

School of Electrical Engineering, Computing and  
Mathematical Sciences

Curtin Institute of Radio Astronomy

Advantages and Limitations of using  
the Murchison Widefield Array for  
Space Surveillance: a Feasibility Study

Steve Raj Prabu

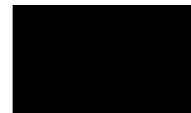
ORCID 0000-0003-3165-6785

This thesis is presented for the Degree of  
Doctor of Philosophy  
of  
Curtin University of Technology

August 2021



To the best of my knowledge and belief this thesis contains no material previously published by any other person except where due acknowledgement has been made. This thesis contains no material which has been accepted for the award of any other degree or diploma in any university.



Steve Raj Prabu

30 August 2021



Sherlock Holmes and Dr. Watson go on a camping trip. In the middle of the night, Holmes wakes up and nudges his faithful friend.

“Watson, look up at the sky and tell me what you see.”

“I see millions and millions of stars, Holmes,” replies Watson.

“And what do you deduce from that?”

Watson ponders for a minute.

“Well, astronomically, it tells me that there are millions of galaxies and potentially billions of planets. Astrologically, I observe that Saturn is in Leo.

Horologically, I deduce that the time is approximately a quarter past three.

Meteorologically, I suspect that we will have a beautiful day tomorrow.

Theologically, I can see that God is all powerful, and that we are a small and insignificant part of the universe. What does it tell you, Holmes?”

Holmes is silent for a moment.

“Watson, you idiot!” he says. “Someone has stolen our tent!”

— Internet



# Statement of Contributions

The content of Chapter 3, Dynamic Spectrum Analysis and Classification of Satellite Signals, is a reproduction of “The development of non-coherent passive radar techniques for space situational awareness with the Murchison Widefield Array”, Publications of the Astronomical Society of Australia , Volume 37 , 2020 , e010. It is my own work, except the following. The development of techniques and discussion of results were contributed by my supervisory panel - Paul J. Hancock, Steven J. Tingay, and Xiang Zhang.

The content of Chapter 4, A Low Earth Orbit Blind Survey using the MWA, is a reproduction of “A low-frequency blind survey of the low Earth orbit environment using non-coherent passive radar with the Murchison Widefield Array”, Publications of the Astronomical Society of Australia , Volume 37 , 2020 , e052. It is my own work, except the following. The development of techniques and discussion of results were contributed by my supervisory panel - Paul J. Hancock, Steven J. Tingay, and Xiang Zhang.

The content of Chapter 5, Preliminary Orbit Determination, is a reproduction of a manuscript titled, “Orbit Determination and Catalogue Maintenance for LEO Objects using the Murchison Widefield Array”, and is under review (on the day of thesis submission). It is my own work, except the following. The development of techniques and discussion of results were contributed by my supervisory panel - Paul J. Hancock, Steven J. Tingay, and Xiang Zhang.

The content of Chapter 6, Targeted Searches for Weak Reflected FM Signals

using the MWA, is a reproduction of a manuscript that is under preparation (on the day of thesis submission), titled, “Improved Sensitivity for Space Domain Awareness Observations with the Murchison Widefield Array”. It is my own work, except the following. The development of techniques and discussion of results were contributed by the MWA collaboration members, Torrance Hodgson, Brian Crosse, Melanie Johnston-Hollitt, and my supervisory panel - Paul J. Hancock, Steven J. Tingay, and Xiang Zhang.



(Signature of Candidate)



(Signature of Supervisor)

(Signature of Chair)



# Acknowledgements

This amazing journey could not have been as productive, memorable, and fun if it weren't for the many wonderful people around me. First of all, I would like to thank my supervisors, Paul Hancock, Steven Tingay, and Xiang Zhang for guiding me through this project. I could not imagine a better group of supervisors. Thank you for your constant support and input into this project which has enabled me to give structure to this thesis. Thank you for molding me into a better researcher.

I would also like to thank Adrian Sutinju, Budi Juswardy, and Angela Dunleavy for the many memorable conversations we have had. Thank you Angela not just for the countless admin help, but also for often checking up with me and making sure I was doing fine. Arash Bahramian, although you were not directly involved in my supervisory panel, you always sent me links to preprints and blogs that you thought would interest me. Also thank you for the feedback you always provided on plots that I shared during group meetings.

The Ph.D. student cohort at CIRA has been a very welcoming and supportive group, and I am grateful for the friendship I have shared with you guys. Especially I would like to thank my friends with whom I had the opportunity to share my entire three-year Ph.D. journey; Jai, Mike, Alex, Torrance, Jun, and Stefan. You guys had a huge part to play in making Perth my home and thank you guys for the many awesome memories I share with you all. Thanks to Jai for helping me settle down all the way from my very first week in Perth. Special thanks to Mike and Alex for making sure I always had sufficient caffeine in my bloodstream throughout the day. I owe you guys (also to Patricia and Emma) an apology

for ghosting on many planned events. To Torrance and Stefan, thank you for the 500+ hours of gaming we accumulated during Covid lockdowns, and without you guys work from home would have been very dull (and probably a lot more productive).

I would also like to extend my sincere thanks to my other friends whose Ph.D. journey briefly overlapped with mine; Jishnu, Susmita, Kariuki, Jaiden, Bella, Pikky, Ronniy, Gayatri, Dilpreet, Ferry, Daniel, and Ben. Special thanks to Pikky, Ronniy, and Bella for making me feel welcome during my first few weeks at CIRA and making me come out of my comfort bubble. To Jishnu, thank you for the many insightful conversations about radio telescopes. To Susmita and Jun, thank you for the constant entertainment you guys provided from my adjacent office cubicle, and for making sure I did not miss my troublesome siblings back home. Thanks to Kariuki for trying very hard to teach me swimming. Maybe next time we should try it in waters not infested with sharks.

Thanks to Manoj, Jai, Sweta, Mahavir, Ramesh, Sidarth, Mohammad, and Nipanjana for often feeding me Indian food every time I felt homesick. Thank you Manoj for also being an excellent flatmate over the last two years of my Ph.D. To my homies from undergrad/school; Hussain, MD, Shrikant, Sujoy, Rahul, and Shashank, thank you for your constant support from across the globe. Especially Hussain, for always being just one phone call away.

Finally, I would like to thank my family for their constant support. Thank you dad for getting me interested in science and engineering from a very young age. You have always been a role model and have inspired me to become a scientist like you. Thank you mom for giving up your own career for taking care of me and my little brother. I can never thank you enough for every sacrifice you have made, and I would always want you to see my accomplishments as your own. To my younger brother Allen, thank you for always making me seem like the lesser naughty child and all the best for your future. I also want to thank my grandparents for their constant love and support throughout my Ph.D. Thank

you for literally checking up on me every single day to make sure I had proper food and did all my grown-up chores. I am always grateful to have you in my life. My only regret is not having my paternal grandad around, and I am sure you would have been really proud to see me finish my Ph.D.



# Abstract

The rapid increase in the volume density of human-made objects in Low Earth Orbit (LEO) has raised concerns about the possible onset of cascading collision event scenarios, i.e, the Kessler Effect. These concerns have motivated the development of Space Domain Awareness (SDA) sensors that are capable of detecting and characterising objects in LEO over a large field-of-view (FoV). With the advent of mega-constellations, such as the 40,000 satellite Starlink constellation being deployed by SpaceX, frequent LEO monitoring is required to help preserve the usability of Earth orbits. In this thesis, I use an existing radio interferometer, the Murchison Widefield Array (MWA), to perform space surveillance by using it as a non-coherent, bi-static, passive radar in the commercial FM band. The study is aimed at developing observation techniques using the MWA to contribute towards the global SDA effort.

I develop the concept of the Dynamic Signal to Noise Ratio Spectrum (DSNRS), a data product that isolates the radar signal of interest from other signals in the environment, including direct path reception from the FM transmitters. I use DSNRS to analyse and classify radar signals in MWA data, and the method resulted in the identification of out-of-band transmissions from CubeSats. These unintended signals contaminate the radio sky and may in future pose a challenge to sensitive radio telescopes on Earth.

I develop and test a blind detection pipeline and run it on archival MWA data, aimed at autonomously detecting narrow-band transient satellite reflection signals. The blind survey detected over 70 unique LEO objects over multiple

passes, along with FM reflections from Geminid meteors, and aircraft flying over the MWA. I also perform line-of-sight range measurements to some of these nearby events (meteors and aircraft), by splitting the MWA into sub-arrays and performing parallax measurements.

In addition to the blind detection capability, I demonstrate preliminary orbit determination and catalog maintenance capabilities using the non-coherent passive radar techniques with the MWA. The orbital elements obtained through this work were found to be in good agreement with publicly available values published by the global Space Surveillance Network (SSN). I also demonstrate more sensitive cued searches using the MWA, that use prior knowledge of a satellite's location to perform signal stacking while following the satellite's trajectory across the sky.

The potential of reflected radio signals and unintended transmissions, both originating from objects in Earth orbit, to interfere with radio astronomy observations has raised concerns about their impact on astronomy. Hence throughout this thesis, based on an understanding of the MWA system, I discuss methods to mitigate the impact of these LEO objects on radio observations performed from the Murchison Radio-astronomy Observatory, home to the MWA, ASKAP, EDGES, the future low-frequency Square Kilometre Array, and numerous other test arrays.

The work done in this thesis has shown the MWA to be a novel instrument that is capable of performing space surveillance. This thesis has also highlighted how performing space surveillance with the MWA is in the best interests of both SDA and the radio astronomy communities.

# Contents

	<b>vii</b>
<b>Acknowledgements</b>	<b>ix</b>
<b>Abstract</b>	<b>xiii</b>
<b>1 Literature Review</b>	<b>1</b>
1.1 Introduction . . . . .	1
1.2 The Problem: The Importance of SDA . . . . .	2
1.2.1 Current Space Domain Awareness (SDA) Solutions . . . . .	3
1.2.2 The Need for other SDA Facilities . . . . .	5
1.3 Proposed Work . . . . .	7
1.3.1 The SDA Framework . . . . .	7
1.3.2 The Murchison Widefield Array . . . . .	8
1.3.3 Overview of Passive Radar Techniques . . . . .	10
1.3.4 Previous Passive Radar Studies using Radio Telescopes . . . . .	12
1.4 Structure of Thesis . . . . .	15
<b>2 Methods: Aperture Synthesis and Orbital Mechanics</b>	<b>19</b>
2.1 Introduction . . . . .	19
2.2 Aperture Synthesis . . . . .	20

2.2.1	Unit of Radiation Measurement . . . . .	20
2.2.2	An Antenna Pair Response to a Single Source . . . . .	22
2.2.3	An Interferometer’s Response to the Apparent Sky . . . . .	25
2.2.3.1	UV Coverage and the Point Spread Function . . . . .	26
2.2.4	Widefield Imaging using W-Stacking . . . . .	30
2.2.4.1	De-Convolution (CLEANing) . . . . .	31
2.2.5	Calibration . . . . .	32
2.2.6	The MWA Signal Chain . . . . .	33
2.2.6.1	Phase 2 Upgrade . . . . .	34
2.2.6.2	The MWA as a Radar System . . . . .	34
2.3	Orbital Mechanics . . . . .	35
2.3.1	Two Line Elements . . . . .	37
2.4	Summary . . . . .	38

### **3 Dynamic Spectrum Analysis and Classification of Satellite Signals** **39**

3.1	Abstract . . . . .	39
3.2	Introduction . . . . .	40
3.3	Observations and Data Processing . . . . .	43
3.3.1	Observations . . . . .	43
3.3.2	Data Processing . . . . .	45
3.3.3	Dynamic Signal to Noise Ratio Spectrum (DSNRS) Analysis	48
3.4	Results . . . . .	55
3.4.1	Results of DSNRS Analysis for Targeted Objects . . . . .	55
3.4.2	Detection of Additional Signals . . . . .	57
3.5	Discussion . . . . .	59



3.5.1	Completeness . . . . .	59
3.5.2	Future work . . . . .	63
3.6	Summary . . . . .	64
<b>4</b>	<b>A Low Earth Orbit Blind Survey using the MWA</b>	<b>67</b>
4.1	Abstract . . . . .	67
4.2	Introduction . . . . .	68
4.3	Background . . . . .	70
4.4	Data Processing . . . . .	71
4.4.1	Blind Search . . . . .	74
4.4.2	Detection Maps . . . . .	74
4.4.3	Parallax Analysis . . . . .	75
4.5	Results . . . . .	78
4.5.1	Satellite Candidates . . . . .	78
4.5.2	Meteor Candidates . . . . .	86
4.5.3	Aircraft . . . . .	87
4.5.4	Transmitters and Unknown Objects . . . . .	88
4.5.5	False Positives . . . . .	88
4.6	Discussion . . . . .	89
4.6.1	Detection Completeness . . . . .	89
4.6.2	RFI Environment Analysis . . . . .	91
4.7	Conclusion . . . . .	96
<b>5</b>	<b>Preliminary Orbit Determination</b>	<b>99</b>
5.1	Abstract . . . . .	99
5.2	Introduction . . . . .	100
5.3	Background . . . . .	103

5.4	Methods . . . . .	104
5.4.1	Angular Coordinate Measurements . . . . .	105
5.4.1.1	Signal Reconstruction . . . . .	105
5.4.1.2	Constraining Cross-Track Structure . . . . .	106
5.4.1.3	Constraining In-Track Structure . . . . .	107
5.5	Results . . . . .	113
5.5.1	Determining the Orbital Elements . . . . .	113
5.5.2	Validation of Results . . . . .	116
5.5.3	HST Re-Acquisition . . . . .	117
5.5.3.1	One Pass Re-Acquisition . . . . .	119
5.5.3.2	Two Pass Re-Acquisition . . . . .	121
5.6	Discussion and Future Work . . . . .	121
5.6.1	SDA Catalog Maintenance using the MWA and Future Im- provements . . . . .	121
5.6.1.1	SDA Sensitivity Dependence on Array Configura- tion and Hardware Parameters . . . . .	122
5.6.1.2	The MWA SDA Capability in the Global Context of SDA Sensors . . . . .	124
5.6.2	Importance of FM Reflecting LEO Catalog for Astronomy Observations . . . . .	126
5.7	Conclusion . . . . .	127
<b>6</b>	<b>Targeted Searches for Weak Reflected FM Signals using the MWA</b>	<b>129</b>
6.1	Introduction . . . . .	129
6.2	Data And Methods . . . . .	130

6.2.1	Shift-Stacking . . . . .	130
6.2.2	Near-field re-focusing . . . . .	132
6.3	Results and Discussion . . . . .	135
6.3.1	Shift-Stacking Candidates . . . . .	135
6.3.2	Near-field Results . . . . .	144
6.4	Conclusion . . . . .	147
<b>7</b>	<b>Conclusion</b>	<b>151</b>
7.1	Project 1: The Dynamic Spectrum Analysis . . . . .	152
7.2	Project 2: A LEO Blind Survey . . . . .	152
7.3	Project 3 : Catalogue Maintenance . . . . .	153
7.4	Project 4 : Targeted Search for Faint Signals . . . . .	154
7.5	Closing Remarks and Future Work . . . . .	155
	<b>Appendices</b>	<b>157</b>
<b>A</b>	<b>Supporting Material</b>	<b>159</b>
A.1	TLEs used in Chapter 3 . . . . .	159
A.2	Supplementary Information for Orbit Determination Solution Con- vergence . . . . .	161
A.3	Visibility fringe-washing as a function of satellite altitude . . . . .	163
<b>B</b>	<b>Copyright Information</b>	<b>165</b>
	<b>Bibliography</b>	<b>171</b>



# List of Figures

1.1	The growth in number of objects in Earth orbit. . . . .	3
1.2	Motivation for performing SDA. . . . .	5
1.3	SDA Analytic Framework. . . . .	6
1.4	MWA tile and Phase 1 configuration. . . . .	8
1.5	MWA Phase 2 configuration. . . . .	9
1.6	Mono-static and bi-static radar. . . . .	10
1.7	Schematic diagram for a bi-static radar. . . . .	11
1.8	The predicted flux density of modelled spherical objects. . . . .	13
1.9	FM reflection from a meteor trail. . . . .	14
2.1	Radiation power detected by a radio telescope. . . . .	21
2.2	A two antenna interferometer. . . . .	23
2.3	Coordinate system used for defining sky brightness distribution. . . . .	26
2.4	MWA Phase 1 and Phase 2 physical configuration and uv coverage. . . . .	29
2.5	Orbital elements measured in an ECI frame. . . . .	36
3.1	Primary beam corrected difference image of ALOS. . . . .	46
3.2	Primary beam corrected difference image of UKube-1. . . . .	47
3.3	Fine channel difference image with direct FM reception. . . . .	49
3.4	RMS noise variation with frequency. . . . .	50
3.5	DSNRS utility on satellite signal and direct path reception event. . . . .	51
3.6	DSNRS plots for all the targeted objects. . . . .	54

3.7	Fine channel image of ISS. . . . .	57
3.8	Fine channel image of Alouette-2. . . . .	58
3.9	Uncatalogued FM reflecting object. . . . .	59
3.10	A single time-step DSNRS for an uncatalogued object. . . . .	60
3.11	Range vs RCS of all the targeted objects. . . . .	62
4.1	Blind detection of KANOPUS-V in a fine channel difference image. . . . .	75
4.2	Detection map of all $6\sigma$ events in an observation. . . . .	76
4.3	Apparent parallax in aircraft detection when splitting the MWA into sub-arrays. . . . .	78
4.4	DSNRS plot for ZIYUAN 3. . . . .	86
4.5	Blind detection of meteor trails. . . . .	87
4.6	Range vs RCS analysis of all detected events. . . . .	89
4.7	Investigating RFI events flagged by AOFLAGGER. . . . .	92
5.1	Isolation of transient events using difference imaging. . . . .	104
5.2	Reconstructed satellite streak. . . . .	105
5.3	Historic TLE evolution. . . . .	108
5.4	1 pass and 2 pass HST re-acquisition. . . . .	113
5.5	Historic evolution of HST TLE. . . . .	120
6.1	Demonstration of shift-stacking. . . . .	133
6.2	The near-field curvature as seen by a baseline pair. . . . .	134
6.3	An example of a flaring event detected using shift-stacking. . . . .	135
6.4	Apparent centroid distribution for flaring and steady reflection events. . . . .	137
6.5	Frequency distribution for flaring and steady reflection events. . . . .	138
6.6	Detected new candidates in Range vs RCS parameter space. . . . .	139
6.7	Demonstration of the near-field imaging capability using the MWA. . . . .	145
6.8	Baselines affected by fringe-washing and near-field effects. . . . .	147

6.9	Number of baselines not fringe-washed as a function of integration time. . . . .	148
A.1	TLEs used for DSNRS . . . . .	160
A.2	Orbit determination solution convergence analysis . . . . .	162





# Chapter 1

## Literature Review

### 1.1 Introduction

On October 4<sup>th</sup>, 1957, the first human-made satellite was launched into orbit, marking the beginning of the space race (Lyon, 1960). Despite the vast expense of launching satellites, more than 25 were launched in the next year, due to geopolitical competition. Today, the capability exists to deploy over 100 satellites in a single launch<sup>1,2</sup> into Low Earth Orbit (LEO).

With more launches comes more debris resulting from those launches (expended rocket bodies and upper stages, defunct satellites, the results of explosions and collisions, and general bits and pieces that have detached from other objects). Much effort is expended on tracking more than 500,000<sup>3</sup> pieces of these human-made debris orbiting the Earth.

*“As the number of artificial satellites in Earth orbit increases, the probability of collision between satellites also increase”*, to quote Donald J. Kessler, in his paper (Kessler & Cour-Palais, 1978) that describes the possibility of cascading collision events in LEO that can result in a debris cloud around the Earth. This is the so-called Kessler Effect.

---

<sup>1</sup><https://www.space.com/35709-india-rocket-launches-record-104-satellites.html>

<sup>2</sup><https://www.space.com/spacex-launches-143-satellites-transporter-1-rocket-landing>

<sup>3</sup>[https://www.nasa.gov/mission\\_pages/station/news/orbital\\_debris.html](https://www.nasa.gov/mission_pages/station/news/orbital_debris.html)

This PhD thesis explores the use of non-coherent passive radar techniques with the Murchison Widefield Array (MWA) (Tingay et al., 2013a), primarily focused on contributing towards Space Surveillance whilst also briefly investigating other opportunities of exploration the non-coherent passive radar data may provide (such as aircraft/meteor detection and RFI environment analysis). The work develops and demonstrates techniques to perform cued and un-cued detections<sup>4</sup> of LEO objects, thus showing the MWA SDA system to be a valuable addition to existing space surveillance facilities (Prabu et al., 2020b,a).

The SDA problem and the proposed work are described in Section 1.2 and Section 1.3, respectively. The structure of this thesis is described in Section 1.4.

## 1.2 The Problem: The Importance of SDA

When the density of objects in a given orbit increases past a critical value, it can lead to a cascading collision called the Kessler Effect (Kessler & Cour-Palais, 1978; Kessler et al., 2010). The Kessler Effect could render entire orbits useless for future space missions and applications and put the lives of astronauts in orbit at risk. Figure 1.1 shows the growth rate of the number of human-made objects in Earth orbit over time from the 1950s. The onset of the Kessler Effect can be delayed, or its impacts mitigated, by performing SDA and frequently monitoring the orbits of these objects, using that information to actively manage the space environment and/or active satellites (where possible). Although the Kessler Effect is an extreme scenario, there exist less extreme cases where a small number of objects are involved. Given the current and projected future dependency of the world economy, communications, agriculture, and security on space assets, SDA is a critical activity to maximise the continued success of these

---

<sup>4</sup>In this thesis, detections are classified as uncued when the observations are reduced without any prior information about the objects within the FOV. A detection is classified as cued when the data processing is done to search for a given object (techniques demonstrated in Chapter 6) where we use prior information about the object's pass/orbit to obtain a statistically significant detection.

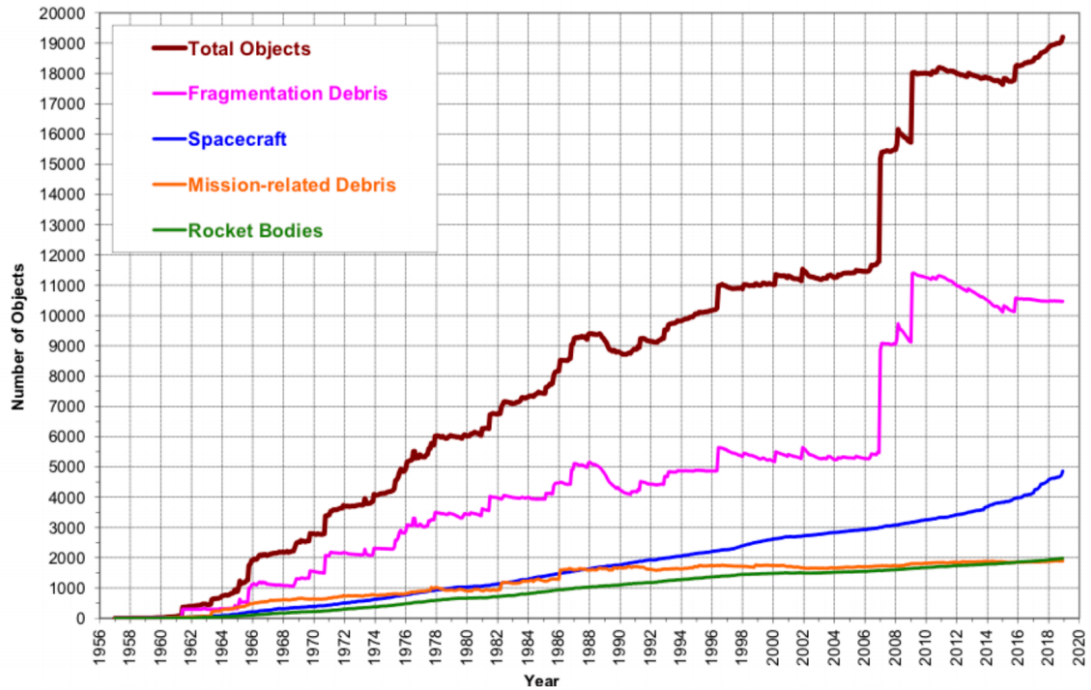


Figure 1.1: The growth in the number of objects in Earth orbit as a function of time (plot obtained from Gallozzi et al. (2020))

endeavors.

The importance of SDA was illustrated when two satellites, Iridium-33 and Kosmos-2251, collided in orbit in 2009 (Kelso, 2009), which drastically increased the total number of orbiting objects (can be seen in Figure 1.1). The density of objects has further increased due to anti-satellite capabilities tested by China (Kelso, 2007), India (Akhmetov et al., 2019), Russia (Johnson-Freese & Burbach, 2019), and the United States (Pardini & Anselmo, 2009). SDA also helps predict the trajectory of objects as they re-enter the atmosphere, e.g. when SkyLab crashed in Western Australia <sup>5</sup>.

### 1.2.1 Current Space Domain Awareness (SDA) Solutions

Over the last few decades, the United States Department of Defence (DoD) have taken the lead role of tracking these orbiting human-made objects and glob-

<sup>5</sup><https://www.abc.net.au/local/photos/2009/07/09/2621733.htm>

ally sharing the information. The SDA program run by the US is called the Space Surveillance Network (SSN) (Miller, 2007), and it has been obtaining data about LEO debris from as early as 1990 (Stansbery et al., 1995). These sensors are divided into dedicated, collateral, and auxiliary sensors. The dedicated and collateral sensors are run by the USSPACECOM and auxiliary sensors are operated by other groups. The primary objective of the dedicated sensors is to detect human-made artifacts orbiting Earth, while the collateral and auxiliary sensors perform SDA as their secondary objective.

Most of the existing SSN infrastructure consists of optical sensors or active radars (the detection system of an active radar is discussed in Section 1.3.3) Henize et al. (1993); Woods et al. (2013); Reed (1969). All the radar facilities used by the SSN perform SDA as their secondary objective (Muntoni et al., 2021) as most of them are primarily used as missile warning systems. The orbital parameters obtained by SSN are publicly available<sup>6</sup> in the Two Line Element (TLE) format<sup>7</sup> (discussed further in Chapter 2), that are generally valid for a few weeks before/after the epoch at which the measurements were made.

The European equivalent of SSN was started by the European Space Agency (ESA) in 2009 (Bobrinsky & Del Monte, 2010). This initiative was established to analyze the space environment and space weather in three different programs: Space Surveillance and Tracking (SST); Near Earth Object (NEO) monitoring; and Space Weather (SWE) (Flohrer & Krag, 2017). The program is currently funded at 95 million Euros per year with 19 participating states.

Some examples of other SDA radars across the globe are Kamisaibar Space Guard Centre Radar at Japan (Taromaru et al., 2005), RT-70 in Ukraine (Konovalenko et al., 2005; Molotov et al., 2004), and Silentium passive radar system<sup>8</sup> in Australia.

---

<sup>6</sup><https://www.space-track.org/auth/login>

<sup>7</sup><https://www.celestrak.com/NORAD/documentation/tle-fmt.php>

<sup>8</sup><https://www.silentiumdefence.com.au/>

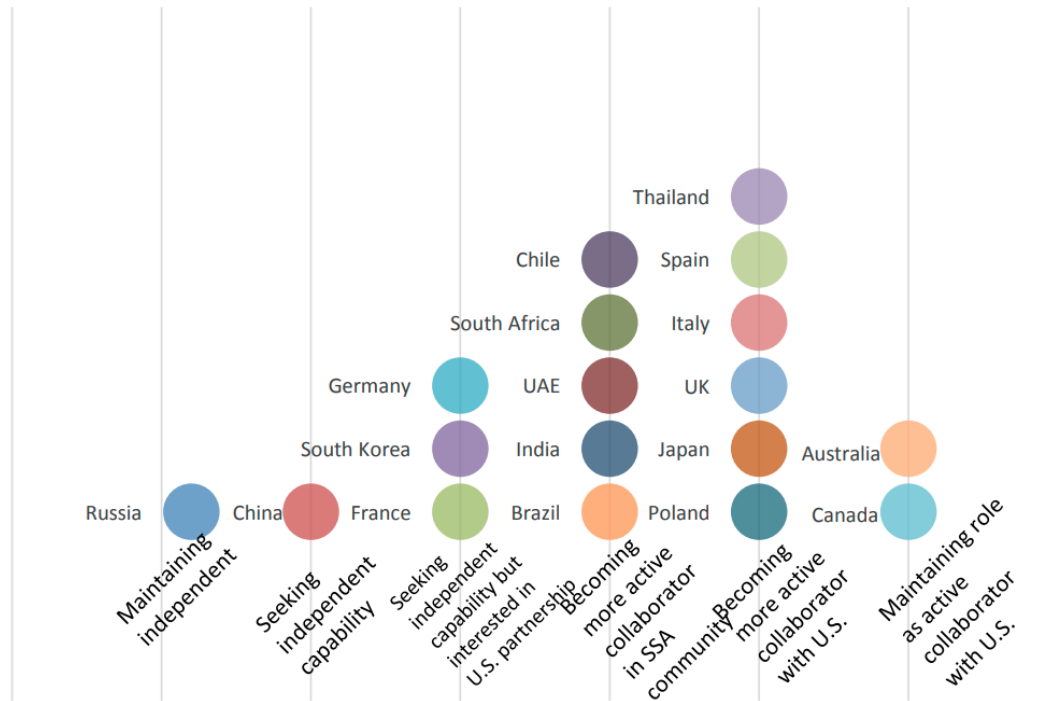


Figure 1.2: Figure categorises different countries with interest in performing SDA based on their motivation to do so. (Image obtained from Lal et al. (2018))

### 1.2.2 The Need for other SDA Facilities

In the recent past, there has been a growing concern about the predicted observation load increase on the existing SDA facilities with the advent of mega-constellations. For example, the Starlink Constellation alone is predicted to receive about 7.2 million conjunction warnings per year (Lal et al., 2018), and with each of these warnings we require followup observations to closely monitor the objects of interest. Also, with the increasing usage of on-board electric propulsion system (that gradually changes the satellite’s orbit), we require increased number of observations of the objects in order to always retain an accurate understanding of the LEO environment.

There is also an increasing desire for countries to be self-reliant on SDA information, to prevent bias of information. For example, “South Korean government officials estimate that their country receives [SDA] data on only about 40 percent

of the objects tracked by DoD, due to sensitivity of US assets” (Lal et al., 2018). Decentralisation of SDA capability across different countries would also prevent the current leading SDA nations from monetising the SDA data. A recent study of the motivation behind different countries to participate in SDA is summarised in Figure 1.2.

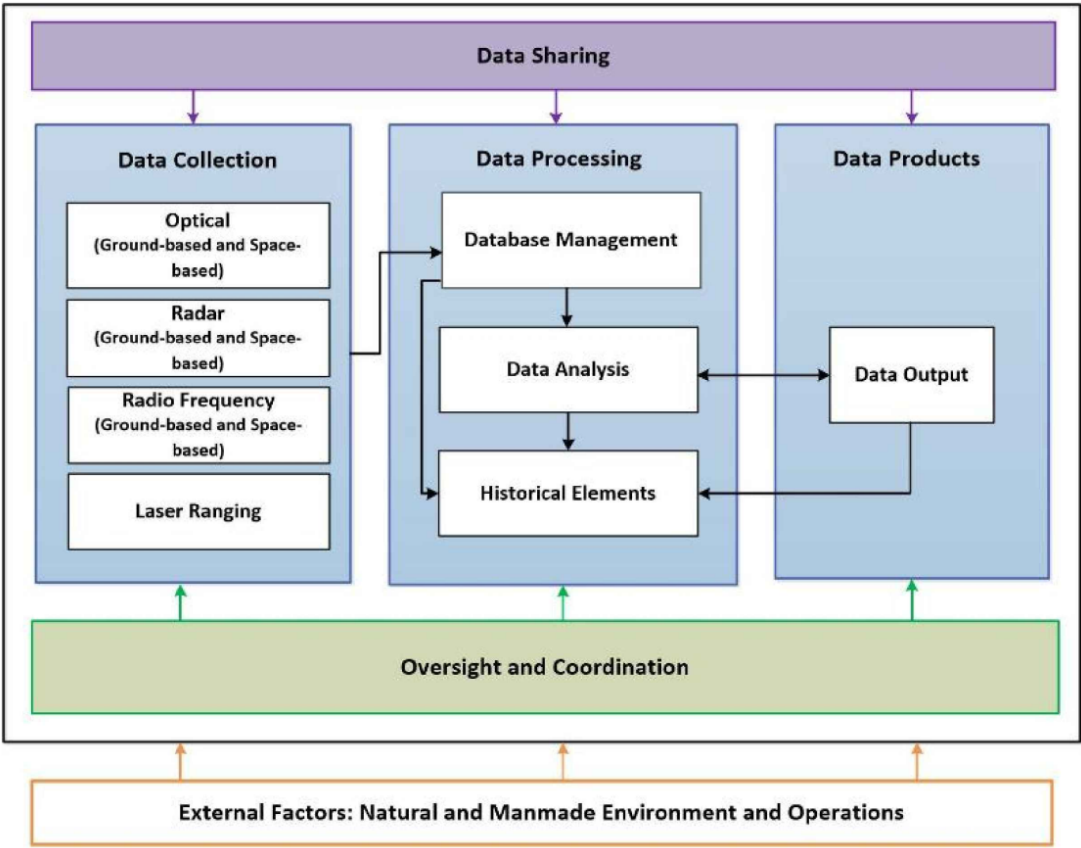


Figure 1.3: Figure shows the analytic framework used in Lal et al. (2018) to study the different SDA facilities around the world.(Image obtained from Lal et al. (2018))

## 1.3 Proposed Work

### 1.3.1 The SDA Framework

Due to the lack of a globally accepted definition of SDA, a recent case study (Lal et al., 2018) that investigated space surveillance capabilities of 18 different countries, used a modularised analytical framework (shown in Figure 1.3) that described the different SDA activities undertaken by these individual groups. The framework has been “functionally modularised” in order to reduce the cost associated with the individual activities and to enable private sectors to step in.

The *Data Collection* module incorporates performing observations (astrometry) of Resident Space Objects (RSOs) and the data is processed in *Data Processing* module to perform orbit determination, catalog maintenance, and conjunction monitoring. The *Data Products* module contacts satellites operators to coordinate maneuvers to avoid in orbit collisions. The *Oversight and Coordination* and *Data Sharing* modules comes up with guidelines and regulations to ensure proper communication between the previously discussed modules. The outside influence of government policies and other natural influences on the SDA activities are encapsulated by the *External Factors* module.

This thesis aims to demonstrate that an already existing radio interferometer, the Murchison Widefield Array (MWA), can be used as a passive radar to contribute towards the *Data Collection* module of the SDA framework. To validate the collected data, this thesis also develops a basic orbit determination method that enables us to update TLEs for RSOs and re-acquire them on future orbits. The benefits of performing SDA with an existing radio interferometer is two-fold; firstly, its location outside the current leading SDA nations helps towards decentralising the SDA data (as previously discussed in Section 1.2.2), secondly, performing SDA as an secondary activity helps reduce the involved cost (both from construction and operation point of view). In the age of mega-constellations that use electric propulsion to slowly change orbits, the large FOV of the MWA

should enable it to monitor multiple objects simultaneously and perform catalog updates, thus proving to be a novel SDA instrument.

### 1.3.2 The Murchison Widefield Array

The high density of objects in LEO leads one to consider the utility of a detection system that has a large Field of View (FoV), in order to perform simultaneous detections and with the ability to rapidly change pointing direction. One such instrument is the MWA (Tingay et al., 2013a), an interferometer primarily built for astronomical studies (Bowman et al., 2013; Beardsley et al., 2019). The MWA is a low frequency precursor to the Square Kilometre Array (SKA), located in the radio-quiet Murchison Radio-astronomy Observatory (MRO) in Western Australia (also the site where the low frequency component of the SKA will be built).

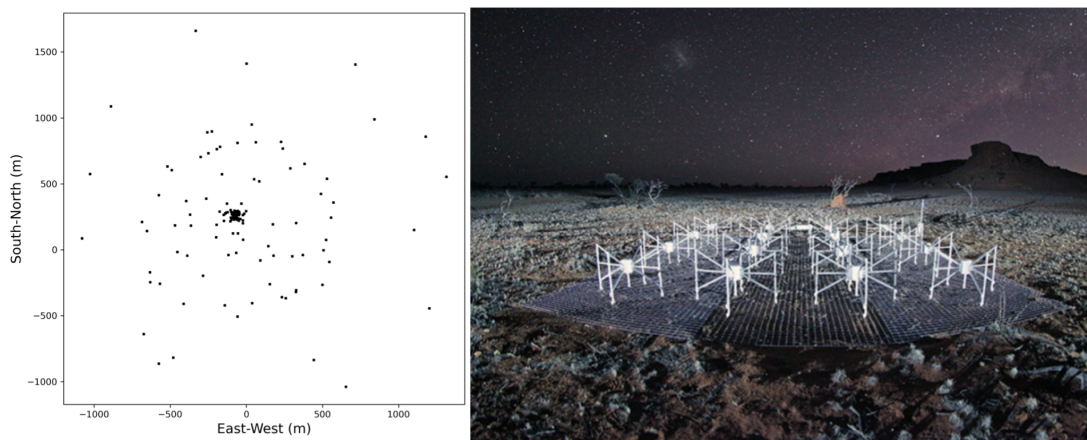


Figure 1.4: The left panel shows the tile configuration of the Phase 1 MWA and the right panel shows an image of an MWA tile (Right panel image credit to Dr John Goldsmith/Celestial Visions, and was obtained from <http://www.mwatelescope.org/>)

The MWA has 128 tiles, each comprising of 16 dual-polarised bow-tie antennas (Tingay et al., 2013a) (as shown in Figure 1.4) and can observe the Southern hemisphere sky in the 70 – 300 MHz frequency range with a 30.72 MHz processed bandwidth (for each polarisation). The MWA has gone through a recent upgrade



to Phase 2 (Wayth et al., 2018), with two different configurations in which it can operate. The spatial scales probed by a radio-interferometer is determined by the ground arrangement of the array, and conversely, the resolution of the instrument is dependant on the diffraction limit of its longest baselines. Hence, the different ground configurations of the MWA were determined by their respective science goals. The Phase 1 MWA had a maximum baseline length of 3 km, while the extended configuration of Phase 2 has a longest baseline of 5.3 km (physical configuration for the compact and extended MWA Phase 2 array is shown in Figure 1.5). The Phase 2 extended configuration was primarily intended to perform galactic and extra-galactic surveys of the southern radio sky. The Phase 2 compact configuration has most of the tiles within a 200 m diameter area (more information on the MWA signal path can be found in Chapter 2) in order to study the diffuse emission as part of EoR science. This thesis explores the use of the MWA as a sensitive receiving system as part of a passive bi-static radar configuration.

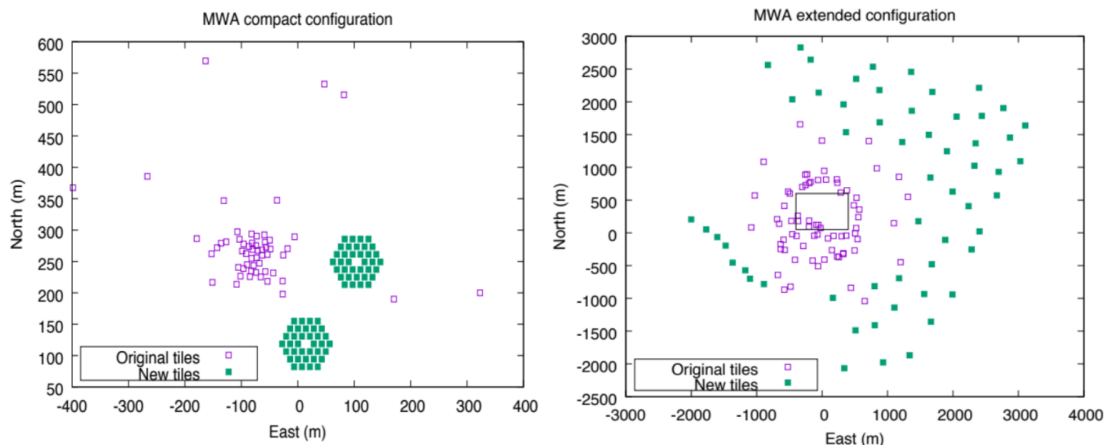


Figure 1.5: The left panel shows the tile locations for the Phase 2 compact configuration and the extended configuration of Phase 2 is shown in the right panel (Image obtained from Wayth et al. (2018)).

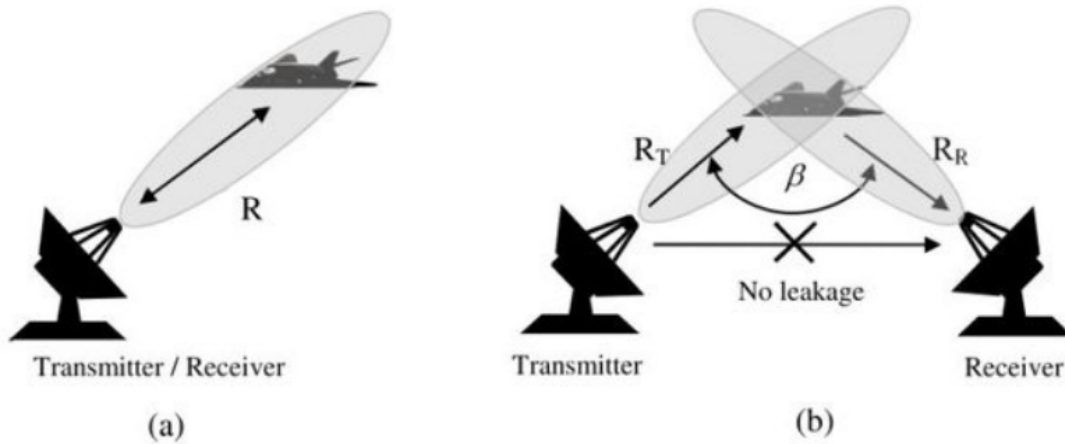


Figure 1.6: The two configurations of radars, namely mono-static (left panel) and bi-static radars (right panel) (Image obtained from [Aziz et al. \(2015\)](#)).

### 1.3.3 Overview of Passive Radar Techniques

Radars operate by detecting reflected/scattered radio signals from the target of interest ([Skolnik, 1990](#)). Although radars were preliminary developed for military purposes during World War II, they have a large of number of civilian applications, such as maritime and airborne navigation, weather monitoring, and space surveillance.

Based on the number of individual elements (transmitter/receiver) used, radars are classified as mono-static and bi-static (as shown in [Figure 1.6](#)). A mono-static radar transmits the signal and receives the echo return from the same location, while in a bi-static radar the transmitter and receiver are two different elements at two different locations. Bi-static radars can be further classified as active or passive radars. The receiver in active radars detects the echos of signals transmitted by a dedicated and coordinated transmitter, while a passive radar detects the echos of signals transmitted by non-cooperative radio transmitters (such as commercial FM,  $\sim 100$  MHz, radio transmitters, which is the focus of this thesis).

The received power in a bi-static radar is approximated as follows (schematic shown in [Figure 1.7](#)). Let the transmitter of the bi-static radar transmit with an

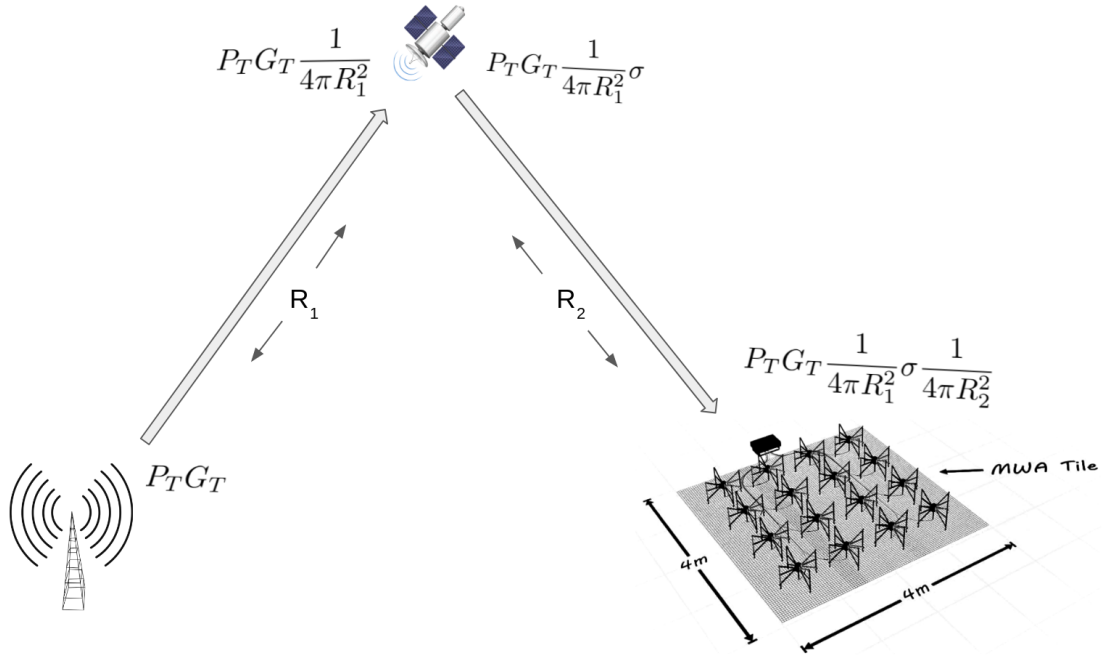


Figure 1.7: Schematic diagram for a bi-static radar, including the basic bi-static radar equations.

isotropic power  $P_T$  with a gain of  $G_T$  in the direction of the target. Assuming the signal travels as a spherical wave-front, the power density incident on the target at a distance  $R_1$  would be  $P_T G_T \frac{1}{4\pi R_1^2}$ . If the target has a reflecting area  $\sigma$  (also called as the Radar Cross-Section), the reflected power from the target would be  $P_T G_T \frac{1}{4\pi R_1^2} \sigma$  (assuming no absorption). If the receiver is at a distance  $R_2$  from the target and assuming the reflected signal also travels as a spherical wave front, then the power received by the bi-static receiver is given by

$$POWER_{RX} = P_T G_T \frac{1}{4\pi R_1^2} \sigma \frac{1}{4\pi R_2^2} A_{receiver} \quad (1.1)$$

where  $A_{receiver}$  is the collecting area of the receiver. The received power by a mono-static radar is a special case where  $R_1 = R_2$ .

### 1.3.4 Previous Passive Radar Studies using Radio Telescopes

Radio telescopes such as the Long Wavelength Array (LWA) (Taylor et al., 2012; Helmboldt et al., 2014), Arcebo (Castleberg & Xilouris, 1997), Effelsberg (Ruiz et al., 2005), and LOw Frequency ARray (LOFAR) (van Haarlem et al., 2013; Gaussiran II et al., 2004) have detected objects such as meteors and aircraft through reflections of terrestrial transmitters in the past. In this project, the focus is on the MWA, due to its large FoV and excellent imaging capabilities, and due to the MWA being located at a very radio quiet site.

The MWA has been previously used to detect satellites using two different passive radar techniques, namely coherent passive radar (Palmer et al., 2017; Hennessy et al., 2019) and non-coherent passive radar (Tingay et al., 2013b; Zhang et al., 2018). The coherent method uses the high time and frequency resolution Voltage Capture System (VCS) (Tremblay et al., 2015) data from the MWA, while the non-coherent method uses the time and frequency averaged correlated data, as would be normally used for making standard images from an interferometer. The coherent method performs detection by using matched filters (Hennessy et al., 2019) (designed using the transmitted FM signal as reference) to search for signals reflected from satellites, while the non-coherent method uses wide-field imaging and source finding techniques. This thesis uses the non-coherent detection method (detailed in Chapter 2).

The first demonstration of the non-coherent method using the MWA was performed by Tingay et al. (2013b) during the commissioning phase of the MWA (using 32/128 tiles) with a maximum north-south baseline (antenna separation) of 2 km and an east-west baseline of 1 km. The angular resolution was  $5' \times 10'$  at a central frequency of 103.4 MHz, with a bandwidth of 30.7 MHz. The demonstration detected the International Space Station (ISS) in reflected transmissions from different FM radio stations located at Perth and Geraldton, depending on its location in the sky.

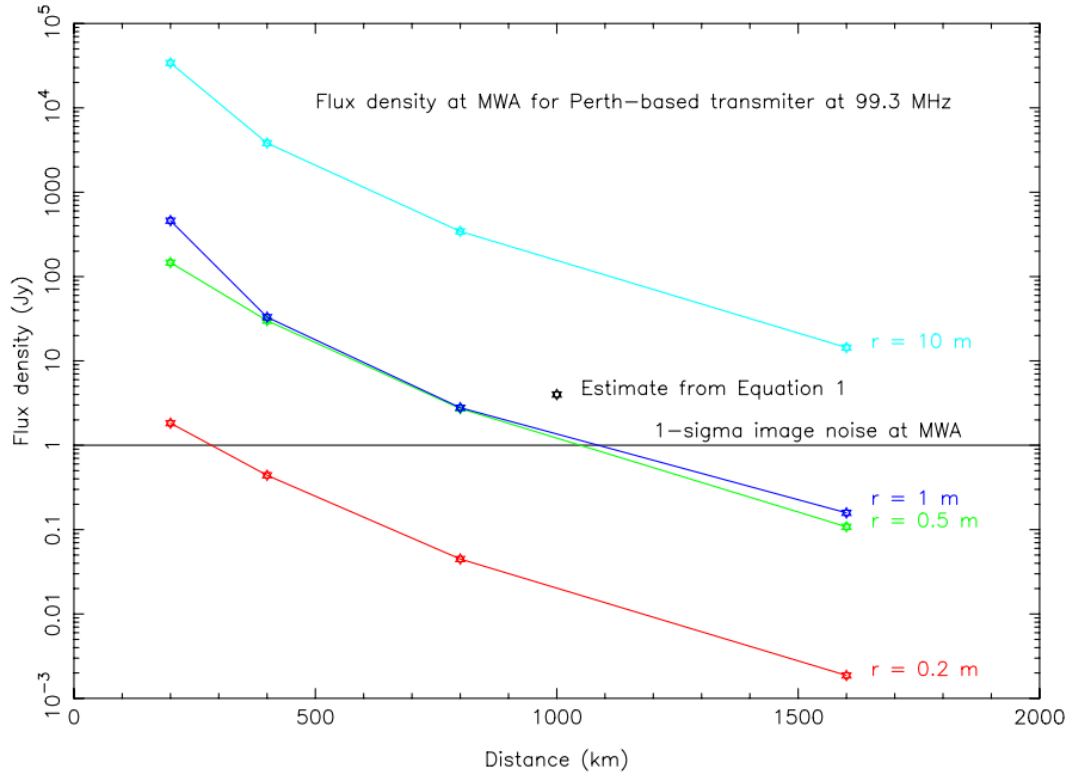


Figure 1.8: The predicted flux density of modelled spherical objects as a function of distance (plot obtained from Tingay et al. (2013b))

Tingay et al. (2013b) also published an XFDTD<sup>9</sup> (a time domain finite difference electromagnetic simulation software) simulation, estimating that debris with an equivalent radius greater than 0.5 m could be detected up to a range of 800 km with 1 s integration times and a 50 kHz bandwidth, and smaller debris could be detected with longer integration times. The simulation was performed for 11 different FM radio stations, for debris with radii 0.2 m, 0.5 m, 1 m, and 10 m, and at altitudes of 200 km, 400 km, 800 km, and 1600 km. The results of the simulations are shown in Figure 1.8. (Note that for a specific object pass and a specific FM transmitter, we could optimize the integration time, bandwidth, and primary beam pointing to obtain the maximum possible SNR. However, in this thesis, we use generic parameters that were found to work for all LEO objects and FM transmitters. The choice of bandwidth would also depend on

<sup>9</sup><https://www.remcom.com/xfdtd-3d-em-simulation-software>

the FM transmitter being considered and its overlap with the quantised MWA fine frequency channels. For example, FM channels often have a bandwidth of 200 kHz and can be fully captured at the highest possible SNR by 5 adjacent fine channels of 40kHz bandwidth that perfectly overlaps with the FM transmission. However, the FM channels and the fine frequency channels do not always perfectly overlap, resulting in loss of SNR. Similarly, for an object at 800km altitude would approximately require double the integration time required for an object at 400km in order to produce streaks of similar lengths. Hence, throughout this thesis, we use observation parameters that worked well for all LEO objects).

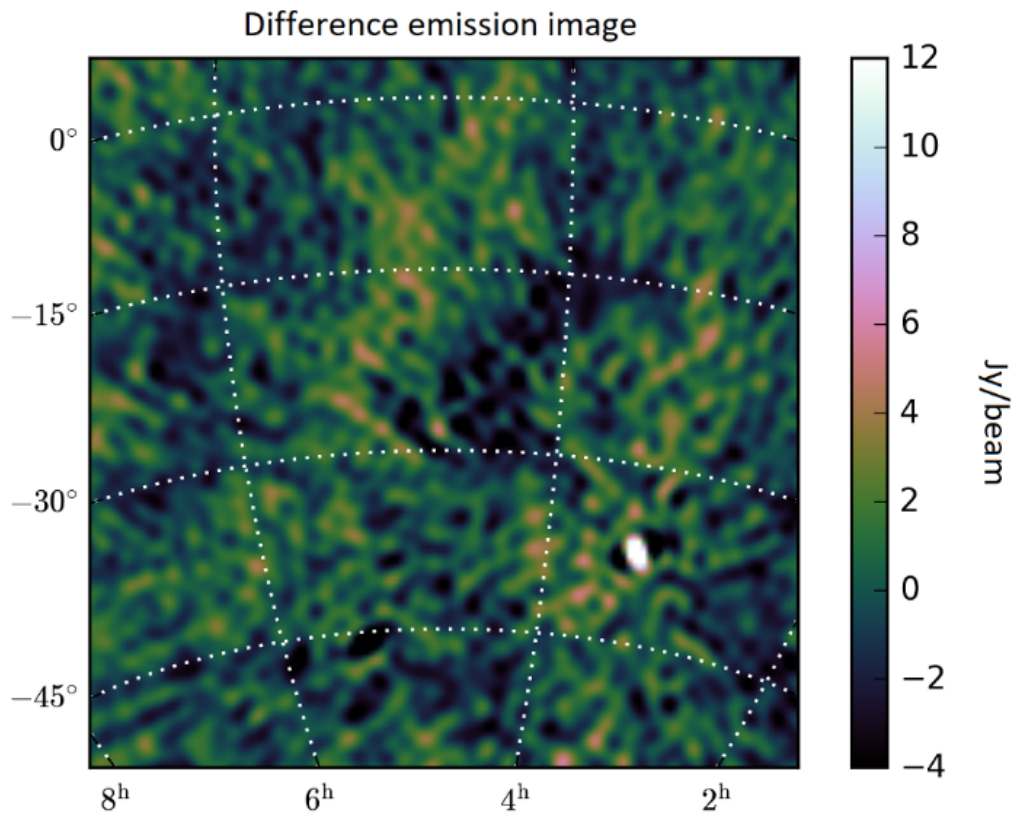


Figure 1.9: FM transmitter reflection off a meteor candidate as observed by [Zhang et al. \(2018\)](#).

The MWA has also been used to search for meteors ([Zhang et al., 2018](#)) in the past, using the same technique. When a meteoroid enters the atmosphere, it is heated to very high temperatures. This causes the meteor to leave behind an

ionised trail due to collisions with particles in the air. The MWA was used to detect these meteors using the FM transmissions reflected by the ionised trails. The idea was validated through a 322 hour observation with MWA and observations with the Desert Fireball Network (DFN) (Bland et al., 2012).

The constant astronomical background signals in the MWA images were removed using difference imaging. During the MWA observations, only baselines shorter than 387 m were used. This was due to the fact that the meteors when observed by the MWAs longest baseline at 80 MHz would still be in the near field. An object is considered to be in the far-field if the received wave-front can be approximated to a plane (when compared to the antenna separation). However, for nearby sources (such as meteors, aircraft, and satellites), the wave-front curvature is significant on the longest MWA baselines, and violate the coherent integration assumption in interferometer theory. Another reason for using short baselines is due to the fact that the meteor trails are extended sources (short baselines are more sensitive to extended sources, as explained in Chapter 2). During these observations, two satellites were also detected, with range greater than 500 km and radar cross sections (RCS) ranging from  $0.1m^2$  to  $1m^2$ . These detections provided the motivation for the PhD thesis project described here, and are investigated further in Chapter 3.

## 1.4 Structure of Thesis

This thesis aims to primarily study how the MWA can be used to contribute towards LEO space surveillance along with other serendipitous opportunities the data may provide (such as RFI environment analysis which is of extreme interest to the radio-astronomy community) by building upon the previously established non-coherent passive radar techniques in Tingay et al. (2013b) and Zhang et al. (2018). In cases where satellites are themselves transmitting in the MWA frequency band, these signals are used rather than reflections from Earth-based transmitters. As the MWA is located at the same site as the future low-frequency

component of the SKA, many of our SDA analysis had great implications for understanding the RFIs seen by the SKA. Hence, wherever possible, we translate our results in the context of the SKA. The proposed study is pursued as smaller goals (each exploring a different aspect of the MWA technology) within this thesis, as mentioned below:

- Provide an introduction to aperture synthesis (data calibration, imaging, and signal detection) and propagation of satellites using Simplified Propagation Models (SPG) and mean orbital elements (TLEs) is described in Chapter 2;
- Investigate further the satellite detections previously carried out by Zhang et al. (2018) and identify the different frequencies reflected by these objects (demonstrating the high time and frequency resolution of the MWA's correlated data). This study has been performed in Chapter 3;
- Develop an understanding of the parameter space probed by the MWA SDA system, by performing a blind survey of LEO environment using MWA observations. The blind survey is performed in Chapter 4 using archived MWA data, thus demonstrating the versatile nature of MWA observations;
- Validate the collected MWA SDA data by performing orbit determination for LEO objects. The method developed is preliminary and allows us to re-acquire LEO objects during subsequent passes. An illustrative sample of 33 observations from the blind survey that have the best quality detections (detected over multiple epochs) have been used in Chapter 5 to demonstrate the orbit determination and TLE catalogue maintenance capabilities of the MWA;
- Explore targeted SDA search capability using the MWA to detect faint satellite signals. Chapter 6 develops and tests two methods to perform targeted satellite signal searches in MWA observations. The chapter also



explores the sensitivity of the different MWA configurations towards near-field satellite events;

The overall conclusions of the work are summarised in Chapter 7. Chapter 3 and 4 have been published as peer reviewed journal papers in the Publications of the Astronomical Society of Australia (PASA). Chapter 5 and 6 are a reproduction of a papers that is currently under review with PASA and Advances in Space Research, respectively.



# Chapter 2

## Methods: Aperture Synthesis and Orbital Mechanics

### 2.1 Introduction

The first reported observation of astronomical radio emission was performed by Karl Jansky in 1932, during his study of noise sources affecting intercontinental radio communications ([Jansky, 1932](#)). Intrigued by Jansky's findings, Grote Reber went on to carry out the first published radio astronomy survey ([Reber, 1944](#)) in 1944. The telescopes used by Jansky and Reber were single antennas, whose resolution was limited by the diffraction limit of the instrument at the observed wavelength. In 1946 Sir Martin Ryle and D.D Vonberg developed the method of performing higher resolution measurements (much above the diffraction limit of a single antenna) of sky intensity distributions by combining the signals from multiple antennas (later termed as aperture synthesis) ([Ryle & Vonberg, 1946](#)), and Sir Martin Ryle was later awarded the Nobel prize for his contributions in 1974. Since then the field of aperture synthesis has developed rapidly over the last few decades, leading to the current Square Kilometre Array (SKA) era ([Dewdney et al., 2009](#)).

In this Chapter, I briefly explain aperture synthesis techniques for observing

the radio sky, and the methods associated with calibrating and imaging aperture synthesis data in Section 2.2. I also explain the MWA signal chain in Section 2.2.6 along with aperture synthesis methods applied to the MWA. I conclude the chapter by giving a brief introduction to orbital mechanics methods in Section 2.3.

## 2.2 Aperture Synthesis

I start by describing the different units of radiation measurement used commonly in aperture synthesis, before proceeding to summarise the relationship between the interferometer’s response and the sky brightness distribution.

### 2.2.1 Unit of Radiation Measurement

The power dissipated by an isotropic radiating source is given by its luminosity  $L$  (J/s). We estimate the luminosity from the power measured by an antenna element. The power measured depends on the collecting area of the antenna and its distance from the source (Figure 2.1), as given by Equation 2.1,

$$P_{measured} = L \times \frac{1}{4\pi d^2} \times A_{eff}, \quad (2.1)$$

where  $L$  is the luminosity,  $d$  is the distance between the source and the antenna,  $P_{measured}$  is the measured power, and  $A_{eff}$  is the effective collecting area of the instrument. The measured power is normalised by its collecting area (using Equation 2.2) to obtain flux  $F$  ( $J s^{-1} m^{-2}$ ). Flux is a measure of the time rate of radiation energy passing through an unit area at a distance  $d$  from a source of luminosity  $L$ ,

$$F = P_{measured}/A_{eff}. \quad (2.2)$$

Flux is not a measurable quantity in practice as no single instrument is capable

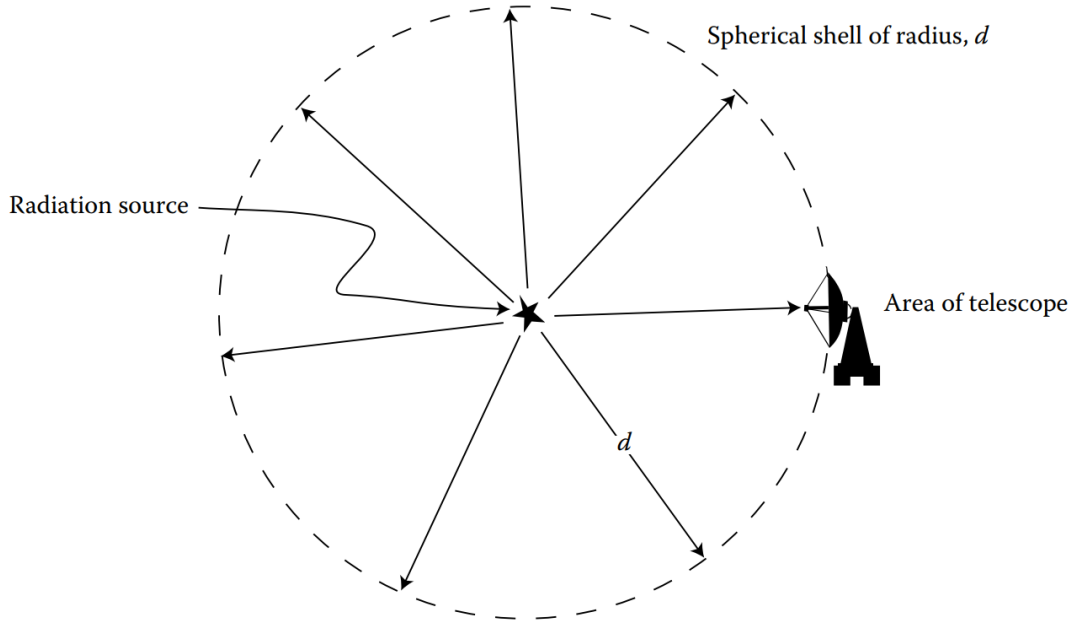


Figure 2.1: Figure shows the fraction of the radiated power detected by the radio telescope (image credit [Marr et al. \(2015\)](#)).

of observing over the entire electromagnetic spectrum. Hence, flux is further normalised by the bandwidth  $\Delta\nu$  of the instrument to obtain flux density,  $F_\nu$  ( $J s^{-1} m^{-2} Hz^{-1}$ ), using Equation 2.3.

$$F_\nu = F/\Delta\nu \quad (2.3)$$

The Jansky (Jy)<sup>1</sup> is the conventional unit of flux density measurement in radio-astronomy. A Jansky is defined in SI units as  $1 \text{ Jy} = 10^{-26} J s^{-1} m^{-2} Hz^{-1}$ .

The final quantity of radiation measurement is intensity (or surface brightness). Intensity ( $I$ ) is defined as flux density per unit solid angle ( $Jy \Omega^{-1}$ ). For resolved sources, intensity helps describe the radiation distribution within the source and is also independent of distance from the source. Hence for resolved sources, “Intensity is a direct measure of the [radiating] object’s surface brightness, that is, the amount of energy radiated per second per unit area of the surface

---

<sup>1</sup>named after Karl Guthe Jansky, the father of radio-astronomy.

per unit solid angle *right at the surface*” (Marr et al., 2015). The measured intensity is proportional to the square of the electric field from the source (see Marr et al. (2015) for more details), and this is a very important relation that will be used later in Section 2.2.3 to derive the instrument’s response to the apparent radiating sky.

## 2.2.2 An Antenna Pair Response to a Single Source

In this section, I briefly explain the response of a radio-interferometer to a radiating source at infinity, first using two antennas (*Antenna*<sub>1</sub> and *Antenna*<sub>2</sub>) followed by a generic formalisation of the aperture synthesis response of  $N$  antenna elements to a distribution of radiating sources (the apparent sky) in the following section.

Let us first consider two identical antenna elements separated by a distance  $b$  (called a baseline) observing a far-field<sup>2</sup> unresolved source at an angle  $\theta$  from the zenith, as shown in Figure 2.2. From Figure 2.2, we see that the wave-front as measured by *Antenna*<sub>1</sub> has travelled an extra distance  $\Delta s$  (for the signal to arrive in phase), compared to *Antenna*<sub>2</sub>. The time delay corresponding to the the extra distance can be found using Equation 2.4,

$$\tau = \frac{b \times \sin(\theta)}{c}, \quad (2.4)$$

where  $\theta$  is the angle of the source from the zenith, and  $c$  is the speed of light. The electric field due to the far-field source at the location of the antennas at any instant can be written as

$$\begin{aligned} E_1(t) &= E_o e^{i2\pi\nu t} \\ E_2(t) &= E_o e^{i2\pi\nu(t+\tau)}, \end{aligned} \quad (2.5)$$

where  $\nu$  is the frequency of the observation,  $E_o$  is the amplitude of the electric

---

<sup>2</sup>the source is far enough that the radiation wave-front from it can be assumed to be planar.

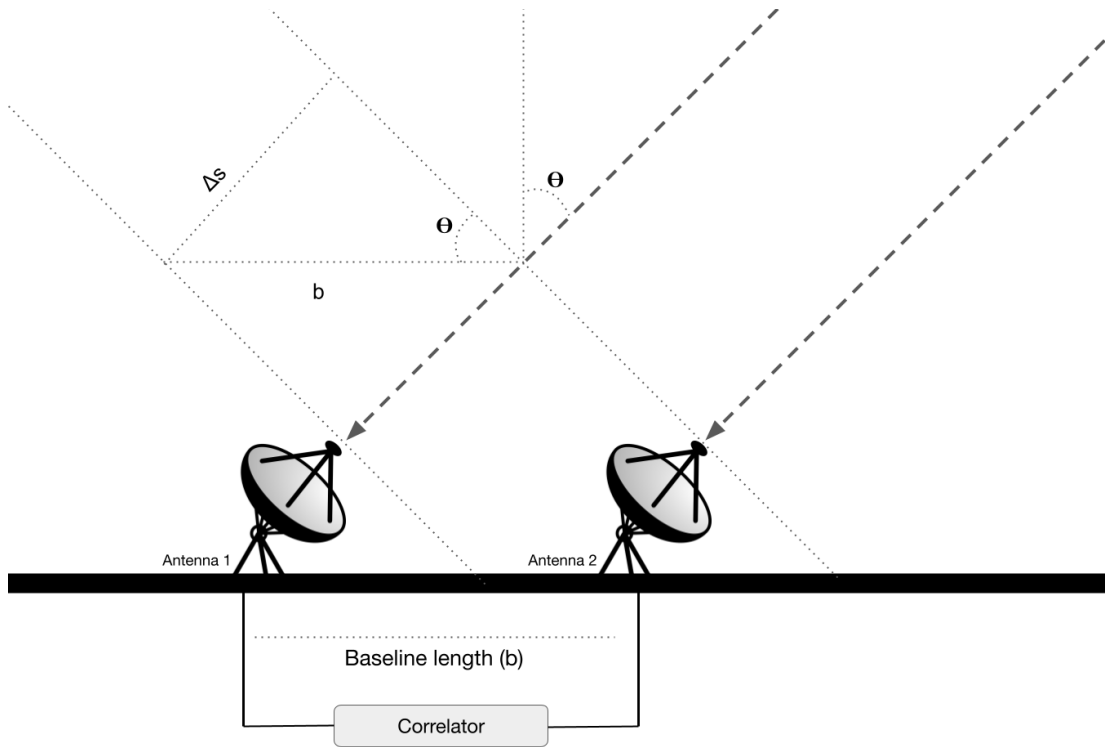


Figure 2.2: A two antenna interferometer observing a source at an angle  $\theta$  from the zenith.

field, and  $t$  is time. The voltage response of the antenna is proportional<sup>3</sup> to the electric field, and hence Equation 2.5 can also be treated as the mathematical form of the voltage signal measured by the antenna (the constant of proportionality can be accounted for while calibrating). The measured signals are cross-correlated and time averaged by the correlator. If the correlator averages the signal every  $t_{int}$  intervals, then the output of the correlator is given by Equation 2.6,

---

<sup>3</sup>the constant of proportionality is different for different frequencies.

$$\begin{aligned}
\Gamma(\tau) &= \frac{1}{t_{int}} \int_0^{t_{int}} E_1(t) \times \overline{E_2}(t) dt \quad (\text{where } \overline{E_2}(t) \text{ is the complex conjugate of } E_2(t)) \\
\Gamma(\tau) &= \frac{1}{t_{int}} \int_0^{t_{int}} E_o e^{i2\pi\nu t} \times E_o e^{-i2\pi\nu(t+\tau)} \\
\Gamma(\tau) &= \frac{1}{t_{int}} \int_0^{t_{int}} E_o^2 e^{-i2\pi\nu\tau} dt = \frac{1}{t_{int}} E_o^2 e^{-i2\pi\nu\tau} \int_0^{t_{int}} dt \\
\Gamma(\tau) &= E_o^2 e^{-i2\pi\nu\tau}.
\end{aligned} \tag{2.6}$$

From Section 2.2.1, we know that the intensity of the source is proportional to the square of the electric field, hence we can replace  $E_o^2$  in Equation 2.6 with the intensity  $I$  of the source (the constant of proportionality can be accounted for while calibrating). However, due to the direction dependant *primary beam*<sup>4</sup> response of the antenna, the intensity is attenuated by the primary beam gain  $A$  (dimensionless) for the given direction. Hence, Equation 2.6 can be re-written as

$$\Gamma(\tau) = A \times I \times e^{-i2\pi\nu\tau}. \tag{2.7}$$

Equation 2.7 is the complex cross-correlation of the signals measured by a single baseline as a function of the angular location of the radio source ( $\tau$ ), and hence the information about the source position in the apparent sky can be obtained from the phase of the complex measurement. In fact, when observing the real sky with a single baseline, the signals from all the sources contained within the primary beam are correlated. The interferometer's response to a source is linear, hence using the superposition principle the cross-correlation for  $m$  sources is given by

$$\Gamma(\tau) = \sum_{j=0}^m A_j \times I_j \times e^{-i2\pi\nu\tau_j} \tag{2.8}$$

---

<sup>4</sup>the angular response of the antenna.



### 2.2.3 An Interferometer's Response to the Apparent Sky

From the previous section, we know that we can resolve sources parallel to the orientation of a baseline by varying the delay of its cross-correlation function. Most modern radio interferometers extrapolate this concept by using an array of antennas (with baselines in different directions) to resolve the sources in the 2D sky. In this section, I derive an interferometer's response to the 2D sky signal.

Let  $l$  and  $m$  be two orthogonal direction cosines that define the apparent sky as measured from a phase centre<sup>5</sup> ( $s_o$ ) as shown in panel B of Figure 2.3. If we define the 2D sky intensity distribution as  $I(l, m)$  and the telescope's primary beam response as  $A(l, m)$ , the measured cross-correlation (hence forth called visibility) in Equation 2.8 can be re-defined as

$$V = \int_{4\pi} A(l, m)I(l, m)e^{-i2\pi\nu\tau} d\Omega. \quad (2.9)$$

The baselines of the array are measured in uvw Cartesian coordinates, as shown in Figure 2.3. The w-axis is pointed towards the phase centre, while the u and v axes are along the l and m direction cosines. Every baseline in the array is defined using its uvw projection. Note that the uvw coordinates are expressed in wavelengths.

If we define the position of other sources within the primary beam as a vector sum from the phase  $s = s_o + \sigma$  (as shown in panel A of Figure 2.3), we can re-write the delay as  $\nu\tau = D.s = D.(s_o + \sigma)$ . Thus, from Equation 2.9, we get

$$V(u, v, w) = \int_{4\pi} A(l, m)I(l, m)e^{-i2\pi(D.[s_o+\sigma])} d\Omega. \quad (2.10)$$

Also, from trigonometry we know that

---

<sup>5</sup>in previous section, the zenith was considered as the phase centre and the position of other sources was measured from the zenith. For a given observation, any arbitrary direction can be considered as the phase centre and can also be changed post observation.

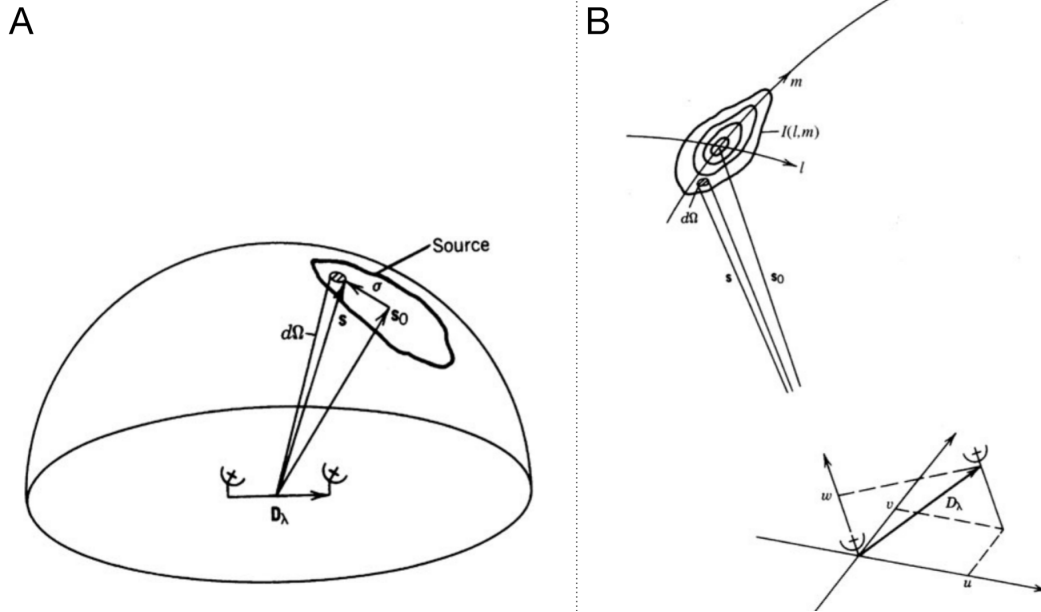


Figure 2.3: The coordinate system used for defining sky brightness distribution and baseline projections (image adapted from Thompson et al. (2017)).

$$\begin{aligned}
 D \cdot s_o &= w \\
 D \cdot \sigma &= ul + vm + w\sqrt{1 - l^2 - m^2} \\
 d\Omega &= \frac{dl \times dm}{\sqrt{1 - l^2 - m^2}}.
 \end{aligned} \tag{2.11}$$

Substituting the values from Equation 2.11 in 2.10, we obtain

$$V(u, v, w) = \iint \frac{A(l, m)I(l, m)}{\sqrt{1 - l^2 - m^2}} \times e^{-2\pi i(ul+vm)} e^{-2\pi iw(\sqrt{1-l^2-m^2}-1)} dl dm. \tag{2.12}$$

Equation 2.12, is the visibility function that defines a baseline's response to the 2D sky signal.

### 2.2.3.1 UV Coverage and the Point Spread Function

All baselines together sample the sky signal in  $(u, v, w)$  coordinates (or commonly called the uv coverage). An interferometer's ability to recover the true sky signal

is limited by its uv-coverage. If we define the uv sampling function of the interferometer as  $S(u, v)$  (assuming a narrow primary beam, i.e,  $w \approx 0$ ), then the reconstructed image  $I_{dirty}(l, m)$  is given by

$$I_{dirty}(l, m) = \mathcal{F}\{V(u, v) \times S(u, v)\}, \quad (2.13)$$

where  $\mathcal{F}$  is a Fourier transform (note that the images and visibilities share a 2D Fourier relationship and more information on imaging is provided in Section 2.2.4). The visibilities sampled by each baseline determines the spatial scales resolved in a given direction, and an ensemble of baselines together define the instrument's 2D response to the sky (Point Spread Function [PSF]). The spatial scales resolved by a single baseline of length  $d$  is determined by  $\approx \lambda/d$  (due to the diffraction limit), and hence the maximum resolution of the interferometer in a given direction can be obtained from the diffraction limit of the longest projected baseline.

Using the convolution theorem  $\mathcal{F}\{A \times B\} = \mathcal{F}\{A\} \otimes \mathcal{F}\{B\}$  (Bracewell & Bracewell, 1986) and the Fourier relationship between the visibilities and the sky, Equation 2.13, can be re-written as

$$\begin{aligned} I_{dirty}(l, m) &= \mathcal{F}\{V(u, v)\} \otimes \mathcal{F}\{S(u, v)\} \\ I_{dirty}(l, m) &= I_{true}(l, m) \otimes PSF(l, m), \end{aligned} \quad (2.14)$$

where  $I_{true}(l, m)$  is the true sky being sampled and  $PSF(l, m)$  is the instrument response. The array configuration, uv coverage, and the reconstructed sky image for the MWA Phase 1, Phase 2 extended, and Phase 2 compact configurations are shown in Figure 2.4. The corresponding PSFs for the three observations can be found in the insert panel within the re-constructed image. We note that the PSF of the compact configuration is much wider (hence lower resolution) than the other two array configurations due to its very short baseline lengths. All  $6\sigma$  sources detected in the reconstructed images are shown using green contours. Note that many point sources detected by the Phase 1 and the Phase 2 extended

array are not detected by the Phase 2 compact array due to its lower resolution (sampling spatially compact radio sources using a PSF wider than the source results in reduced SNR, due to averaging the source signal over a larger area in the sky). Note that although the three different MWA configurations have the same total sensitivity/collecting area (no. of tiles), the spatial scales that they are sensitive towards are different.

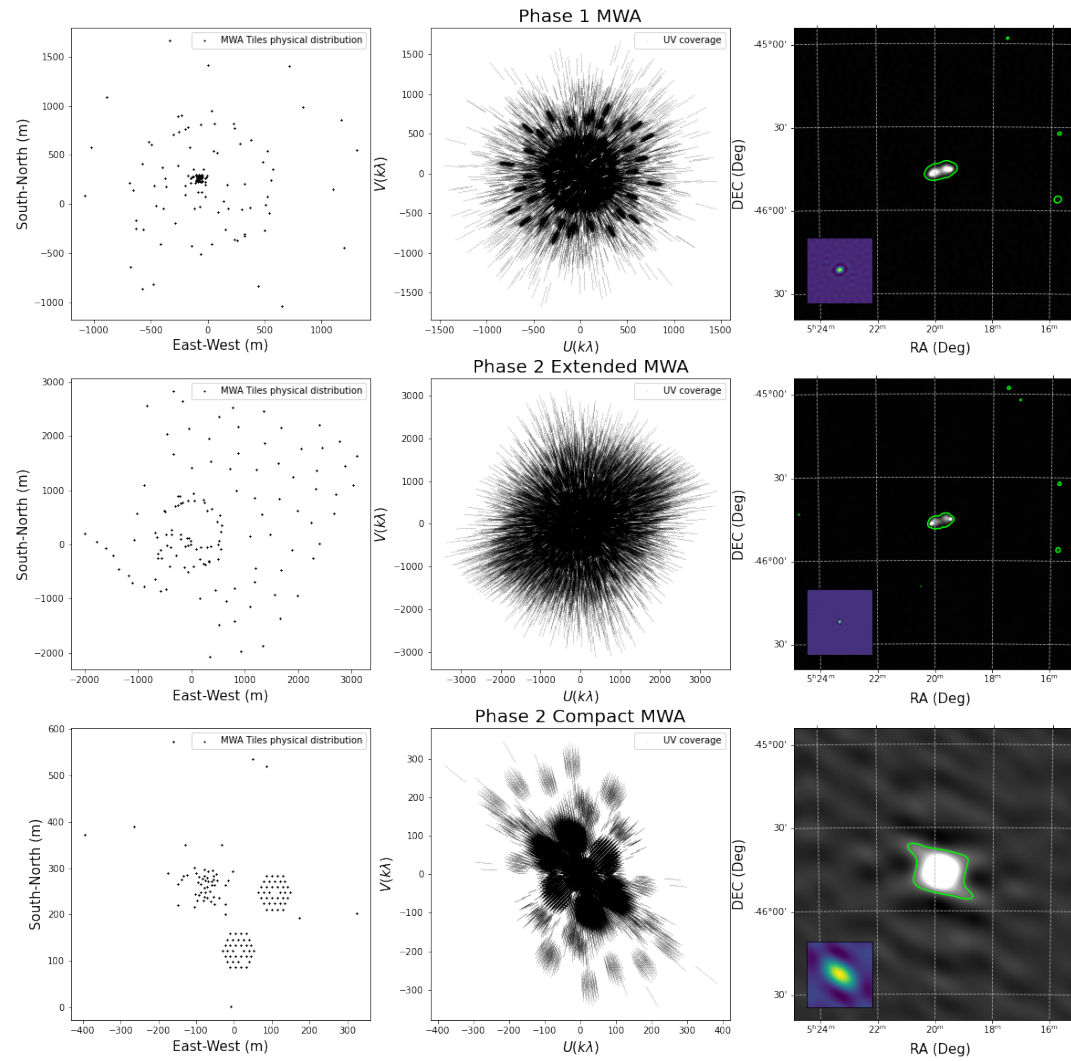


Figure 2.4: The physical array layout and uv coverage of MWA Phase 1, Phase 2 extended and Phase 2 compact configurations. All the three observations were performed over the same frequency band. The phase centres and the imaging parameters are also the same for the three observations.

## 2.2.4 Widefield Imaging using W-Stacking

For interferometers with a narrow primary beam, the sampled visibilities and the apparent sky signal can be approximated by a 2D Fourier relationship (by substituting  $w = 0$  in Equation 2.12). However, due to the non-coplanar configuration of the MWA tiles and due to its wide primary beam, the 2D Fourier relationship no longer holds as the visibilities are sampled in a 3D space. Large primary beam interferometers perform visibility inversion (imaging) by using methods such as W-projection (Cornwell et al., 2008), W-Stacking (Humphreys & Cornwell, 2011), 3D Fourier transforms (199, 1999), and faceting (Cornwell & Perley, 1992), that appropriately deals with the  $w$  dimension in visibility sampling. For the MWA, we use the W-Stacking method using the software WSClean (Offringa et al., 2014; Offringa & Smirnov, 2017) and the method is explained below.

The inverted form of the visibility, Equation 2.12, is given below (obtained from Offringa et al. (2014))

$$\frac{I(l, m)A(l, m)}{\sqrt{1 - l^2 - m^2}} = e^{2\pi iw(\sqrt{1-l^2-m^2}-1)} \int \int V(u, v, w) \times e^{2\pi i(ul+vm)} du dv. \quad (2.15)$$

Due to the Fourier inversion being performed on a digital device (computer), the visibilities have to be binned into a regular grid prior to performing a 2D Fast Fourier Transform (FFT). The size of the grid determines the angular size of the pixel in the inverted image.

Upon gridding the visibilities to different discrete  $w$ -layers, we can integrate Equation 2.15 between  $w_{min}$  to  $w_{max}$ , which results in

$$\frac{I(l, m)A(l, m)(w_{max} - w_{min})}{\sqrt{1 - l^2 - m^2}} = \int_{w_{min}}^{w_{max}} e^{2\pi i w(\sqrt{1-l^2-m^2}-1)} \times \int \int V(u, v, w) e^{2\pi i(ul+vm)} du dv dw.$$

$$\text{re-constructed image} = \sum_w \text{Phase Correction} \times \text{2D FFT of discrete w-layer} \quad (2.16)$$

In the above equation, the term inside the double integral takes the form of a 2D Fourier transform and the exponential term outside the double integral is a direction dependent phase correction that is different for every w-layer. Hence, from Equation 2.16, we see that the sky image over a wide field of view can be reconstructed by stacking a series of phase-corrected 2D-FFTs of the different w-layers.

#### 2.2.4.1 De-Convolution (CLEANing)

From Section 2.2.3.1, we know that the re-constructed sky image (or “dirty image”) is the true sky convolved with the PSF. The process of de-convolution (or CLEANing) aims to remove the PSF structure from the dirty images. Incomplete UV-coverage causes side-lobes in the PSF, resulting in increased side-lobe “confusion noise” in the dirty images. CLEANing helps detect faint sources within the primary beam by reducing the side-lobe confusion noise<sup>6</sup>. The steps involved in CLEANing are: 1) fitting a PSF model to the detected bright sources; 2) subtracting the fit PSF models (starting from the brightest source); and 3) restoring the subtracted sources back into the image using a Gaussian model of the PSF.

The WSClean software performs de-convolution using Högbom’s CLEAN algorithm (Högbom, 1974). The Högbom method fits a PSF model to sources in the dirty images and subtracts the corresponding modeled visibility (using Equation 2.12) from the measured visibilities in the UVW grid. Due to the large primary

---

<sup>6</sup>side-lobe confusion noise is not random but is systematic in nature, and hence can be subtracted

beam of the MWA, PSF subtraction of the detected sources in the visibility domain is computationally less expensive than generating PSF models for every direction within the large primary beam<sup>7</sup> and performing an image based source subtraction.

However, throughout this thesis MWA dirty images were often used for performing satellite detections<sup>8</sup>, and CLEAN was only performed for either improving the calibration through self-calibration (explained in Section 2.2.5) or in some very exceptional cases (e.g, parallax analysis done in Chapter 4 where images of different resolutions had to be compared and hence sources are subtracted and restored).

## 2.2.5 Calibration

The time-varying behaviour of the antenna gain and phase, can result in intensity and angular position discrepancies between the true sky and the reconstructed sky. The process of calibration solves for the gain and phase for every antenna element of the interferometer by using a reference model.

For the MWA, we use sky based calibration, where we solve for antenna gain/phase using a prior model of the apparent sky. Throughout this thesis, either the GaLactic and Extra-galactic All sky MWA (GLEAM) (Hurley-Walker et al., 2017) survey sources within the primary beam of the observation or models of bright radio-galaxies such as Hydra-A, Fornax-A, and Pictor-A are used to perform calibration. For a given sky model, we can create model visibilities for every baseline (using Equation 2.12) and the process of calibration tries to minimise the difference between  $(V_{data} \times A) - V_{model}$  by iteratively varying the complex gain  $A$  of the antenna pair.

During calibration, an imperfect (or incomplete) model of the sky can result

---

<sup>7</sup>Due to differences in projected baselines, the PSF varies largely over the large FOV.

<sup>8</sup>Due to imaging in every fine channel and time-step, CLEANing all the images proved to be a computationally expensive task with marginal improvement. Also, due to using difference images, if either of the used images had a different depth of CLEANing it would result in imaging artifacts/false-positives.



in calibration errors. Model visibilities created using incomplete knowledge of the sources within the primary beam of the observation can result in increased noise (as they do not accurately represent the total flux density measured by the instrument) in the re-constructed image. This issue is often addressed by performing self-calibration, where we improve the calibration solution by using the CLEAN model of the sky obtained during de-convolution <sup>9</sup>.

### 2.2.6 The MWA Signal Chain

An MWA (Tingay et al., 2013a) tile has 16 dual polarised bow-tie antennas arranged in a  $4 \times 4$  grid configuration, as shown in Figure 1.4. The signals from the 16 antennas are combined in phase to create a coherent primary beam by the analogue MWA beamformer. The beamformer has switchable delay lines that enable the primary beam to be steered across the sky.

The analogue signals from every 8 tiles (16 independent voltage streams due to observing in two polarisations) are sent to the MWA receivers (Prabu et al., 2015). The MWA has 16 receivers that are spread across the array such that no single tile is more than 500 m away from its receiver. The receiver amplifies and band limits the incoming signals (to 80 – 300 MHz), and then channelising the data further to the required 30.72 MHz wide digitised (5 real + 5 complex bits) output. This is also the coarse channelisation step in the MWA signal chain, as the 30.72 MHz bandwidth output is in the form of 24 coarse channels (1.28 MHz each). The output from the receivers are then sent to the on-site Central Processing Facility (CPF).

The in-coming wide-band data are further channelised to 10 kHz fine frequency channels before being correlated at the CPF. The MWA’s correlator (Ord et al., 2015) is a GPU-based software run real-time on 24 servers. Once correlated, the

---

<sup>9</sup>during CLEANing, the model column of the measurement set gets populated with model visibilities for every source subtraction performed during CLEANing and this model column is used for performing self-calibration

visibilities are sent for storage at the Pawsey Supercomputing Centre<sup>10</sup> in Perth, for further analysis. The raw “gpubox” visibility files or the CASA (McMullin et al., 2007) measurement sets for the observations can be downloaded by the user from the MWA All-Sky Virtual Observatory<sup>11</sup> (ASVO) for further analysis.

### 2.2.6.1 Phase 2 Upgrade

The MWA underwent an upgrade to Phase 2 during 2016 (Wayth et al., 2018). The Phase 2 array uses the same hardware as described in Section 2.2.6, but has an additional 128 deployed tiles at the MRO. “The Phase II MWA [is] periodically reconfigured between *compact* and *extended* configurations, each of which contains 128 operating tiles” (Wayth et al., 2018). The physical array configuration for the Phase 1, Phase 2 compact, and Phase 2 extended configurations are shown in Figure 2.4.

Fifty six of the new tiles are spread outside the Phase 1 diameter, up to a distance of 5.3 km. These long baselines provide a 1.1 arc-minute synthesised beam when observing at 150 MHz (as compared to 2 arc-minute beam for Phase 1 at the same frequency). The remaining 72 tiles are arranged as two regular hexagonal cores. The tile configuration of the compact configuration was driven by the increased sensitivity towards extended emission as required by Epoch Of Re-ionisation (EOR) science experiments (key science for the MWA). The regular tile arrangements of the compact configuration also help perform redundant baseline calibration for EOR observations (Li et al., 2018).

### 2.2.6.2 The MWA as a Radar System

The MWA is able to observe the radio sky using its standard operation mode (aperture synthesis methods explained in this thesis) and also by performing coherent searches using its Voltage Capture System (VCS) (Tremblay et al., 2015) mode. Only the standard MWA operation mode is used in this thesis, and hence

---

<sup>10</sup><https://pawsey.org.au/>

<sup>11</sup><https://asvo.mwatelescope.org/>

the developed methods are called “non-coherent passive radar techniques”. More information on coherent passive radar with the MWA can be found in [Palmer et al. \(2017\)](#), [Hennessy et al. \(2019\)](#) and [Hennessy et al. \(2020\)](#).

## 2.3 Orbital Mechanics

The motion of a gravitationally bound (in a circular or elliptical orbit) satellite around the Earth can be defined by

$$\frac{\delta \vec{v}}{\delta t} = -\frac{\mu}{r^3} \vec{r}, \quad (2.17)$$

where  $\vec{v}$  and  $\vec{r}$  are the instantaneous velocity and position vectors of the satellite measured in an inertial reference frame, and  $\mu$  is the gravitational parameter of Earth ( $3.98 \times 10^{14} \text{ m}^3 \text{ s}^{-2}$ ). The vectors  $\vec{v}$  and  $\vec{r}$  are together called the *state vectors* of the object, as its velocity and position at any other instant can be determined as a linear combination of its initial state using Equation 2.18. Note that six independent<sup>12</sup> values (three orthogonal components of  $\vec{r}$  and three orthogonal components of  $\vec{v}$ ) are required to uniquely define an orbit,

$$\begin{aligned} \vec{r}_t &= f \vec{r}_o + g \vec{v}_o \\ \vec{v}_t &= \dot{f} \vec{r}_o + \dot{g} \vec{v}_o. \end{aligned} \quad (2.18)$$

In Equation 2.18,  $f$ ,  $g$ ,  $\dot{f}$  and  $\dot{g}$  are called Lagrange coefficients and their values depend on the initial state and the time difference between the two epochs (more information on how to determine these values can be found in Chapter 2 of [Curtis \(2013\)](#)).

We decompose the six independent values to a combination of Euler rotation angles (argument of perigee  $\omega$ , inclination  $i$ , right ascension of ascending node  $\Omega$ ) that define the 3D orientation of the orbit, parameters that define the shape of the orbit (eccentricity  $e$ , semi-major axis  $sma$ ), and a parameter that locates

---

<sup>12</sup>Although, if the object is in a perfectly circular orbit, the 6<sup>th</sup> value can be determined using the condition that the  $\vec{v}$  and  $\vec{r}$  vectors are perpendicular.



The SGP propagator model uses mean orbital elements as compared to osculating elements (the instantaneous orbital elements of the satellite. The osculating elements are constantly varying with time due to the perturbations discussed above). However, osculating elements are used in satellite conjunction monitoring in order to accurately examine the situation. In this thesis we limit ourselves to use mean orbital elements to propagate satellites due to not having access to higher order propagation software as well as to reduce the computational cost involved.

### 2.3.1 Two Line Elements

The Space Surveillance Network (SSN) catalogues all discovered human-made objects (above a diameter of 10 cm) in space using North American Aerospace Defense (NORAD) IDs and publicly releases their mean orbital elements in the Two Line Element (TLE) format. The TLE<sup>13</sup> contains the mean orbital elements of the object measured at a given epoch, along with additional information regarding launch year for the object, epoch of measurement, atmospheric drag coefficients, and check-sums (to identify any bit-flips while electronically transmitting TLEs). Using the TLEs we can predict the state vector of the object (for a few days near the epoch of observation) using an SGP model. There are many Python packages (such as `Skyfield`<sup>14</sup> and `PyEphem`<sup>15</sup>) that can read TLEs and determine the state vectors of the object near the epoch of observation, and these packages are used throughout this thesis<sup>16</sup> Note that the PSF of the MWA Phase 2 Hex observations used in this thesis has an FWHM of about 15 arc minutes (for near zenith pointings) and any fractional uncertainties in `Skyfield/PyEphem`

---

<sup>13</sup>more information on TLE format can be found in <https://www.celestrak.com/NORAD/documentation/tle-fmt.php>

<sup>14</sup><https://rhodesmill.org/skyfield/>

<sup>15</sup><https://rhodesmill.org/pyephem/>

<sup>16</sup>`PyEphem` is computationally faster than `Skyfield` and was used during early parts of this thesis. However, `Skyfield` is more accurate in predicting the angular positions of the satellite and hence was incorporated into the pipelines to replace `PyEphem` in the second half of this thesis (during Python 2 to Python 3 migration).

orbit propagations would still be within our reported angular measurement errors. Also, as the main focus of this thesis is to contribute towards the data acquisition part of the SDA framework discussed in Section 1.3, the brief introduction to TLEs given in this section is sufficient to follow research performed in the following chapters.

## 2.4 Summary

In this chapter I have briefly discussed methods associated with aperture synthesis using the Murchison Widefield Array. I explain the dependence of the measured visibility by a baselines on the primary beam response, sky brightness distribution, frequency of observation, and the projected baselines geometry. I also discuss the W-Stacking method used for imaging the MWA's wide-field of view and the calibration methods associated with it. I conclude the chapter by giving an introduction to the MWA signal chain and a preliminary description of orbital mechanics required to follow the rest of this thesis.

# Chapter 3

## Dynamic Spectrum Analysis and Classification of Satellite Signals

This chapter is a reproduction of Prabu, S. Hancock, P. Zhang, X. Tingay, S.J, “The development of non-coherent passive radar techniques for space situational awareness with the Murchison Widefield Array”, Publications of the Astronomical Society of Australia , Volume 37 , 2020 , e010, DOI: <https://doi.org/10.1017/pasa.2020.1>. It differs from the original in minor text edits to ensure consistency within this thesis. The reader will encounter some repetition of material in the introductory sections.

### 3.1 Abstract

The number of active and non active satellites in Earth orbit has dramatically increased in recent decades, requiring the development of novel surveillance techniques to monitor and track them. In this paper, we build upon previous non-coherent passive radar space surveillance demonstrations undertaken using the Murchison Widefield Array (MWA). We develop the concept of the Dynamic Signal to Noise Ratio Spectrum (DSNRS) in order to isolate signals of interest (reflections of FM transmissions of objects in orbit) and efficiently differenti-

ate them from direct path reception events. We detect and track Alouette-2, ALOS, UKube-1, the International Space Station, and Duchifat-1 in this manner. We also identified out-of-band transmissions from Duchifat-1 and UKube-1 using these techniques, demonstrating the MWA’s capability to look for spurious transmissions from satellites. We identify an offset from the locations predicted by the cataloged orbital parameters for some of the satellites, demonstrating the potential of using MWA for satellite catalog maintenance. These results demonstrate the capability of the MWA for Space Situational Awareness and we describe future work in this area.

## 3.2 Introduction

The rising number of human-made objects in Earth orbit could lead to an increasing number of collision events between these objects. In the extreme limit, the Kessler effect (Kessler & Cour-Palais, 1978) is predicted to occur when the space density of objects increases beyond a critical value and a single collision leads to a cascade of collisions, rendering the entire orbit useless for future space missions (Kessler et al., 2010). An average of 21 satellite collision warnings are issued by the US military every day (Witze, 2018) and most of these objects are in Low Earth Orbit (LEO) with speeds of approximately 8km/s. Many small satellites have very little on-board fuel for position-keeping and a single collision avoidance manoeuvre can reduce the operation life-time of the satellite drastically (Schaub et al., 2015). Also, many CubeSats and NanoSats do not have on-board propulsion systems and these satellites pose a threat to other operational satellites in orbit.

A well known example of these risks being realised was when two satellites (Iridium-33 and Kosmos-2251) collided in 2009 (Kelso, 2009). The density of objects in LEO has further increased in the past decade due to the testing of anti-satellite capabilities by China (Kelso, 2007), India (Akhmetov et al., 2019), Russia (Johnson-Freese & Burbach, 2019) and the United States (Pardini & Anselmo,



2009). These objects in orbit are monitored and cataloged by the Space Domain Awareness (SDA) (Bobrinsky & Del Monte, 2010) program run by the European Space Agency (ESA) and the Space Surveillance Network (SSN) (R. Sridharan, 1998) run by the US. Both these organisations have been expanding their sensor networks in order to be able to detect and track multiple objects at any given time. However, due to companies such as SpaceX planning to launch mega-constellations (Radtke et al., 2017) in the future, a much larger number of sensors have to be utilised in order to accommodate the growth rate of satellites in LEO.

Radio interferometers such as Long Wavelength Array (LWA) (Taylor et al., 2012; Helmboldt et al., 2014) and LOw Frequency ARray (LOFAR) (van Haarlem et al., 2013; Gaussiran II et al., 2004) have detected reflections of non-cooperative transmitters from objects like meteors and aircrafts using correlated data in the past. In this work, we explore the use of the Murchison Widefield Array (MWA) for passive space surveillance in the FM band, building upon previous work. The transmitter-target-receiver architecture used in this work is similar to the GRAVES radar<sup>1</sup> except that we use interferometric correlated data and non-cooperative terrestrial FM transmitters.

The MWA is a low frequency (70 – 300 MHz) radio interferometer built as a precursor to the Square Kilometre Array (SKA) (Tingay et al., 2013a), located at the radio-quiet Murchison Radio-astronomy Observatory (MRO) in Western Australia. The MRO is one of two sites where the SKA will be built in the future. While the MWA has been designed and built with a primary mission for astrophysics and cosmology (Bowman et al., 2013; Beardsley et al., 2019), the facility has been shown to be a novel and effective instrument for SDA studies, utilised as part of passive radar systems that use terrestrial FM broadcasts as non-cooperative illuminators of opportunity for objects in Earth orbit. The MWA represents a highly sensitive receiver of FM signals reflected off orbiting objects.

The MWA has been used previously to detect the International Space Station

---

<sup>1</sup><https://www.onera.fr/en/news/graves-space-surveillance-system>

(ISS) by using non-coherent (Tingay et al., 2013b) and coherent (Palmer et al., 2017) passive radar detection techniques. In coherent detection, the signal transmitted by the FM station is used as a reference for designing matched filters to search for reflection events, while in non-coherent detection, the search is done using interferometer correlated data in the image domain. In this paper, we focus on the development of non-coherent techniques for space surveillance by the MWA. The development of coherent techniques is described by (Hennessy et al., 2019) and in an upcoming article by Hennessy et al. (2019, IEEE submitted).

Tingay et al. (2013b) carried out observations during the commissioning phase of the MWA as a proof-of-concept for the non-coherent passive radar technique. This work detected the ISS, using the transmissions reflected off the ISS from a variety of terrestrial FM radio stations. Tingay et al. (2013b) also published electromagnetic simulations, predicting that debris with a radius greater than 0.5 m could be detected by the MWA via FM reflections at ranges up to 1000 km, with a 1 s integration time and a 50 kHz bandwidth.

Using similar techniques, the MWA has also been used to search for meteors (Zhang et al., 2018), based on possible intrinsic radio emission, as seen at lower frequencies by the Long Wavelength Array (Taylor et al., 2012; Ellingson et al., 2013; Obenberger et al., 2016), or the reflection of FM radio waves from the ionisation trails left by meteors. In Zhang et al. (2018), the static celestial sources in their images were removed using difference imaging techniques, leaving non-static meteors visible as transient signals in the difference images. During these observations, some apparent FM reflections from satellites were also detected (of objects much smaller than the ISS) but were not investigated in detail. The current paper undertakes a comprehensive examination of these detections and extends the difference imaging techniques of Zhang et al. (2018), to improve the detection of objects in Earth orbit for the purposes of SDA using non-coherent passive radar techniques with the MWA.

This paper is compiled as follows. In Section 3.3 we discuss the observations

and the data processing analysis. Section 3.4 describes the results obtained from our analysis. The results and conclusions are discussed in Sections 3.5 and 3.6.

## 3.3 Observations and Data Processing

### 3.3.1 Observations

All of the observations we have utilized are zenith pointing drift scans from Phase 1 of the MWA (128 tiles distributed over a  $\sim 3$  km diameter area), observing the sky at 72.335 – 103.015 MHz (arranged as  $24 \times 1.28$  MHz coarse channels). The motivation behind choosing zenith pointed observations is two-fold. Firstly, it is the direction with the most sensitive MWA primary beam response. Secondly, satellites near the zenith have the shortest line-of-sight distance<sup>2</sup> and hence would be the most sensitive direction for detecting satellites. Although zenith does not have any favourable reflection geometry for satellite reflections, the MWA’s primary beam centred at the zenith is large enough to incorporate most of the favourable directions. Table 3.1 contains the list of the dates and times of these target observations and the identification of the objects detected (along with some characteristics of those objects). Also listed in Table 3.1 are the calibrator sources associated with the observations.

---

<sup>2</sup>Note that the received power in a passive radar is inversely proportional to distance<sup>4</sup>.

Table 3.1: List of observations and identified target objects within those observations.

Observation ID	Date UT	Start UT	Stop UT	Target/ Calibrator	Range to Target (km)	RCS <sup>a</sup> (m <sup>2</sup> )	Required TLE Offset (s)
1102604896	2014-12-14	15:07:58	15:11:50	Alouette-2	2184.9 - 2298.0	0.985	9.0
1102627456	2014-12-14	21:23:58	21:25:50	Hydra A			
1142340880	2016-03-18	12:54:22	12:58:14	ALOS	712.8 - 751.8	13.593	1.0
1142332016	2016-03-18	10:26:38	10:29:34	Pictor A			
1142351440	2016-03-18	15:50:22	15:54:14	UKube-1	653.3 - 688.8	0.118	1.75
1142332016	2016-03-18	10:26:38	10:29:34	Pictor A			
1142425368	2016-03-19	12:22:30	12:26:22	ISS	437.4 - 501.2	399.052	0.0
1142418344	2016-03-19	10:25:26	10:28:22	Pictor A			
1142521608	2016-03-20	15:06:30	15:10:22	Duchifat-1	623.3 - 710.8	0.037	1.25
1142504680	2016-03-20	10:24:22	10:27:18	Pictor A			

<sup>a</sup>Radar Cross Section (RCS) obtained From <https://celestrak.com/pub/satcat.txt>

All the above targets/calibrator were observed at 72.335 – 103.015 MHz. The range to target is the maximum and minimum line of sight distance at which the target was detected. Alouette-2 is also seen briefly in the observation 1102605136 (spanning from UTC 2014-12-14 15:12:00.00 to 2014-12-14 15:15:52.00), but was not used for the analysis performed in this paper.

### 3.3.2 Data Processing

The visibility data for the observations in Table 3.1 were downloaded as measurement sets (McMullin et al., 2007) from the MWA node of the All-Sky Virtual Observatory<sup>3</sup> (ASVO). Time averaging of 2 s (4 s for observations containing the Alouette-2 satellite, for reasons explained later) was used along with frequency averaging of 40 kHz. The first and last 80 kHz, along with the central 40 kHz of every 1.28 MHz coarse frequency channel was flagged due to the characteristics of the band-pass filter. The ASVO uses COTTER (Offringa et al., 2015) to convert native MWA format visibility files to measurement sets. RFI detection in COTTER was disabled when retrieving the target observations, so that the signals of interest were not automatically flagged. However, ASVO does apply the hardware flagging to data that is performed on-site.

The target observations were calibrated using calibration observations from the same night. The calibration observations were retrieved from the ASVO using the same parameters as the target observations but with RFI detection enabled in COTTER, in order to obtain good calibration solutions. The calibration observations were additionally pre-processed using AOFLAGGER (Offringa et al., 2015) to flag all the baselines in time and frequency with RFI in them.

When generating calibration solutions from the calibration observations, solutions for the times and frequencies flagged due to RFI were determined by interpolating the solutions across these times and frequencies. This was essential as we did not want the flags due to RFI in the calibration observations to be carried across to the target observations during calibration transfer.

Once the target observations were calibrated, they were imaged using WSCLEAN (Offringa et al., 2014; Offringa & Smirnov, 2017) at every 2 s timestep (4 s for Alouette-2) and at every 40 kHz fine frequency channel. As we perform our satellites detections using difference imaging (explained later in detail), we need to select integration timescales such that the satellite has moved more than

---

<sup>3</sup><https://asvo.mwatelescope.org/dashboard>

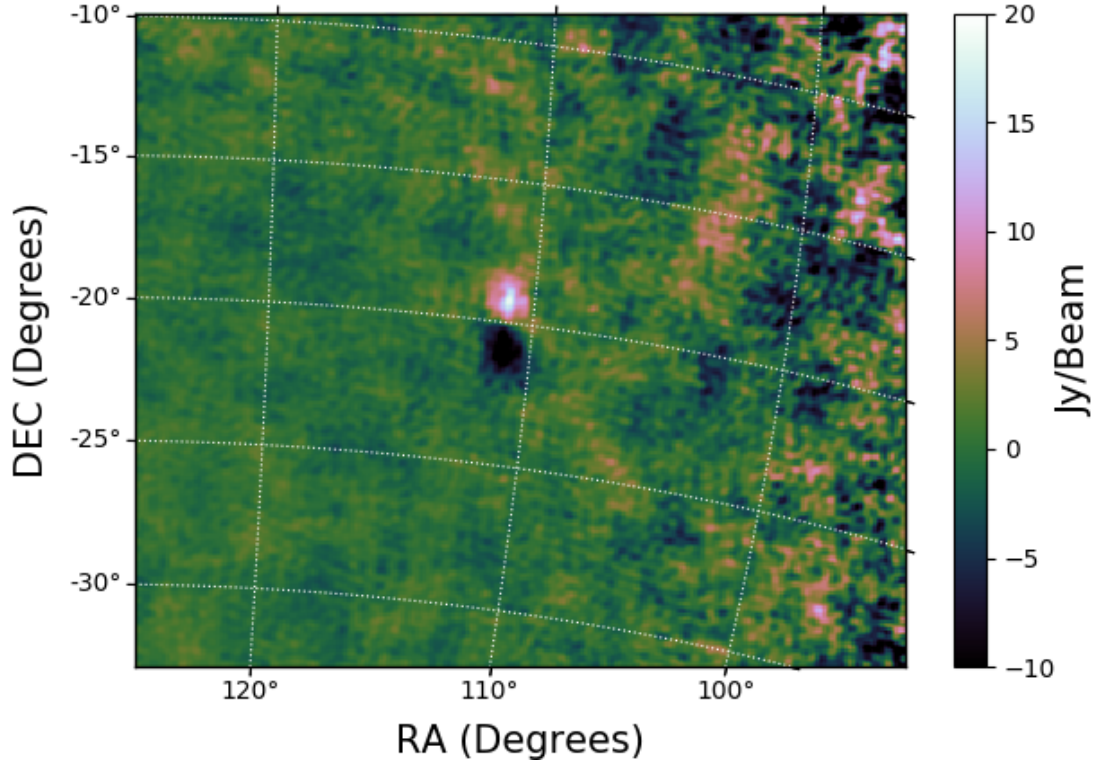


Figure 3.1: Primary beam corrected 30.72 MHz bandwidth difference image of ALOS centered at 87.675 MHz. ALOS is a remote sensing satellite orbiting at an altitude of about 690 km and has an RCS of  $13.6 m^2$ . The satellite also has large solar panels, that when fully deployed have an RCS of  $66.0 m^2$ .

in 1 synthesised beam in order to be detected in the difference images. Hence, we choose 4 s for Alouette-2 due to its lower angular speed compared to the other much faster satellites detected in this work.

In interferometer theory, a source is considered to be in the far-field if the received wave-front is planar as seen by a baseline of length  $D$ . The transition between the near-field and the far-field (the Fraunhofer distance) is given by  $d = 2D^2/\lambda$  where  $\lambda$  is the observing wavelength. Some satellites considered in this work are within a few hundred kilometers of the MWA, which puts them into the near field as seen by the MWA's longest baselines (3 km). Consequently we restrict our analysis to baselines shorter than 500 m in order to avoid near-field effects (Zhang et al., 2018). Natural weighting was also used for all objects.

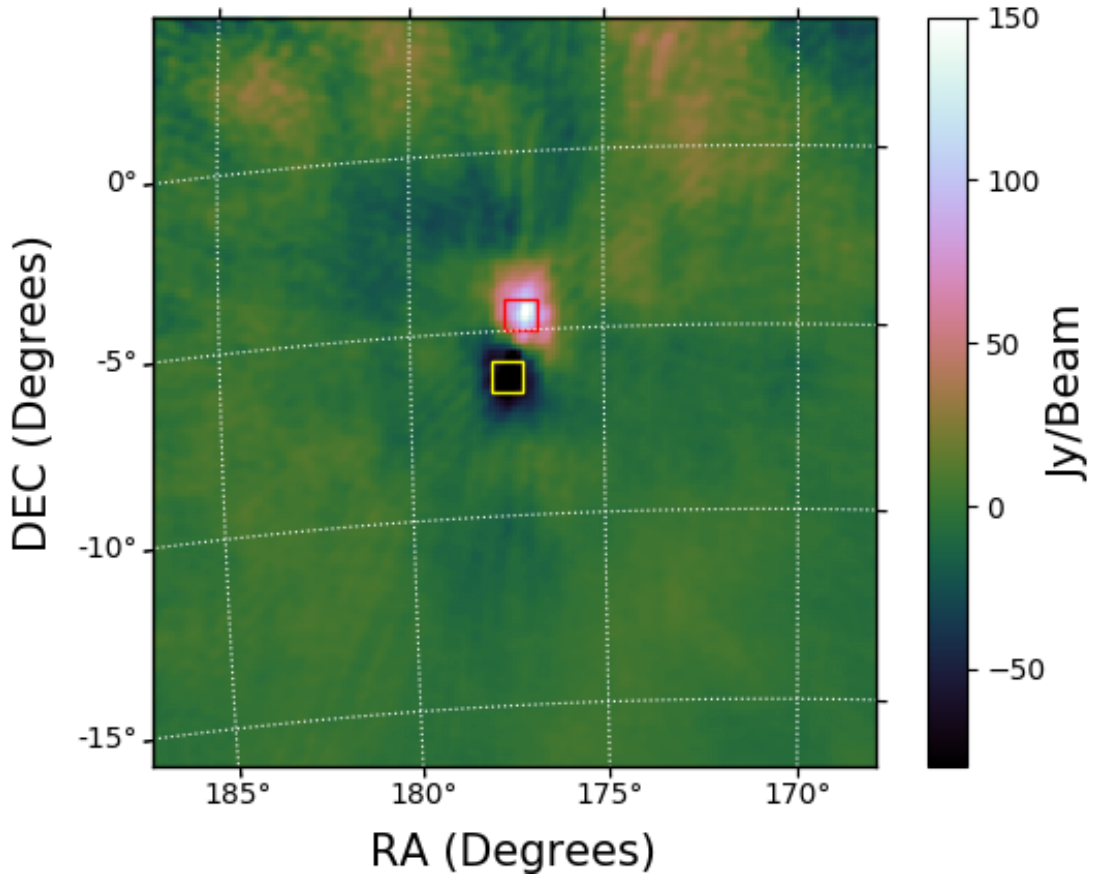


Figure 3.2: Primary beam corrected 30.72 MHz bandwidth difference image of UKube-1 centered at 87.675 MHz. UKube-1 is a 3 Unit CubeSat. The figure also shows the box make by the automated DSNRS script used for integrating flux density in the head and the tail of the streak.

CLEAN was not used, as the step after imaging is to form difference images, which removes the celestial sources and their side-lobes. Pseudo Stokes I images (i.e, without the primary beam correction) were made from the data and were used for the analysis described in Section 3.3.3.

We also produced images of the full 30.72 MHz bandwidth using multi-frequency synthesis, again at every time step. However, the full bandwidth images combine lots of channels with no signal and reduce the signal to noise ratio. Hence, we use these images only for preliminary detection (and position verification) as manual inspection<sup>4</sup> of difference images from every fine channel was not feasible.

<sup>4</sup>this step is automated from Chapter 4 onward by developing a source-finding software that

These images were made in XX and YY polarisations, which were primary beam corrected before combination, to produce a primary beam corrected Stokes I, full bandwidth image.

The data reduction pipeline used in this work incorporates the difference imaging technique that was found to work effectively by [Zhang et al. \(2018\)](#). Once imaged, difference images were formed at each time step  $t$  by subtracting the image at time step  $t - 1$  from the image at time step  $t$ . The difference images remove the persistent celestial sources, along with their side-lobes, thus greatly reducing the side-lobe confusion noise in the difference images. The difference images reveal objects that move rapidly<sup>5</sup> in Right Ascension and Declination (such as satellites, orbiting debris, planes, and long duration meteors) as streaks, characterised by a positive intensity head (in the direction of motion of the object) and a negative intensity tail. The phase centres of these images were fixed at the pointing centres of the MWA beam for the observations (zenith in this case). Examples of difference images revealing such streaks due to the objects listed in [Table 3.1](#) are shown in [Figures 3.1](#) and [3.2](#).

### 3.3.3 Dynamic Signal to Noise Ratio Spectrum (DSNRS) Analysis

During the development of the imaging and difference imaging methodology, we noticed that the images could be affected by FM signals in two ways. First, the signal of interest was present, that being the FM signals reflected off objects in orbit and thus confined to a small region of the image plane. Second, FM signals could enter the MWA field-of-view by virtue of direct reception from the transmitter, via atmospheric ducting.

---

performs autonomous detections of satellites signals in ever fine-channel and time-step.

<sup>5</sup>objects that move more than one synthesised beam appear as streak signals in difference images. Often for the integration times (2s) used in this thesis, most LEO objects move about 0.8 – 2.0 degrees. Objects that move much slower get subtracted out while performing difference image. But such slow moving objects are much higher in altitude and are not within the predicted detection parameter space of the MWA SDA system.



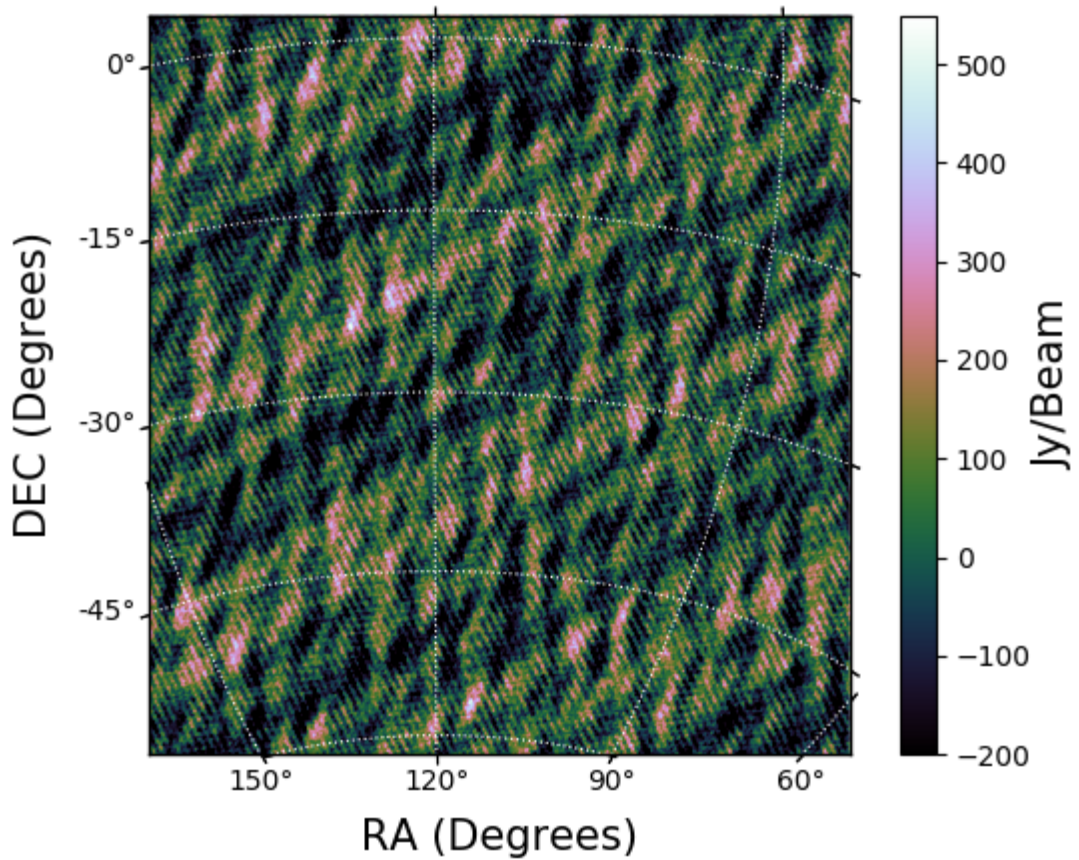


Figure 3.3: Difference image for one 40 kHz frequency channel with direct FM reception.

When FM reflections are present in an image, the signals are highly localised in the image, corresponding to the locations of the objects reflecting the signals. In this case, the overall RMS in the image is very close to that of a thermal noise dominated image with no signal present.

However, when an image is affected by direct reception of FM signals, the overall image RMS is greatly increased relative to a thermal noise dominated image. For example, we show a difference image for one 40 kHz frequency channel affected by direct reception, and the variation of image RMS in difference images as a function of frequency, for one of the observations in Figures 3.3 and 3.4, respectively.

We utilised these characteristics to distinguish between reflected and direct

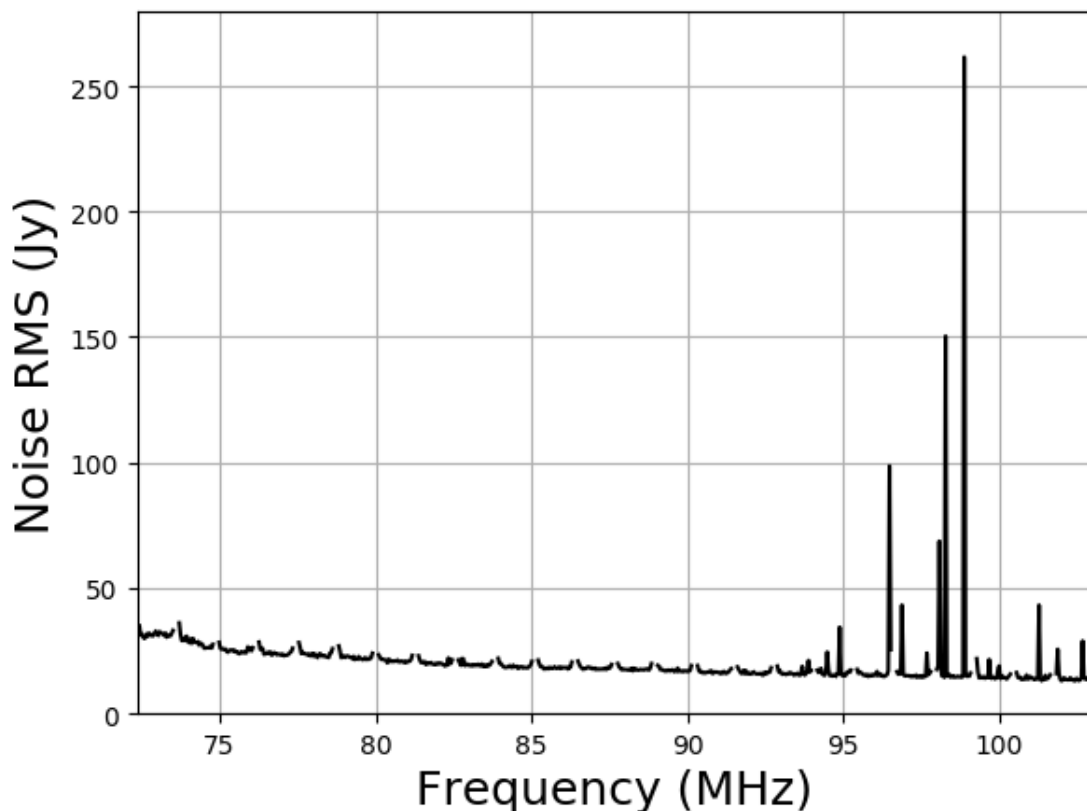


Figure 3.4: Plot showing the variation of noise RMS of difference images with frequency. Note that the plot is discontinuous at the centre and edge of every coarse channel due to flagging.

reception FM signals in our data and to isolate the signals of interest, as follows.

The archived Two Line Element (TLE) data<sup>6</sup> were obtained for the epochs at which the observations were made, for the relevant objects. The TLE data contain the orbital parameters at a given epoch along with the satellite ID. The Ephem<sup>7</sup> Python module was used to propagate the satellite using TLE data to the UTC time of the difference images.

<sup>6</sup>TLE data obtained from <https://space-track.org>

<sup>7</sup><https://pypi.org/project/ephem/3.7.3/>

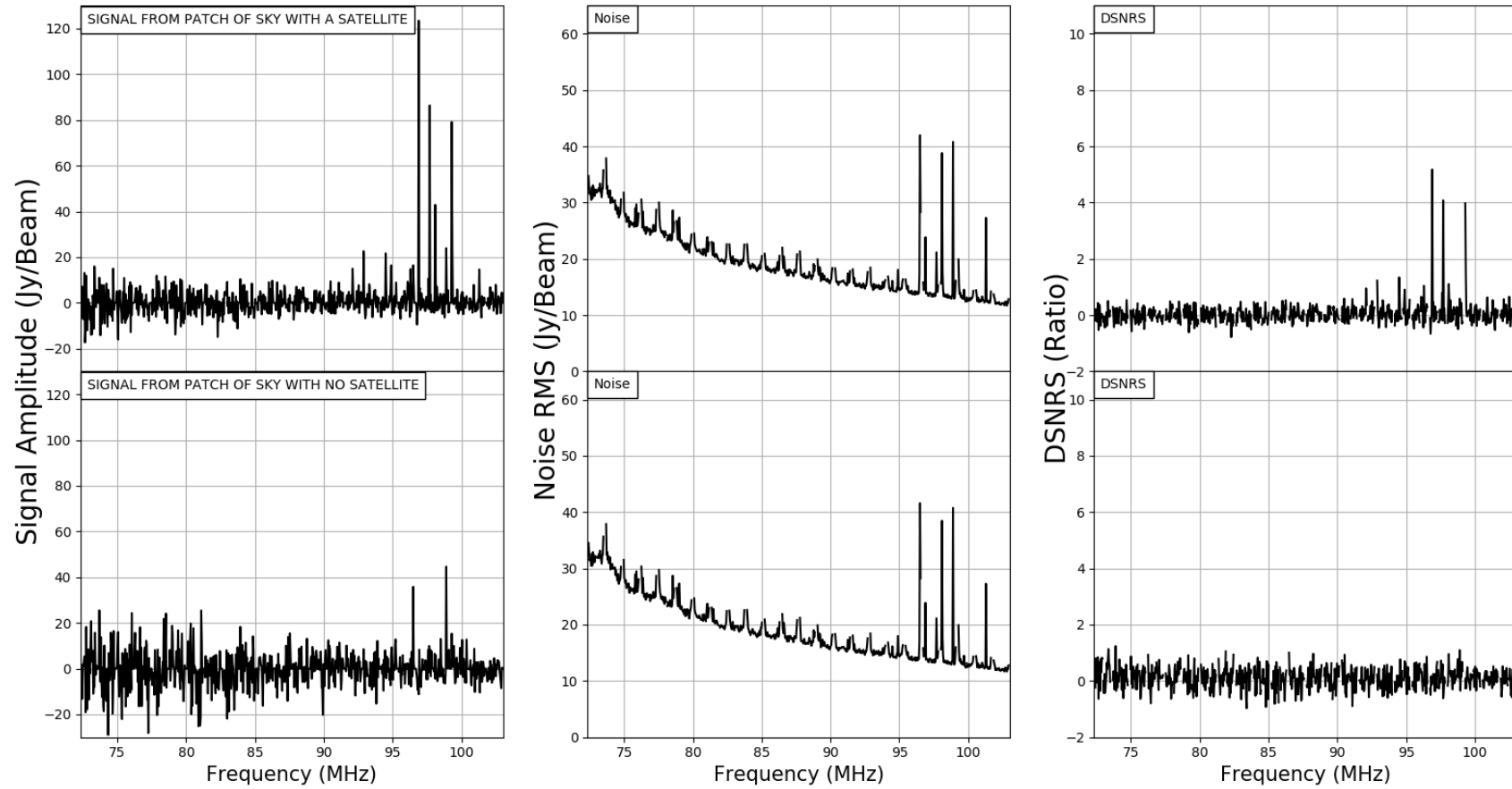


Figure 3.5: The left, middle and right panel show the numerator, denominator and the resultant value of Equation 3.1 when applied on a part of the sky with (top) and without (bottom) a satellite. Note the plot is discontinuous as the center and edge of every course channel due to flagging.

The predicted satellite location was used to form boxes around the head and the tail of the streak in the difference images, as shown in Figure 3.2. However, the predicted satellite position did not always exactly match with the MWA detections and time delays of a few seconds (given in Table 3.1) had to be provided to the Ephem module in order to make the predicted position coincide with the detection (note that the offset is not due to error in the instrument but due to the TLE for the satellites being outdated during the observation. As the observations are phase and amplitude calibrated using the background sky sources, the observed offset is unlikely to be from instrument effects. It is also not likely to be errors from the TLE propagation as they are significantly smaller than the PSF FWHM). The sizes of the boxes were calculated using the distance the satellite was predicted to move in the image plane, and to contain the majority of the signal at all times. These boxes were used to calculate the Dynamic Signal to Noise Ratio Spectrum (DSNRS) for all of the satellites. Due to the motion of these satellites being resolved, and the signal of interest being contained in the positive “head” and the negative “tail”, the DSNRS describes the mean signal contained in the boxes, divided by the RMS of the noise calculated in the image away from the signal, and is presented in Equation 3.1,

$$DSNRS(t, f) = \frac{\sum_{i=1}^N J_{Head}(t, f) - \sum_{k=1}^M J_{tail}(t, f)}{RMS(t, f)} = \frac{\sum_{i=1}^N J_{Head}(t, f) - \sum_{k=1}^M J_{tail}(t, f)}{RMS(t, f) \times (M + N)}, \quad (3.1)$$

where  $J_{Head}$  and  $J_{Tail}$  are the intensity (per pixel values) in the tail and the head of the streak in a difference image, respectively;  $N$  and  $M$  are the number of pixels in the head and the tail, respectively. RMS is the root mean square of the difference image calculated at time step  $t$  and at frequency  $f$ , at a region in the image containing no satellites. We negate the tail summation term in the above equation as the signal in the tail is negative. Both the numerator and denominator in Equation 3.1 have the dimensions of intensity (Jansky/beam),

thus the resultant value of Equation 3.1 is a dimensionless number that varies with time and frequency, hence the use of dynamic spectrum in our terminology. Note that we utilise the DSNRS as a qualitative detection metric, to identify the frequencies reflected by the satellite and to isolate those signals in image, time, and frequency space. The DSNRS metric, while a measure of signal-to-noise, does not imply any particular adherence to an underlying statistic. The noise term contains both Gaussian and complicated non-Gaussian components.

Figure 3.5 shows the utility of the DSNRS in isolating the reflected FM signals of interest in our difference images. In the bottom three panels of Figure 3.5, DSNRS was applied to a randomly selected location on the sky that did not contain a satellite. The bottom-left panel of Figure 3.5 shows the summed intensities in head and tail boxes. The bottom-middle panel of Figure 3.5 shows the image RMS. The bottom-right panel of Figure 3.5 shows the result of DSNRS, that all of the signal found at the randomly selected location is due to direct reception of FM signals by the MWA.

However, the top three panels of Figure 3.5 shows the same observation, but with the top-left panel showing the summed intensities in head and tail boxes selected to correspond to a known satellite. The top-right panel of Figure 3.5 shows the result of DSNRS, that the FM signals reflected from the satellite are isolated. Thus, using DSNRS, we can determine the time and frequency dependence of the reflected FM signals, distinguished from direct reception FM signals.

The method also proved effective in revealing the reflections, even in frequency channels that contained satellite reflections as well as direct FM reception in them. This was tested by superimposing a difference image corrupted by direct FM reception (such as the one shown in Figure 3.3) over the difference image obtained in every other frequency channel. The FM reflection of the RFI was revealed even in the presence of increased noise, but the amplitude was attenuated. The DSNRS method was automated for the detection of reflections from all the frequency channels and time-steps for a given satellite by creating boxes at the predicted

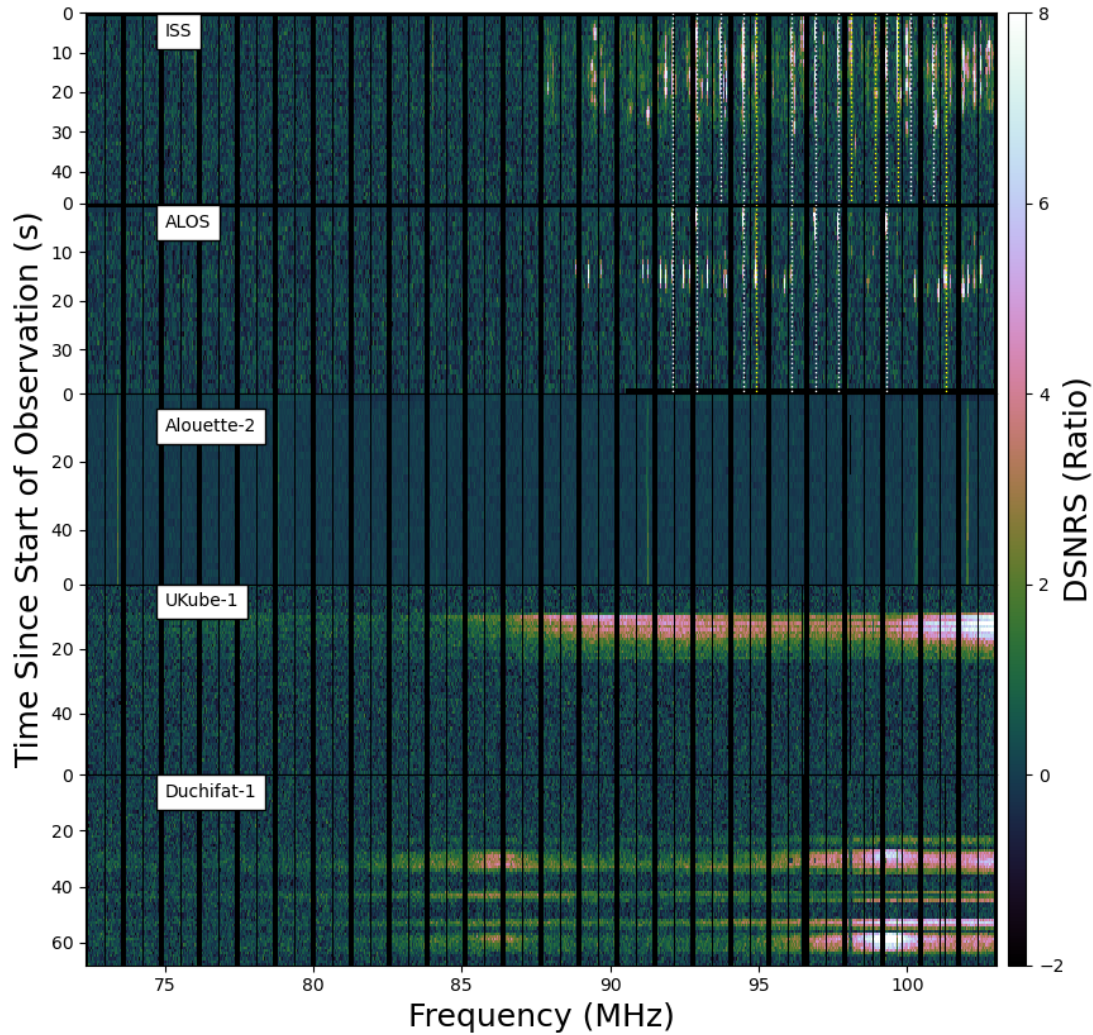


Figure 3.6: DSNRS plots of all the targeted objects mentioned in Table 3.1. The edge and middle of every course channel was flagged (represented by black lines) while the other vertical and horizontal flags are due to missing visibilities. The horizontal flags are due to hardware failure and the vertical flagging in every edge and middle of every course channel is performed to mitigate the impact of non-linear filter-bank response in those fine frequency channels. The top two panels have dotted white and yellow lines showing the fine channels reflecting FM transmitters from Perth and Geraldton, respectively. Note that the maximum values of the DSNRS plots for the CubeSats are much greater than 8 but the colorbar has been clipped between -2 and 8 in order to accommodate reflecting and transmitting satellites in the same figure.

locations of the satellite, as shown in Figure 3.2. The results of the DSNRS analysis are given in Section 3.4.1.

## 3.4 Results

### 3.4.1 Results of DSNRS Analysis for Targeted Objects

The DSNRSs for the objects listed in Table 3.1 are shown in Figure 3.6. From these figures, it can be seen that many transmitted signals from different locations are reflected by ALOS and the ISS. The ISS also has a reflection at 87.8 MHz which must be from a FM transmitter outside of Australia, given it is outside the allocated frequency range for FM broadcasts in Australia. It can be also noted that the ISS and ALOS have many common frequencies, presumably because they are quite similar in altitudes (thus having similar reflection geometries between transmitter, object, and receiver). The brightening and fading of the signal is likely due to the changing transmitter-object-receiver geometry and/or Radar Cross Section (RCS) as the object moves across the sky.

On the other hand, Alouette-2, whose altitude varies from 500 – 2700 km, was detected at a maximum line of sight distance of 2298 km and reflects signals from transmitters very distant (Loxton, Mildura, and Melbourne) from the MWA. The reflected signals for Alouette-2 are quite stable with time (unlike that of ISS and ALOS), perhaps due to it having a much slower angular speed across the sky due to its higher altitude (this is why 4 s time steps were used for Alouette-2, rather than 2 s time steps). Also the RCS of Alouette-2 may not change much relative to the transmitter/receiver geometry, due to it being almost spherical in shape (a perfect test particle for radar studies!). Alouette-2 appears to have a frequency reflected at approximately 73.4 MHz, again outside the FM broadcast band in Australia. This frequency overlaps with the VHF-low analog TV broadcast band, but these broadcasts have a much broader bandwidth than seen in the Alouette-2 DSNRS. Thus, the transmitter responsible for this reflection is unidentified.

When the frequency channel for imaging was selected appropriately, these satellites appeared in standard images even without making difference images or performing CLEAN. The fine channels that appeared the brightest in the DSNRS

plots in Figure 3.6 were chosen to make these images. The ISS and satellites as distant as Alouette-2 appeared well above the side-lobe confusion noise in these channels (about 12 Jy), as shown in Figure 3.7 and Figure 3.8, respectively.

BANE (part of AegeanTools) (Hancock et al., 2012, 2018) was used to perform background noise estimation and the calculation of flux densities (integrated intensities) from these images. The Effective Isotropic Radiated Power (EIRP) power calculated for Alouette-2 was found to be about  $11 \mu\text{W}$  (at a range of 2241 km), which is significantly higher than the power predicted (about 20 pW) for a 1 m diameter sphere using an XFDTD simulation in Tingay et al. (2013b). This could be due to the presence of antennas on the satellite making it a good reflector (due to increased RCS) or due to the satellite reflecting FM stations other than those considered in the simulation. Note that Alouette-2 is a defunct satellite and the higher EIRP could not be due to transmissions.

Two of the detected satellites are CubeSats (Duchifat-1 and UKube-1) and they appeared far brighter than large satellites such as the ISS and ALOS. Via the DSNRS analysis, these CubeSats were found to be most likely transmitting in the FM band, rather than reflecting terrestrial broadcast signals. This is evidenced in Figure 3.6 by the broadband nature of the signals from the CubeSats and the lack of identifiable narrow band FM signals associated with FM reflections. Amateur satellites are allowed to transmit between 144 – 146 MHz for down-link telemetry purposes but it appears that these CubeSats are producing significant transmitted power outside this allocated telemetry band. The measured EIRP from these CubeSats is approximately 256 mW. Note that EIRP is calculated assuming the transmission is isotropic. If the CubeSat transmission is directional in nature, then the actual transmitted power would be lower than indicated by the EIRP calculation. Also, since the CubeSats are smaller than the wavelength considered here, the out-of-band transmission could be due to failed or defective hardware.



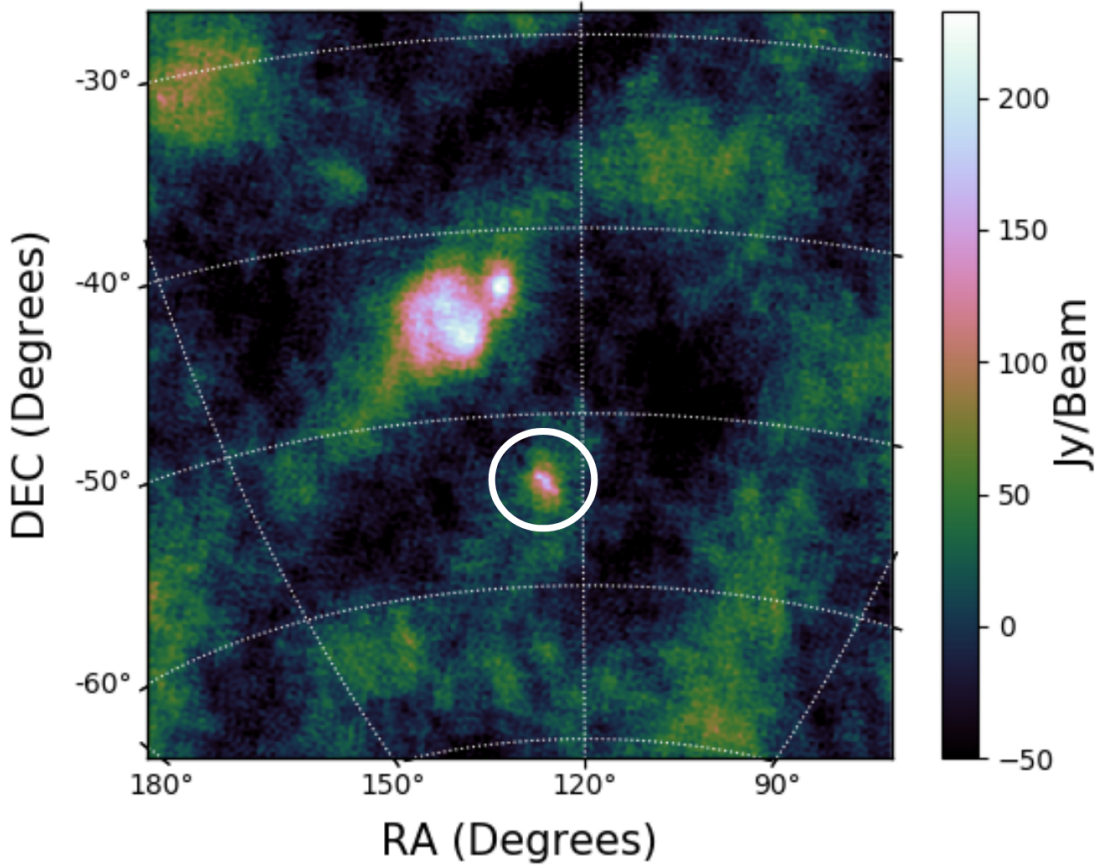


Figure 3.7: The bright spot inside the white circle is the ISS as seen in a single 40 kHz fine channel dirty image. The diffuse structure in the image is the Vela supernova remnant.

### 3.4.2 Detection of Additional Signals

In the process of examining the difference images for the targeted objects, at the high time and frequency resolution required to calculate the DSNRS, we noted that our data contained additional, generally short duration, signals. A significant number of these signals were detected, with a range of characteristics. The examination of the details of these short duration signals is beyond the scope of this current publication but we show an example here and will present a detailed study of these additional signals in a future publication.

Figure 3.9 shows a difference image in which a signal appears for only one difference time-step (4s). The lack of a negative tail confines the event to being

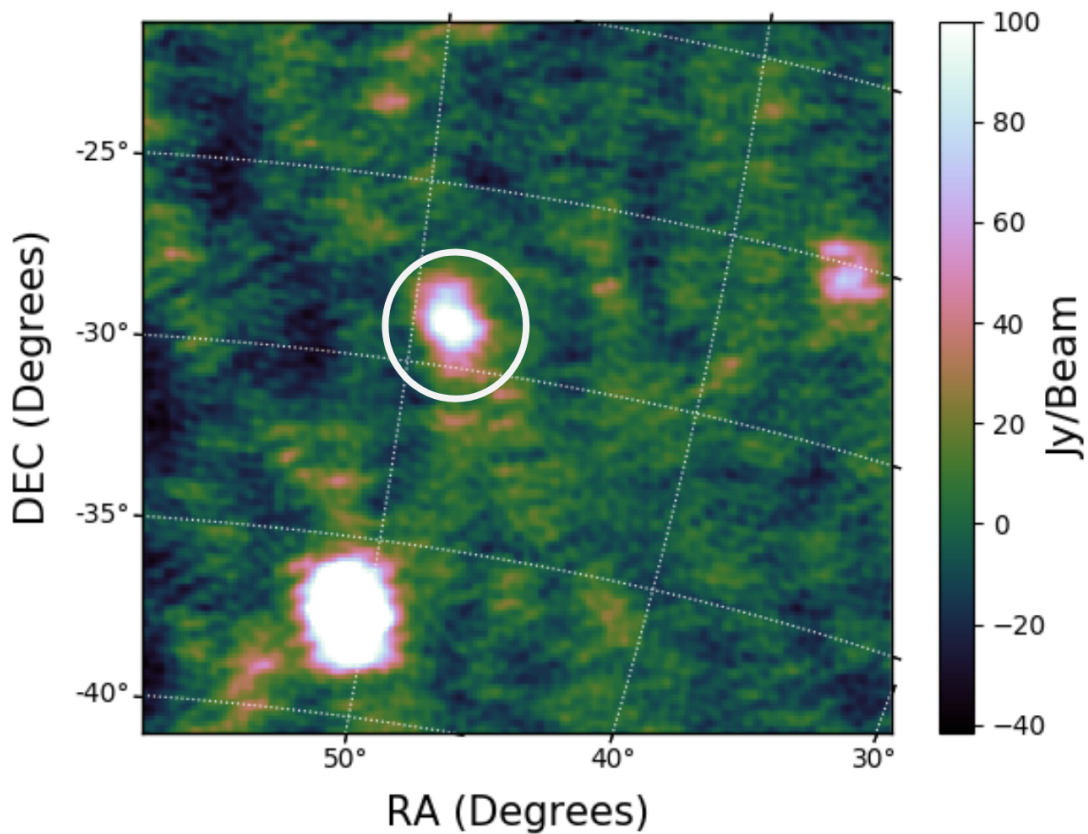


Figure 3.8: Alouette-2 as seen in a single 40 kHz fine channel dirty image. The source in the bottom left is Fornax-A and the bright spot in the right is a cluster of different sources seen as a single emission region due to using baselines shorter than 500 m.

shorter than 4 s. The detection is significant and the DSNRS shows that it is due to reflected FM signals (Figure 3.10). However, Figure 3.9 also shows that the signal does not correspond with the position of any catalogued satellite.

Most likely this signal is due to a reflection from a meteor trail, but other reasons for a short duration signal may be a highly variable RCS, due to a rapidly tumbling object or a geometrically complicated object.

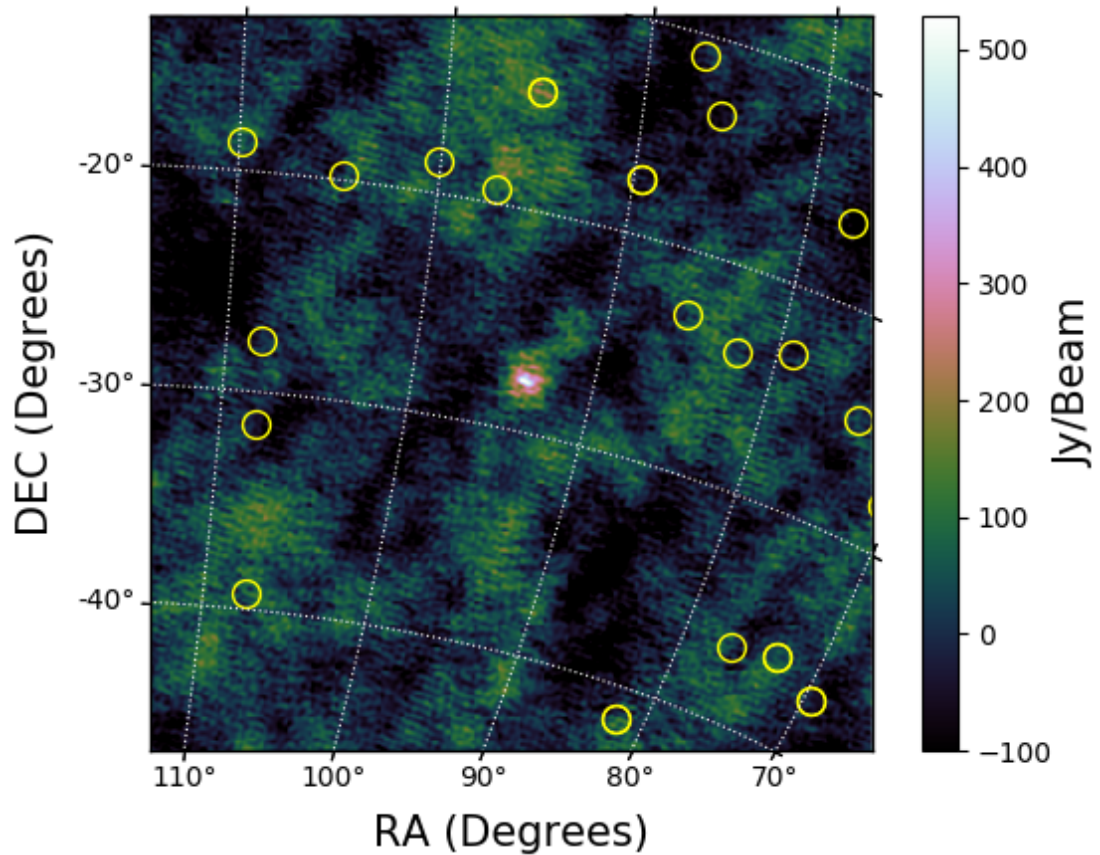


Figure 3.9: An object not in the TLE catalog. The yellow circles are the location of cataloged orbiting objects at that epoch. Note that the object does not appear as a streak due to the signal being confined within the 4s used in the difference image. This could also be a random burst of satellite transmission as previously observed by [Lenc et al. \(2018\)](#).

## 3.5 Discussion

### 3.5.1 Completeness

In this work, we perform a basic demonstration of the techniques involved for performing space surveillance with the MWA and in future we will develop it into a more sensitive blind detection pipeline. Also, due to having just 5 positive detections in the observations used in this work, we only perform a basic completeness check as mentioned below.

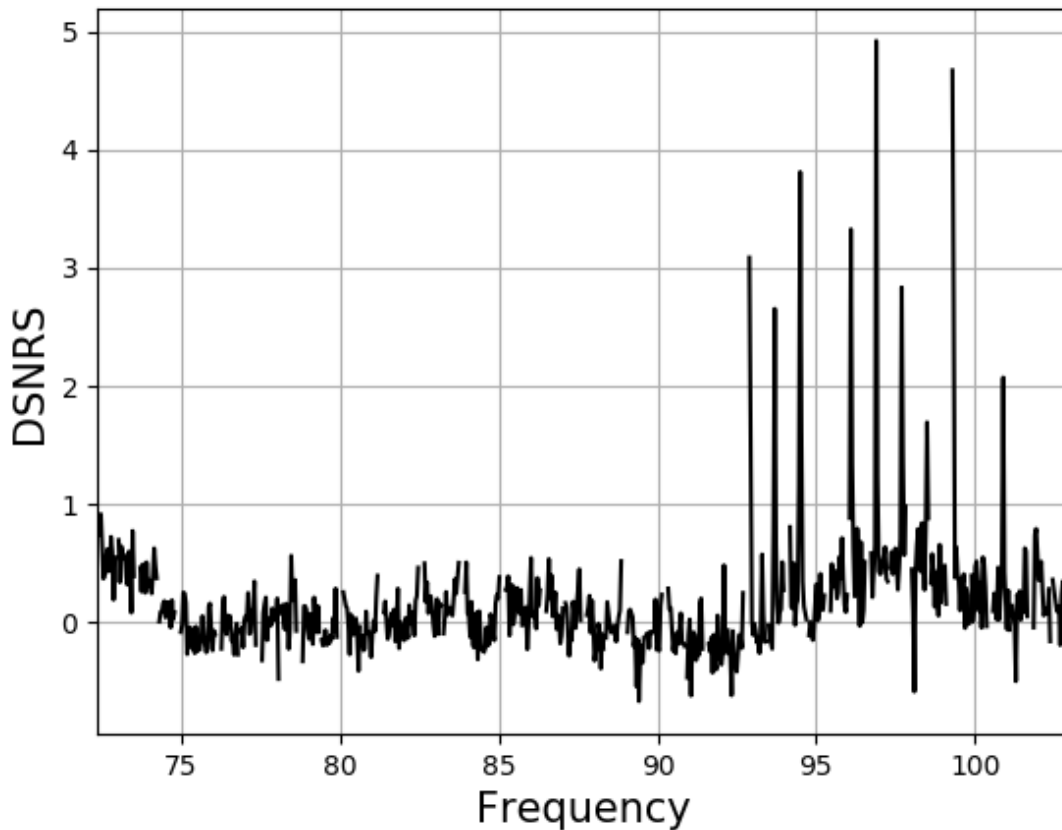


Figure 3.10: A single time-step DSNRS plotted for the short duration signal seen in Figure 3.9.

Tingay et al. (2013b) predicts that debris of radius  $0.5\text{ m}$  should be detected with the MWA Phase 1 configuration up to a range of  $1000\text{ km}$ , for a  $50\text{ kHz}$  bandwidth and one second integration. Hence, in order to do a basic check of detection completeness, the TLE catalog was used to identify all the objects in LEO, Medium Earth Orbit (MEO) and Highly Elliptical Orbit (HEO) that passed through MWA's half power beam and had their shortest range during pass to be less than  $8000\text{ km}$ . The shortest range for these satellites during the pass along with their RCS is plotted in Figure 3.11 (note that the website used for obtaining RCS values does not mention the frequency used for estimating the RCS and are an order of magnitude guide only. The RCS at the lower MWA frequencies is likely to be smaller). In the top-right region are all the satellites with RCS

$> 0.79 \text{ m}^2$  (2D projection of a sphere of radius 0.5 m), in bottom two regions are all the satellites with shortest range less than 1000 km and the bottom-right region is the predicted detection parameter-space (as per [Tingay et al. \(2013b\)](#)).

During the 19.34 minutes of observation a total of 49 unique objects with shortest range less than 1000 km passed through the half power beam with 3-6 objects being present in the field of view at any given instant. From [Figure 3.11](#), it can be noted that there are six objects that satisfy the detection criteria. These objects were identified to be ALOS, Iridium-65, and four different upper stage rocket debris (the RCS of the six objects are given in [Table 3.2](#)). But of the six objects only ALOS (the biggest) was detected in the full bandwidth difference images (note that ISS was detected outside the half power beam due to its very large RCS and hence is not part of the objects in [Figure 3.11](#)). Three of the four rocket bodies are in the observation containing the transmitting satellites and were within the field of view when these CubeSats were found to be transmitting. Hence, it is possible that these objects went undetected due to the increased noise caused by the side-lobes of the bright transmitting CubeSats (for example, the RMS of the 30.72 MHz difference images increased from 0.8 Jy to about 6.4 Jy when the CubeSats were visible). Other missed detections could be also due to unfavourable reflection geometries or weak reflections confining the signal to very few frequency channels, thus reducing the signal to noise ratio in the 30.72 MHz bandwidth images. Alouette-2 on the other hand was detected outside the predicted detection parameter space, possibly due to the existence of two dipole antennas of lengths 22.8 m and 73 m on the satellite (thus increasing its RCS in radio frequencies) for ionosphere sounding purposes<sup>8</sup>.

The [Tingay et al. \(2013b\)](#) simulations assumed a 50 kHz bandwidth and a 1 second integration, rather than the full bandwidth 30.72 MHz noted above, which combines a lot of frequency channels with no signal and dilutes the narrow band signal, reducing sensitivity. Also, the simulations assume detection in the

---

<sup>8</sup><https://nssdc.gsfc.nasa.gov/nmc/spacecraft/display.action?id=1965-098A>

maximum sensitivity pointing direction, whereas all the objects in Figure 3.11 lie away from this direction to various degrees. Thus, all of these effects plausibly explain why we detect only a subset of these objects. The minimum angular distance from the pointing center for the 5 undetected objects and the detected satellites is given in Table 3.2.

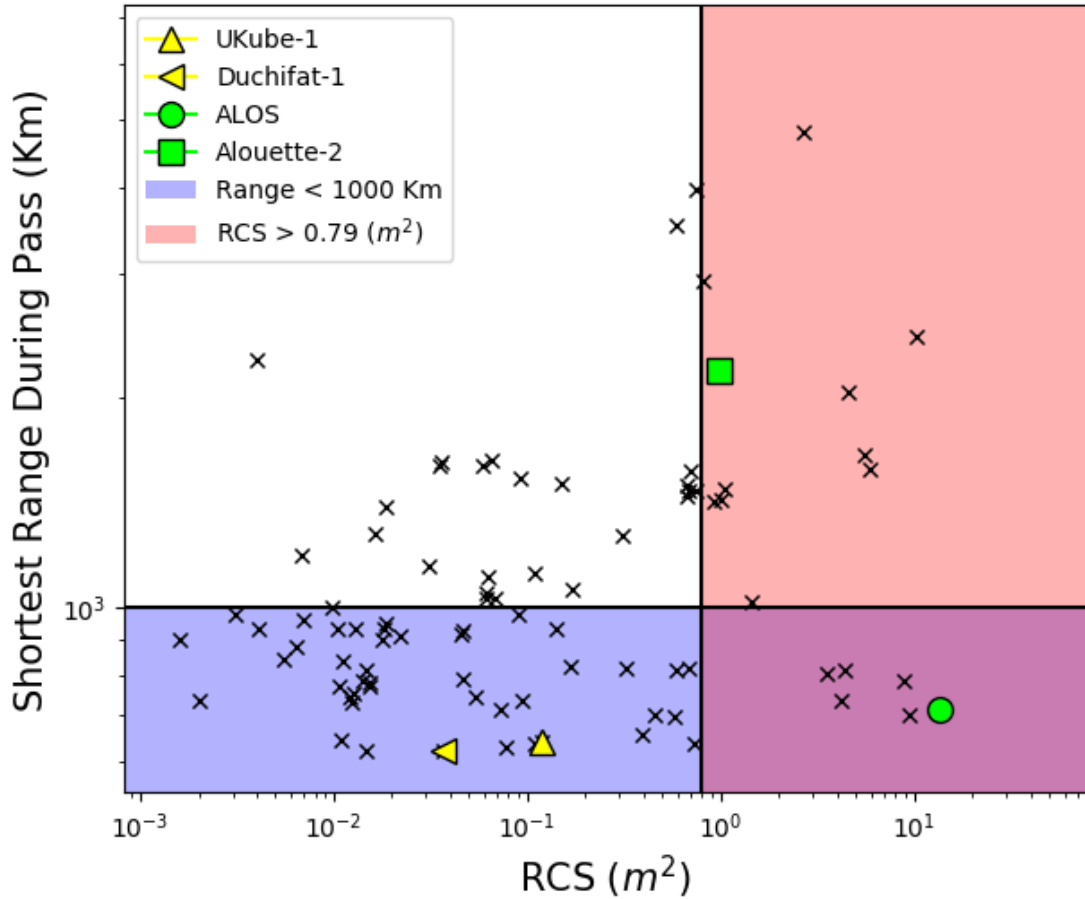


Figure 3.11: Satellites/debris that passed through the half power beam during the observations mentioned in Table 3.1. The transmitting satellites are shown in yellow and the reflecting satellites are shown in green. The bottom-right region is the detection parameter space for MWA in FM frequencies. Note that ISS is not part of the above figure, due to it being detected outside the half power beam.

Upon detailed inspection of difference images made for fine channels that overlap with known FM frequencies, a transient signal (such as the one shown in Figure 3.9) was found near the predicted location of Iridium-65 and was found to

Table 3.2: The Boresight angle (denoted as  $\theta$ ) of the 5 undetected objects along with the detected satellites (marked with asterisk) from the pointing center. It also gives the minimum range to target and the RCS for each of the considered objects.

Object	$\theta$ (Degrees)	Range (km)	RCS (m <sup>2</sup> )
IRIDIUM-65	11.4	802	3.6
DELTA 1 R/B	12.4	783	8.9
DELTA 2 R/B	16.2	701	9.5
SL-8 R/B(1)	16.1	735	4.2
SL-8 R/B(2)	18.4	811	4.4
Alouette-2*	12.5	2191	1.0
ALOS*	9.7	715	13.6
UKube-1*	14.4	644	0.1
ISS*	26.2	437	399.2
Duchifat-1*	12.6	624	0.03

be reflecting in FM frequencies using the DSNRS analysis. The signal was found to spatially coincide within the 1 km position TLE uncertainty of the object (about 0.3 degrees for Iridium-65). But due to the event being confined to a single time-step, the signal could not be definitively identified to be Iridium-65 by comparing its trajectory with the predicted trajectory of the satellite.

### 3.5.2 Future work

The DSNRS technique developed here helps classify signals based on their reflection/transmission spectra and the results we obtain support the idea of using the MWA for space surveillance due to its wide-field view. The TLE time offset mentioned in Table 3.1 can be used as a proxy to identify objects with outdated TLEs. Given that many satellites transmit at about 145 MHz, observing in these frequencies can help expand our detection window to also include transmitting CubeSats as well. In the future, blind detection of satellites can also be done with higher sensitivity using the compact configuration of Phase 2 of the MWA (Wayth et al., 2018). The compact configuration has two dense cores with most of the baselines being shorter than 200 m, thus being ideal for performing near-field

detections.

Future observations and data processing are planned in order to systematically assess the sensitivity of the techniques developed in this paper. For example, the MWA Voltage Capture System (VCS) (Tremblay et al., 2015) was recently used to perform data collection during the so-called SpaceFest2 event <sup>9</sup>, coordinated by the Australian Department of Defence in order to evaluate different technologies and sensor types for SDA . These observations were designed for coherent passive radar with the MWA, utilising processing as described by Hennessy et al. (2019, in press). However, we have used an offline correlation system for the MWA to convert the captured voltages into visibility datasets suitable for the non-coherent techniques developed in this paper. Thus, from the SpaceFest2 observations, we will be able to compare and test the limits of both coherent and non-coherent techniques with the MWA, from targeted observations (as opposed to the serendipitous observations used in this paper) over a range of objects with different RCS values.

### 3.6 Summary

In this paper we have:

- undertaken a detailed analysis of the apparent FM reflections from LEO RFI detected in Zhang et al. (2018);
- developed an analysis using a quantity we call the Dynamic Signal to Noise Ratio Spectrum (DSNRS), that helps classify signals as originating from objects in orbit from terrestrial transmitters;
- used the DSNRS to analyse three signals found to be FM reflections from objects in orbit (up-to a maximum range of 2298 km) and signals identified as out-of-band transmissions from two CubeSats;

---

<sup>9</sup><https://www.airforce.gov.au/our-mission/spacefest-edge>



- detected short duration signals at FM frequencies that do not coincide with satellite locations predicted using the TLE catalog;
- identified position offset between the actual and predicted TLE position, thus demonstrating MWA's potential to be used for catalog maintenance;
- performed a study completeness analysis, considering the reasons why some satellites in the field-of-view went undetected during the observations used in this work.



# Chapter 4

## A Low Earth Orbit Blind Survey using the MWA

This chapter is a reproduction of Prabu, S. Hancock, P. Zhang, X. Tingay, S.J, “A low-frequency blind survey of the low Earth orbit environment using non-coherent passive radar with the Murchison Widefield Array”, Publications of the Astronomical Society of Australia , Volume 37 , 2020 , e052, DOI: <https://doi.org/10.1017/pasa.2020.40>. It differs from the original in minor text edits to ensure consistency within this thesis. The reader will encounter some repetition of material in the introductory sections. This chapter builds upon the previous work by developing a blind detection pipeline that performs un-cued detections of transient narrow-band events in MWA FM band observations.

### 4.1 Abstract

We have extended our previous work to use the Murchison Widefield Array (MWA) as a non-coherent passive radar system in the FM frequency band, using terrestrial FM transmitters to illuminate objects in Low Earth Orbit (LEO) and the MWA as the sensitive receiving element for the radar return. We have implemented a blind detection algorithm that searches for these reflected signals in

difference images constructed using standard interferometric imaging techniques. From a large-scale survey using 20 hours of archived MWA observations, we detect 74 unique objects over multiple passes, demonstrating the MWA to be a valuable addition to the global Space Domain Awareness network. We detected objects with line-of-sight distance up to 977 km and as small as  $0.03 m^2$  radar cross section. We found that 30 objects were either non-operational satellites or upper-stage rocket body debris. Additionally, we also detected FM reflections from Geminid meteors and aircraft flying over the MWA. Most of the detections of objects in LEO were found to lie within the parameter space predicted by previous feasibility studies, verifying the performance of the MWA for this application. We have also used our survey to characterise these reflected signals from LEO objects as a source of Radio Frequency Interference (RFI) that corrupts astronomical observations. This has allowed us to undertake an initial analysis of the impact of this RFI on the MWA and the future Square Kilometer Array (SKA). As part of this analysis, we show that the standard MWA RFI flagging strategy misses most of this RFI and that this should be a careful consideration for the SKA.

## 4.2 Introduction

With the advent of satellite mega-constellations, the density of objects in Low Earth Orbit (LEO) is predicted to reach 0.005 – 0.01 objects per degree square (McDowell, 2020). Most of the current space surveillance radar systems dedicated to monitoring such objects in space (Space Domain Awareness: SDA<sup>1</sup>) operate at VHF/UHF/S-Band and utilise active transmitters to reflect signals from objects in the space environment (Goldstein et al., 1998). The predicted increase in the density of LEO objects demands detection systems with large instantaneous Field-of-View (FOV) receivers, the ability to change pointing directions and tracking quickly, and wide field illuminators. We aim to address these issues

---

<sup>1</sup>Previously Space Situational Awareness (SSA)

by using the Murchison Widefield Array (MWA) as a sensitive passive receiver in the FM band, coupled with existing, uncoordinated FM transmitters as the illuminators.

Previously, [Prabu et al. \(2020b\)](#) demonstrated the so-called Dynamic Signal to Noise Ratio Spectrum (DSNRS) technique, detecting signals from satellites/debris, either via FM reflections or down-link transmissions, and differentiates them from other types of Radio Frequency Interference (RFI) entering the detection system (the MWA). This previous work utilized the results of [Zhang et al. \(2018\)](#) to select a small set of MWA observations known to contain signals reflected from satellites.

Having verified the DSNRS technique, we now take the next step in developing SDA capabilities using the MWA, by undertaking the first blind survey of LEO using the MWA. We have developed a semi-automated pipeline to perform uncued searches for the signals of interest from a large volume of data, 10s of millions of individual images of the entire sky visible from the MWA. This survey is representative of the capabilities of the MWA, should it be used in an on-going operational mode for SDA observations.

As well as realising a survey of LEO, the signals we recover from the MWA data also represent a corrupting influence on astronomical observations at low frequencies. Reflections off, or transmissions from, satellites represent moving sources of Radio Frequency Interference (RFI) that constantly occupy the sky above the MWA (and soon the Square Kilometre Array: SKA). Thus, we are able to quantify the impact this RFI is likely to have on the MWA and the future SKA. Using our survey, we investigate this impact and, in particular, the performance of standard RFI identification and mitigation strategies.

We briefly summarise previous work in [Section 4.3](#). We describe our data processing pipeline in [Section 4.4](#), and our results in [Section 4.5](#). The discussion and conclusions are in [Sections 4.6](#) and [4.7](#), respectively.

## 4.3 Background

Recently, many studies have raised concerns about the impacts of rapidly increasing LEO objects on astronomy (McDowell, 2020; Gallozzi et al., 2020; Hainaut & Williams, 2020; Mallama, 2020). We utilise this as an opportunity to demonstrate space surveillance capabilities using an existing radio interferometer and terrestrial FM transmitters.

The MWA is a low frequency radio interferometer built as a precursor to the Square Kilometre Array (SKA) (Tingay et al., 2013a). The MWA can observe the sky at 70 – 300 MHz and was primarily designed for radio astronomy purposes (Bowman et al., 2013; Beardsley et al., 2019). The MWA has detected satellites in the past using two different techniques; namely coherent detection (Palmer et al., 2017; Hennessy et al., 2019) and non-coherent detection (Tingay et al., 2013b; Zhang et al., 2018; Prabu et al., 2020b) methods.

The coherent detection method uses the MWA’s high time and frequency resolution Voltage Capture System (VCS) (Tremblay et al., 2015) and performs detections using matched filters designed using the transmitted FM signal (Hennessy et al., 2019), while the non-coherent detection system uses interferometer correlated data (Prabu et al., 2020b) along with wide-field imaging techniques. The blind detection pipeline developed here uses the non-coherent detection method, including the use of the DSNRS techniques established by Prabu et al. (2020b).

Electromagnetic simulations presented in Tingay et al. (2013b) predict that LEO objects with a radar cross section (RCS) greater than  $0.79 m^2$  and with line of sight (LOS) range less than 1000 km can be detected using the MWA in the FM band using non-coherent techniques, and we compare our obtained results with these predictions in Section 4.6.

## 4.4 Data Processing

In this work, we aimed to autonomously<sup>2</sup> search for signals from satellites in the MWA data using non-coherent techniques. We utilised observations that observed the sky in the frequency range 72.335 – 103.015 MHz, as this band partially overlapped with FM frequencies and a large number of observations in this band were readily available in the MWA archive. The 628 observations (Table 4.1) used in this work were zenith pointing drift scans from four different nights performed using the MWA’s phase 2 compact configuration (Wayth et al., 2018). The compact configuration has most of its baselines shorter than 200 m, thus enabling the detection system to be sensitive towards near-field objects at FM frequencies.

The visibility files for these observations were downloaded from the All-Sky Virtual Observatory<sup>3</sup> (ASVO) node for the MWA. They were converted to measurement sets (McMullin et al., 2007) using COTTER (Offringa et al., 2015) with a time averaging of 2 s and a frequency resolution of 40 kHz with RFI flagging disabled.

Calibration observations were obtained as measurement sets from ASVO and were preprocessed with AOFLAGGER (Offringa et al., 2015) to flag all baselines with RFI. This was followed by calibration of the measurement sets using the calibrator model. Once calibrated, in order to obtain calibration solutions for channels with RFI, we interpolate solutions between neighbouring channels.

After applying the interpolated calibration solutions to the target observations, the whole sky were imaged at every time-step and fine frequency channel using WSCLEAN (Offringa et al., 2014; Offringa & Smirnov, 2017). WSCLEAN is the abbreviation for W-Stack CLEANing, an advanced de-convolution method developed for wide-field interferometers. CLEAN (de-convolution) is usually done in order to reduce the side-lobes of the synthesised beam. However, we do not

---

<sup>2</sup>The data reduction pipeline is available at <https://github.com/StevePrabu/MWASSA-Pipeline>

<sup>3</sup><https://asvo.mwatelescope.org/dashboard>

perform CLEAN as the subsequent step in our pipeline was to generate difference images, which remove the static celestial sources along with their side-lobes, revealing signals from objects such as satellites, meteors, and aircraft.



Table 4.1: List of observations and calibration observations used in this work. Observation IDs can be searched within the MWA ASVO.

Observation IDs	Start UTC	End UTC	Total Duration (hours)	Calibration Observation	Calibrator Source
1157366872 - 1157407072	2016-09-08 10:47:34	2016-09-08 21:57:34	1.93	1157381872	3C444
1157453032 - 1157493232	2016-09-09 10:43:34	2016-09-09 21:53:34	1.87	1157452432	Her A
1160477632 - 1160507152	2016-10-14 10:53:34	2016-10-14 19:05:34	7.34	1160507272	Pic A
1165749976 - 1165782976	2016-12-14 11:25:58	2016-12-14 20:35:58	8.4	1165779136	Hyd A

### 4.4.1 Blind Search

After the images at every time-step and frequency channels were generated, a blind detection pipeline<sup>4</sup> was run. The pipeline constructed difference images by subtracting the image at time-step  $t$  from time-step  $t + 1$ , for every fine frequency channel, and searched for pixels over  $6\sigma$ . The  $6\sigma$  pixels were used to seed a detection, and we use a flood-fill<sup>5</sup> function to identify all adjacent pixels above  $3\sigma$ . An example of a satellite detected using this method is shown in Figure 4.1. The pixels together constitute the detected signal. We limit our algorithm to the detection of one event (the brightest) per time step per frequency, as when strong signals are present they are accompanied by many strong side-lobes (since performing CLEAN on all the images was not computationally feasible), which we do not want to record as detections. Note that multiple detections at a single time-step are possible if they are seen in different frequency channels. Information for each detection, such as its coordinates (Right Ascension and Declination), peak flux density, time stamp, and frequency were stored for later analysis.

### 4.4.2 Detection Maps

For each of the target observations, the positions of the detections were combined to make detection maps as shown in Figure 4.2. These detection maps are a visualisation tool to perform matching (by eye) of the detections in the observation with the predicted orbits of satellites in the FOV. In Figure 4.2 the detections are shown in black. The predicted trajectories<sup>6</sup> for all the objects in LEO, Medium Earth Orbit (MEO), and Highly Elliptical Orbits (HEO) above the horizon are plotted in red and green. Tingay et al. (2013b) predicts that the objects with range less than 1000 km and an RCS greater than  $0.785 m^2$  can be detected by the MWA. Hence, if the object is within the MWA's half power

---

<sup>4</sup><https://github.com/StevePrabu/RFISeeker>

<sup>5</sup>An algorithm that finds all adjacent cells that satisfy a given condition. We used the "forest fire algorithm" (Torbert, 2016).

<sup>6</sup>Using TLE obtained from <https://www.space-track.org>

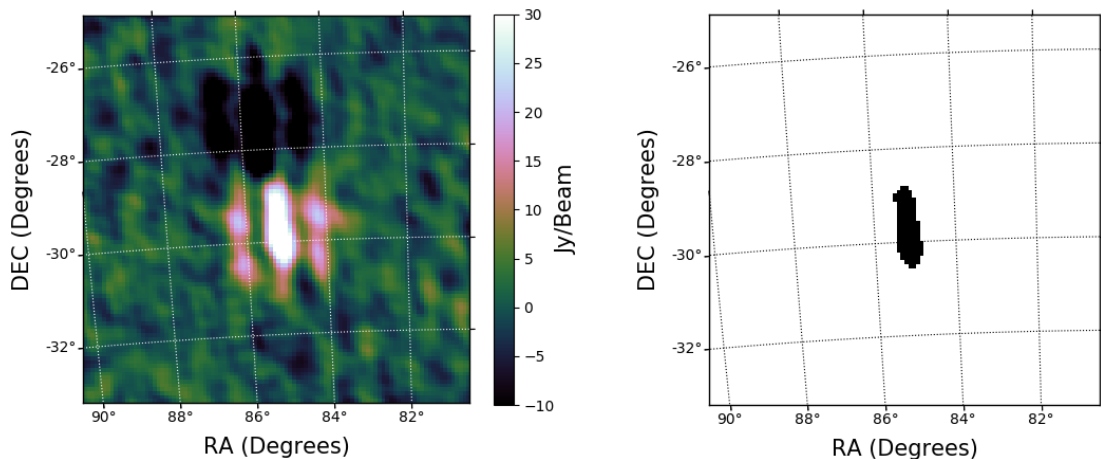


Figure 4.1: The left panel shows a primary beam corrected 40 kHz fine channel difference image of KANOPUS-V. KANOPUS-V is an Earth observation mini satellite orbiting at an altitude of 510 km. The image shows two adjacent streaks caused by side-lobes. The right panel shows the floodfill region of the detected signal.

beam<sup>7</sup> and satisfies the above mentioned conditions, then the red trajectory is replaced by green (as these are theoretically detectable orbits). The detections that were seen in multiple frequencies (in order to reduce the false positive events as described in Section 4.5.5) can be classified as satellites, meteor candidates, aircraft, terrestrial transmitters, unknown objects, and false detections, and are discussed in Section 4.5.

### 4.4.3 Parallax Analysis

The detections classified as aircraft (Section 4.5.3) appeared bright enough to be detected outside the MWA’s primary beam and we estimate the range to these aircraft by performing parallax measurements. The MWA has 128 tiles, and splitting the array into two sub-arrays enables us to perform parallax measurements to some of these bright nearby events that are within the atmosphere. At FM frequencies, the parallax baseline used in this work was sensitive towards

---

<sup>7</sup>for FM band zenith pointed MWA observations, the grating lobes do not appear above the horizon. However, events such as air-crafts and FM reflections fro large objects such as the ISS often can appear even in the null of the primary beam.

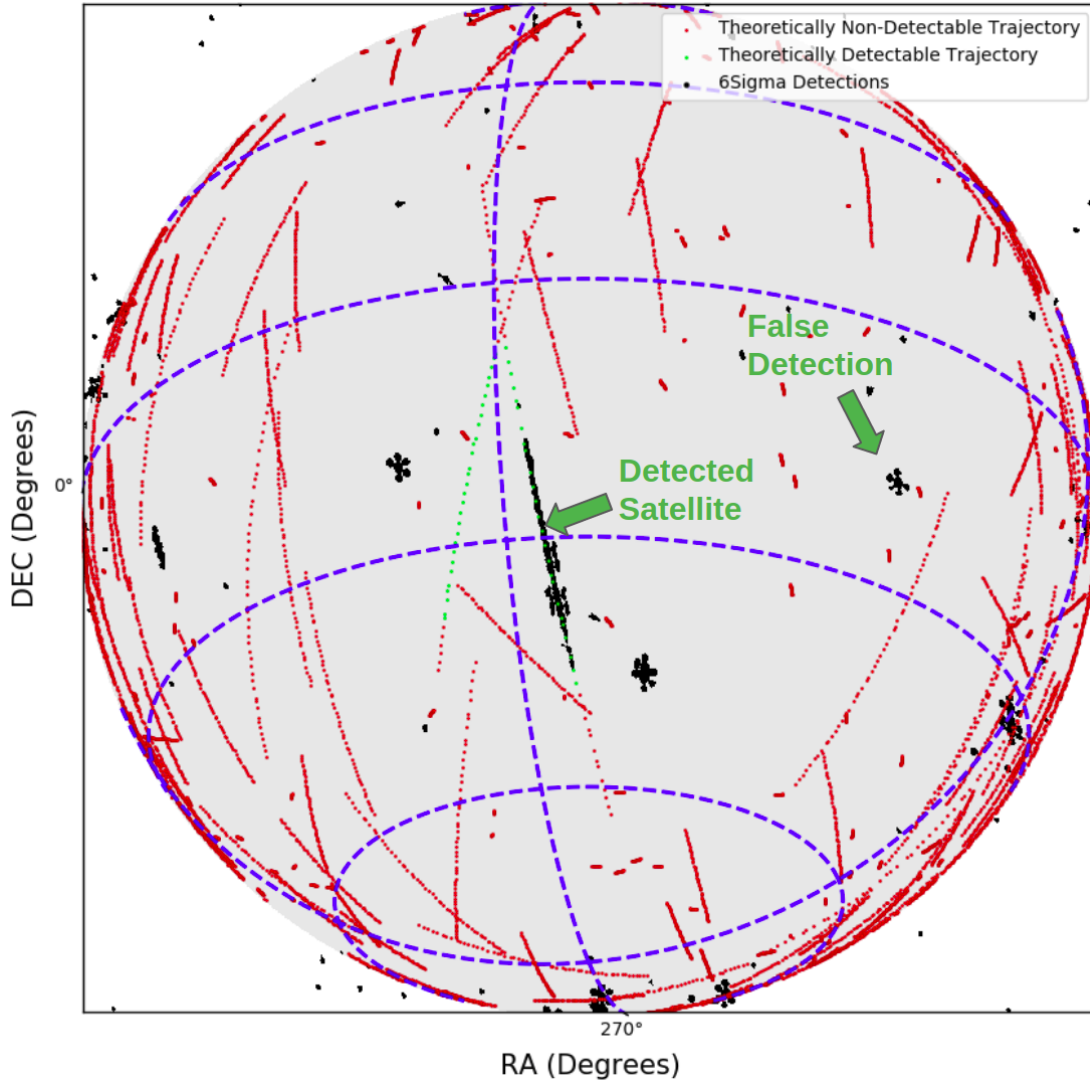


Figure 4.2: The visible horizon during one of the 112s MWA observations. The black markers are detections during this observation. The predicted orbits of all satellites within the visible horizon are plotted in red (or green). If the satellite orbit satisfies all predicted detection criteria (as predicted by [Tingay et al. \(2013b\)](#)) and is within MWA’s half power beam, then its trajectory is plotted in green. One of the theoretically detectable satellites being detected by the pipeline is shown and one is not detected. There are several transmitters also detected near the horizon. The figure also shows one of the false detections that takes the shape of the point spread function.

objects within an approx 100 km altitude (near the zenith).

The MWA compact configuration baselines were sorted in longitude, using the geometric centres of the baselines. Using this sorted list of baselines, the

1000 east-most baselines were combined to make an eastern aperture (ensemble of points in the UV plane) and the 1000 west-most baselines were combined to make a western aperture. The measurement sets for the eastern and western apertures were created by using the `split`<sup>8</sup> task in Common Astronomy Software Applications (CASA<sup>9</sup>) by providing the baseline configuration for both the apertures.

Difference images for the full MWA compact array, eastern aperture, and western aperture were produced for one of the time-steps in which an aircraft was present. However, the UV coverages of the three apertures are different, resulting in different beams sizes. Hence, we address the problem by performing CLEAN and using a low resolution restoring beam corresponding to the lowest resolution of the three apertures. Due to the reflection signal being present in many frequency channels, we enabled the multi-frequency synthesis feature of WSCLEAN while imaging. The centres of the eastern and western apertures were calculated using the geocentric coordinates of the tiles obtained from the measurement set using `casa-core`<sup>10</sup>. The two apertures result in a parallax baseline of 228.2 m.

The difference images made using the eastern and western apertures showed the parallax shift in the apparent position of the aircraft, as shown in Figure 4.3. Using the maximum brightness points and the centres of the two apertures, the LOS range to the aircraft was calculated as in Earl (2015) to be  $20 \pm 2$  km. The aircraft was detected at an azimuth of  $82.6^\circ$  and an elevation of  $26.3^\circ$ , placing it at an altitude of  $9 \pm 1$  km (height of most civil aircraft). Note that although the baselines were sorted in longitude to maximise the East-West separation, the centres of the two apertures have a latitude component as well, thus in Figure 4.3 we see a combination of East-West and North-South offsets in the apparent position.

---

<sup>8</sup><https://casa.nrao.edu/docs/TaskRef/split-task.html>

<sup>9</sup><https://casa.nrao.edu/>

<sup>10</sup><https://casacore.github.io/python-casacore/>

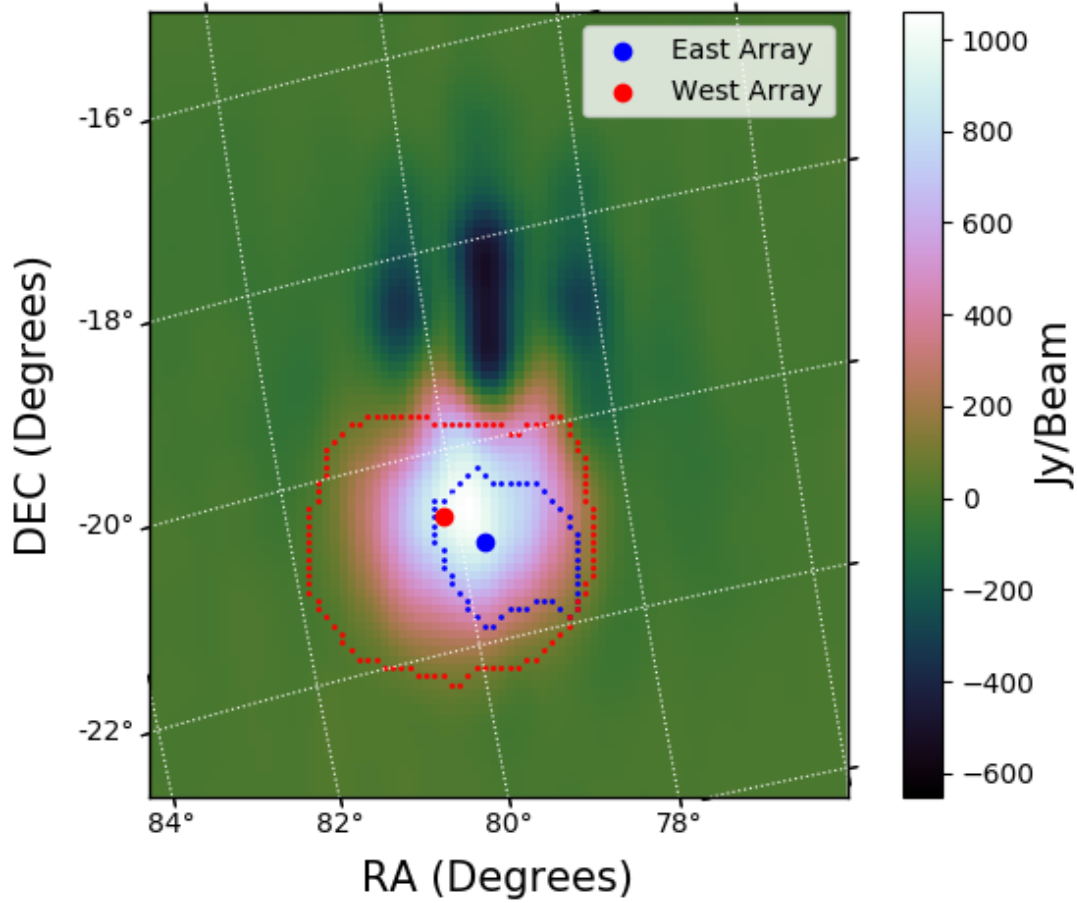


Figure 4.3: 30.72 MHz bandwidth difference image of an aircraft using the MWA compact array. The blue and the red dotted lines are  $3\sigma$  contours of the streak when seen by the eastern and western apertures, respectively. The dots are the corresponding points of maximum brightness. Note that the contour of the eastern aperture image is smaller than that for the western aperture, due to the two sub-arrays having different sensitivities (number of short baselines) towards the aircraft’s altitude.

## 4.5 Results

### 4.5.1 Satellite Candidates

Visual inspection of the detection maps for each of the observations was performed, and the events that plausibly matched in time and position with known objects at multiple time-steps were classified as satellite candidate detections. A total of 74 unique LEO objects were detected over multiple passes, of which 15

were upper stage rocket body debris. The LOS ranges for these satellites were obtained for the time-steps they were detected (calculated using the Two Line Element (TLE) values). The range values, along with RCS, peak flux densities, and operational statuses for these detected objects are tabulated in Table 4.2 (the UTC time, frequency and angular location of all the detected events for the observations mentioned in Table 4.2 are available in Prabu et al. (2020c)). An example DSNRS plot, illustrating the range of frequencies and times for which a satellite was detected is shown in Figure 4.4.

Two satellites, the CubeSats DUCHIFAT-1 and UKUBE-1, were detected due to out-of band transmissions in the FM band, rather than reflections (as previously observed by Zhang et al. (2018) and Prabu et al. (2020b)).

Table 4.2: Table lists the detected satellites/debris and their properties. Legend: O=Operational, R/B=Rocket Body, NO=Non-Operational, PO=Partially Operational, N/A=Not Available. The table summarises the properties of all the detected satellites. It provides the satellites North American Aerospace Defence (NORAD) ID, the range of distance over which it was detected, its Radar Cross Section (RCS<sup>13</sup>), the zenith angle ( $\theta$ ), and the primary beam corrected peak flux density as seen in the brightest 40 kHz frequency channel. Note that the operational status <sup>14</sup> may not be accurate as the information source does not list the date it was last updated. Note that the Observation ID is the GPS time of the start of the observation.

Observation ID	START UTC	NORAD ID	Satellite/Debris Name	Range km	RCS $m^2$	Operational Status	$\theta$ Degrees	Peak Flux Density (Jy/beam)
The detections below are from the night of 2016-12-14 from 11:25:58 UTC to 20:35:58 UTC								
1165782616	2016-12-14 20:29:59	33408	SJ-6E	598 - 603	1.3	O	5.0	32.5
1165782016	2016-12-14 20:19:59	28898	MOZHAYETS 5 and RUBIN-5	699 - 709	5.9	N/A	2.3	31.2
1165780696	2016-12-14 19:57:59	23088	SL-16 R/B	863 - 873	10.3	R/B	13.4	137.9
1165779376	2016-12-14 19:35:59	13367	LANDSAT 4	538 - 539	6.4	NO	6.3	35.3
1165777336	2016-12-14 19:01:59	28230	GP-B	669 - 687	10.2	NO	9.9	61.3
1165777216	2016-12-14 18:59:59	9786	DELTA 1 R/B(1)	621 - 624	8.9	R/B	6.5	55.4
1165776496	2016-12-14 18:47:59	40420	COSMOS 2503	587 - 600	5.5	O	3.1	33.6
1165773496	2016-12-14 17:57:59	40310	YAOGAN 24	639 - 656	4.2	O	3.3	115.8
1165773136	2016-12-14 17:51:59	24277	MIDORI (ADEOS)	806 - 816	22.2	NO	5.8	51.2
1165772296	2016-12-14 17:37:59	13153	COSMOS 1356	480 - 486	9.0	N/A	7.3	39.9
1165771216	2016-12-14 17:19:59	33492	GOSAT (IBUKI)	681 - 705	4.6	O	5.1	56.3
1165771096	2016-12-14 17:17:59	33053	FGRST (GLAST)	555 - 563	4.9	E	17.7	233.9
1165770136	2016-12-14 17:01:59	41336	BREEZE-KM R/B	534 - 540	3.3	R/B	20.0	38.2
1165768696	2016-12-14 16:37:59	20580	HST	617 - 669	28.1	O	25.2	449.5



Table 4.3: ...continued from previous page.

Observation ID	START UTC	NORAD ID	Satellite/Debris Name	Range <i>km</i>	RCS <i>m</i> <sup>2</sup>	Operational Status	$\theta$ Degrees	Peak Flux Density (Jy/beam)
1165767856	2016-12-14 16:23:59	25078	IRIDIUM 44	780 - 783	3.3	NO	6.2	44.5
1165766176	2016-12-14 15:55:59	38707	KANOPUS-V 1	518 - 543	1.9	O	5.7	81.9
1165765696	2016-12-14 15:47:59	41731	QSS (MOZI)	528 - 540	2.1	O	20.8	50.5
1165765336	2016-12-14 15:41:59	39152	TURKSAT-3USAT	632 - 642	0.1	NO	3.9	25.5
1165765216	2016-12-14 15:39:59	25544	ISS (ZARYA)	651 - 877	399.1	O	47.2	247,009
1165765096	2016-12-14 15:37:59	25544	ISS (ZARYA)	733 - 977	399.1	O	44.4	25,936
1165764136	2016-12-14 15:21:59	25758	IRS-P4 (OCEANSAT)	730 - 764	3.5	NO	0.9	44.8
1165764136	2016-12-14 15:21:59	28499	ARIANE 5 R/B	687 - 698	16.0	R/B	13.0	45.1
1165763056	2016-12-14 15:03:59	39019	PLEIADES 1B	719 - 729	5.4	O	8.2	26.7
1165762576	2016-12-14 14:55:59	20580	HST	578 - 600	28.1	O	19.9	120.6
1165761856	2016-12-14 14:43:59	41848	WORLDVIEW-4	626 - 634	6.6	PO	5.3	30.2
1165761736	2016-12-14 14:41:59	27601	H-2A R/B	844 - 879	24.6	R/B	5.9	34.8
1165761376	2016-12-14 14:35:59	41341	H-2A R/B	576 - 607	27.4	R/B	8.5	127.1
1165761256	2016-12-14 14:33:59	38046	ZIYUAN 3 (ZY 3)	528 - 561	5.3	O	13.7	139.3
1165761136	2016-12-14 14:31:59	38046	ZIYUAN 3 (ZY 3)	513 - 562	5.3	O	5.8	152.1
1165760896	2016-12-14 14:27:59	21422	COSMOS 2151	618 - 625	5.7	N/A	9.2	26.5
1165760776	2016-12-14 14:25:59	12987	COSMOS 1328	565 - 579	8.2	N/A	6.5	44.2
1165760536	2016-12-14 14:21:59	38249	PSLV R/B	381 - 407	5.8	R/B	1.4	55.0

Table 4.3: ...continued from previous page.

Observation ID	START UTC	NORAD ID	Satellite/Debris Name	Range <i>km</i>	RCS <i>m</i> <sup>2</sup>	Operational Status	$\theta$ Degrees	Peak Flux Density (Jy/beam)
1165758616	2016-12-14 13:49:59	29499	METOP-A	862 - 878	11.2	O	17.1	53.0
1165757056	2016-12-14 13:23:59	27386	ENVISAT	782 - 805	18.6	NO	8.0	117.6
1165756576	2016-12-14 13:15:59	20580	HST	565 - 584	28.1	O	13.4	59.0
1165756576	2016-12-14 13:15:59	29228	RESURS-DK 1	583 - 596	8.8	O	13.0	25.7
1165756456	2016-12-14 13:13:59	20580	HST	551 - 553	28.1	O	8.3	80.8
1165756096	2016-12-14 13:07:59	11060	TIROS N	849 - 853	4.1	PO	0.8	37.2
1165755976	2016-12-14 13:05:59	14819	COSMOS 1544	505 - 526	8.3	N/A	0.3	179.8
1165754896	2016-12-14 12:47:59	32062	CBERS 2B	773 - 784	2.5	NO	12.7	38.4
1165753936	2016-12-14 12:31:59	16881	COSMOS 1766	558 - 584	8.3	N/A	3.3	52.3
1165753936	2016-12-14 12:31:59	23968	ATLAS 2 CENTAUR R/B	472 - 528	14.9	R/B	5.2	242.6
1165752856	2016-12-14 12:13:59	16613	SPOT 1	691 - 702	7.3	NO	15.4	102.4
The detections below are from the night of 2016-10-14 from 10:53:34 UTC to 19:05:34 UTC								
1160505472	2016-10-14 18:37:35	38257	YAOGAN 14	493 - 505	5.41	O	7.5	143.0
1160504512	2016-10-14 18:21:35	10490	DELTA 1 R/B(1)	523 - 530	9.1	R/B	9.3	48.1

Table 4.3: ...continued from previous page.

Observation ID	START UTC	NORAD ID	Satellite/Debris Name	Range <i>km</i>	RCS <i>m</i> <sup>2</sup>	Operational Status	$\theta$ Degrees	Peak Flux Density (Jy/beam)
1160504752	2016-10-14 18:25:35	24796	IRIDIUM 4	805 - 815	3.7	NO	13.5	63.1
1160502952	2016-10-14 17:55:35	21574	ERS-1	790 - 794	10.3	NO	4.4	32.7
1160502472	2016-10-14 17:47:35	15427	NOAA 9	876 - 904	4.3	PO	13.4	61.8
1160500432	2016-10-14 17:13:35	28480	CZ-2C	841 - 843	10.0	R/B	13.4	38.2
1160498872	2016-10-14 16:47:35	36095	COSMOS 2455	914 - 917	12.2	O	2.9	41.8
1160497792	2016-10-14 16:29:35	24950	IRIDIUM 31	793 - 800	3.6	N/A	2.3	35.1
1160497672	2016-10-14 16:27:35	25544	ISS (ZARYA)	454 - 577	399.1	O	21.5	23,492
1160497672	2016-10-14 16:27:35	40074	UKUBE-1	739 - 760	0.1	O	31.3	417.1
1160497552	2016-10-14 16:25:35	25544	ISS (ZARYA)	442 - 587	399.1	O	17.9	19,138
1160497192	2016-10-14 16:19:35	19274	OKEAN-1	573 - 586	8.6	N/A	7.7	49.6
1160497072	2016-10-14 16:17:35	19274	OKEAN-1	564 - 575	8.6	N/A	4.0	40.2
1160497072	2016-10-14 16:17:35	41386	RESURS P3	520 - 546	7.7	O	18.5	160.2
1160496352	2016-10-14 16:05:35	39574	GPM-CORE	415 - 435	8.1	O	11.1	70.2
1160496232	2016-10-14 16:03:35	39574	GPM-CORE	410 - 479	8.1	O	7.0	598.1
1160495752	2016-10-14 15:55:35	23608	ARIANE 40+3 R	602 - 619	9.7	R/B	6.8	142.6
1160493592	2016-10-14 15:19:35	40118	GAOFEN 2	642 - 714	3.5	O	3.4	126.3

Table 4.3: ...continued from previous page.

Observation ID	START UTC	NORAD ID	Satellite/Debris Name	Range <i>km</i>	RCS <i>m</i> <sup>2</sup>	Operational Status	$\theta$ Degrees	Peak Flux Density (Jy/beam)
1160493472	2016-10-14 15:17:35	40021	DUCHIFAT-1	647 - 709	0.03	O	17.6	469.0
1160493472	2016-10-14 15:17:35	25260	SPOT 4	716 - 752	6.2	NO	0.5	109.4
1160492512	2016-10-14 15:01:35	28649	IRS-P5 (CARTOSAT-1)	654 - 668	4.7	O	15.4	105.6
1160492392	2016-10-14 14:59:35	28649	IRS-P5 (CARTOSAT-1)	640 - 647	4.7	O	10.2	44.9
1160491192	2016-10-14 14:39:35	20624	COSMOS 2082	864 - 888	10.8	N/A	11.1	146.4
1160490232	2016-10-14 14:23:35	23697	ATLAS 2 CENTAUR	919 - 929	13.9	R/B	2.5	76.0
1160489512	2016-10-14 14:11:35	812	OPS 4467 A	821 - 844	0.34	N/A	0.9	48.9
1160488792	2016-10-14 13:59:35	27421	SPOT 5	659 - 665	7.3	NO	9.4	130.6
1160487952	2016-10-14 13:45:35	41765	TIANGONG-2	446 - 455	15.8	N/A	28.4	232.9
1160487832	2016-10-14 13:43:35	23317	OKEAN-4	639 - 656	7.1	N/A	9.5	208.3
1160486632	2016-10-14 13:23:35	8845	METEOR 1-25	884 - 896	4.0	N/A	8.6	122.7
1160485792	2016-10-14 13:09:35	39358	SHIJIAN-16 (SJ-16)	643 - 646	8.3	O	12.9	147.9
1160484112	2016-10-14 12:41:35	28118	ATLAS 3B CENTAUR	313 - 349	11.9	R/B	10.3	174.6
1160479192	2016-10-14 11:19:35	40913	CZ-6 R/B	460 - 465	2.6	R/B	7.5	61.4

Table 4.3: ...continued from previous page.

Observation ID	START UTC	NORAD ID	Satellite/Debris Name	Range <i>km</i>	RCS <i>m</i> <sup>2</sup>	Operational Status	$\theta$ Degrees	Peak Flux Density (Jy/beam)
The detections below are from the night of 2016-09-09 from 10:43:34 UTC to 21:53:34 UTC								
1157493232	2016-09-09 21:53:35	41727	GAOFEN 3	790 - 811	3.9	O	14.7	256.4
1157486032	2016-09-09 19:53:35	19549	IUS R/B(1)	298 - 303	11.8	R/B	14.9	1606
1157474632	2016-09-09 16:43:35	20580	HST	551 - 583	28.1	O	9.3	1336.2
1157472832	2016-09-09 16:13:35	35931	OCEANSAT-2	731 - 741	4.1	O	2.9	113.7
1157472832	2016-09-09 16:13:35	41386	RESURS P3	479 - 489	7.7	O	1.6	121.9
1157468632	2016-09-09 15:03:35	20580	HST	590 - 633	28.1	O	22.0	1306
The detections below are from the night of 2016-09-08 from 10:47:34 UTC to 21:57:34 UTC								
1157407072	2016-09-08 21:57:35	41456	SENTINEL-1B	738 - 754	5.6	O	15.7	77.7
1157407072	2016-09-08 21:57:35	32382	RADARSAT-2	804 - 812	8.4	O	4.4	45.0
1157394472	2016-09-08 18:27:35	41026	YAOGAN 28	505 - 563	4.8	O	16.5	672.3
1157393872	2016-09-08 18:17:35	20978	DMSP 5D-2 F10 (USA 68)	840 - 846	3.9	NO	16.4	47.4
1157383672	2016-09-08 15:27:35	33504	KORONAS-FOTON	545 - 547	4.2	NO	2.6	47.2
1157382472	2016-09-08 15:07:35	15944	COSMOS 1674	546 - 570	8.7	N/A	10.2	44.3

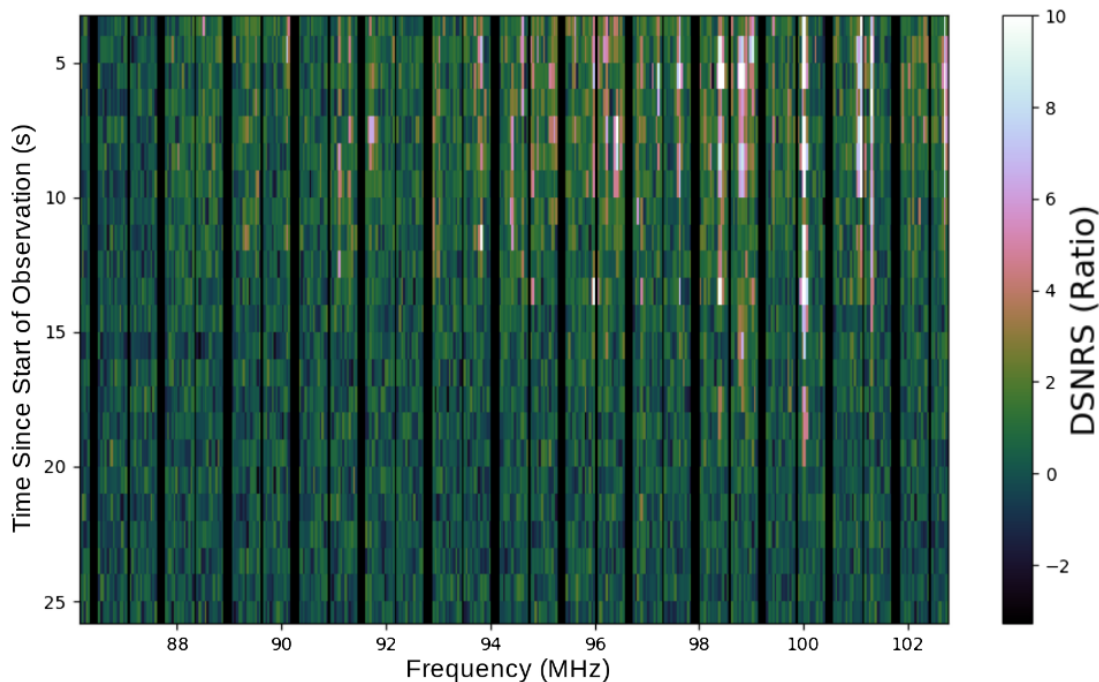


Figure 4.4: DSNRS plot for ZIYUAN 3 (ZY 3). The plot shows the different FM frequencies reflected by the satellite. The black vertical lines in the figure are due to the flagging of trailing, central, and leading fine frequency channels in every coarse channel.

## 4.5.2 Meteor Candidates

The observations from one of the nights used in this work (14 th December 2016) coincided with the Geminids meteor shower. The pipeline detected many reflections from objects that had angular speeds much greater than expected for LEO objects. These objects moved approximately 10 degrees in a single 2 s time-step and are FM reflections from the ionised trails of meteors, as previously observed by [Zhang et al. \(2018\)](#) with the MWA. An example is shown in [Figure 4.5](#). These events often appeared much brighter than satellites and were often pointing in the direction of the Geminids radiant.

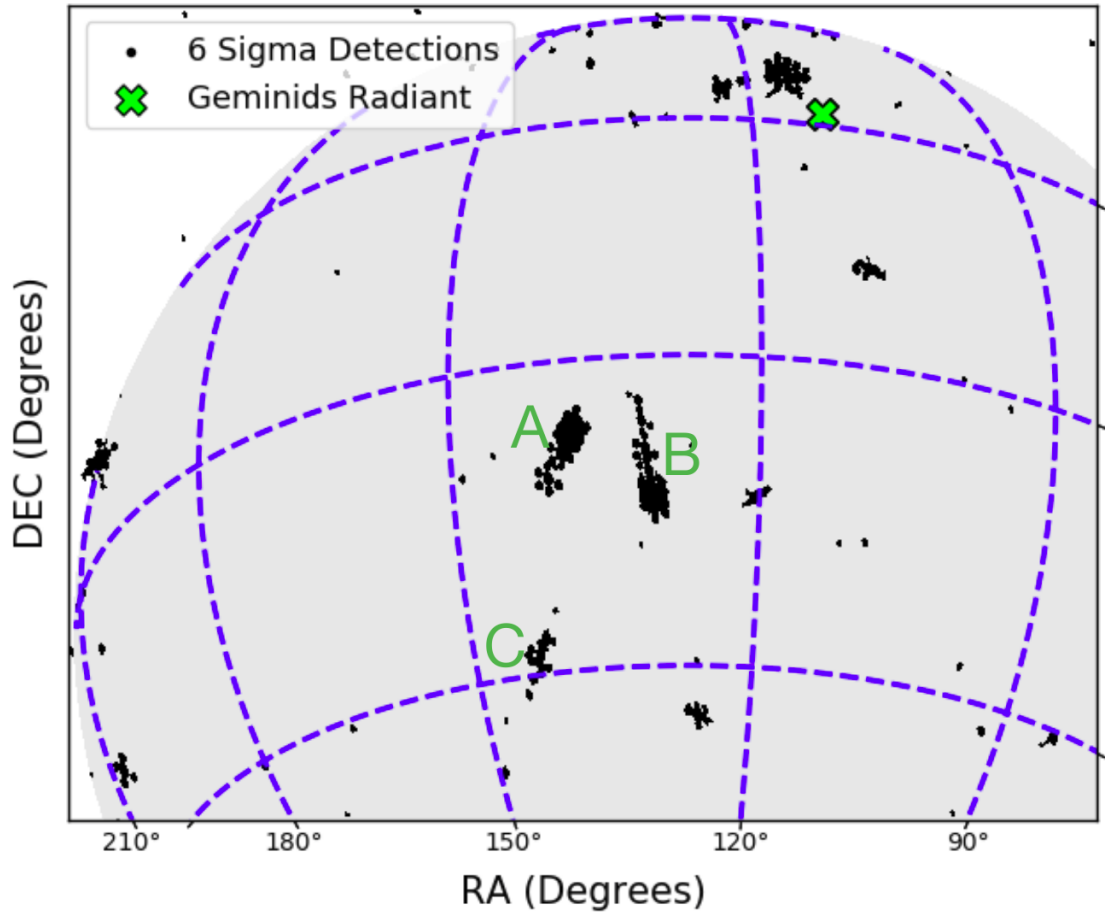


Figure 4.5: Three of the detected meteors are shown in regions A, B and C. Meteor-A and meteor-C point in the direction of the Geminids Radiant while meteor-B could be a sporadic meteor.

### 4.5.3 Aircraft

Nineteen aircraft passes were detected by the pipeline, due to their large reflecting areas and smaller line-of-sight distances. Most of these aircraft flew North-South over the MWA (a very common flight path for flights between Singapore/Malaysia/northern WA locations and Perth). These reflections appeared very bright (approximately 2800 Jy/beam peak flux density in a 30.72 MHz bandwidth difference image) and we utilised parallax to determine their altitudes (Section 4.4.3).

#### 4.5.4 Transmitters and Unknown Objects

Transmitters near the horizon were often detected. These transmitters are not removed through difference images as they are at a fixed azimuth/elevation and are highly variable, hence appear to move in celestial coordinates with time. In future observations, these azimuths/elevations will be masked in order to prevent the pipeline from detecting these transmitters. The transmitters are seen at multiple FM frequencies.

We also detected several events that had angular speeds very similar to LEO objects but did not coincide with any known orbits in the TLE catalog. These are likely to be either satellites with outdated TLEs or uncatalogued objects (intentionally or otherwise). In future, we will investigate these events further by performing orbit determination estimates.

#### 4.5.5 False Positives

The noise in difference images mainly consists of thermal noise and is assumed to follow Gaussian statistics. Due to the large volume of data used in this work, thermal noise fluctuations can trigger the  $6\sigma$  threshold of the detection pipeline, and hence it is important that we quantify these false positives. However, since we constrain the pipeline to allow only the brightest detection per time-step and per frequency channel, the number of false detections is reduced in the presence of a bright reflection event that is seen in multiple frequencies.

In order to investigate the number of false positives, we ran our pipeline again but only on the 380 fine channels outside the FM band (i.e outside 87.5–108 MHz, which is the FM band in Australia). By doing so, we only detect the false positives as the reflection events are confined to the FM band. Note that observations that had no transmitting satellites were used for this analysis, as the transmitted signals from satellites were not confined to the FM band.

We obtained an average of 13 false detections per minute, for the 380 fine frequency channels used. Thus for a full bandwidth observation, and in the absence



of any satellite detection, we would obtain approximately 26 false detections per minute. However, since we utilise other tools such as DSNRS (frequency and time analysis) and detection maps (position and time analysis), to investigate these events further, the probability of classifying one of these events as a LEO object is insignificantly small.

## 4.6 Discussion

### 4.6.1 Detection Completeness

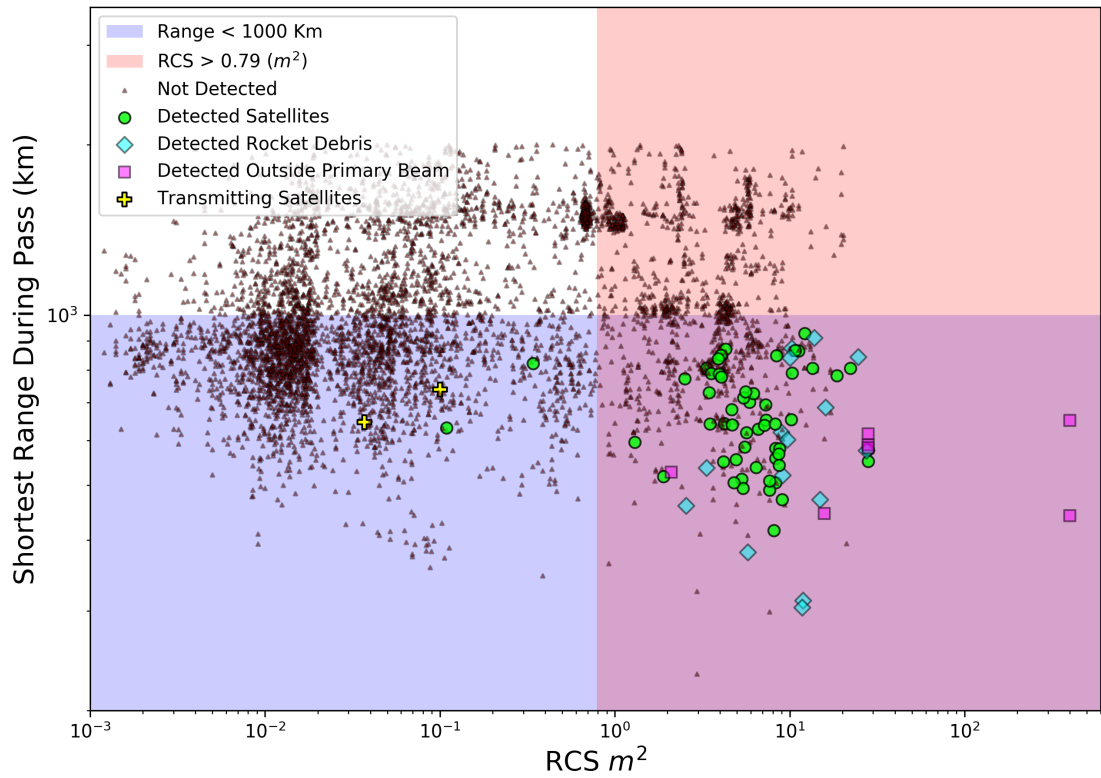


Figure 4.6: The RCS and the shortest range for all the satellites/debris passes above the horizon within the half power beam and with a range less than 2000 km. Note that although a satellite can appear in two consecutive observation IDs, it appears in the above plot as a single datum e.g. the ISS is detected in four observations according to Table 4.2, but only appears twice in the above plot (two rightmost points with the largest RCS) because those four observations covered two passes.

Tingay et al. (2013b) predicts that satellites with an RCS greater than  $0.79 m^2$  and with LOS range less than 1000 km can be detected using the MWA in the FM band using non-coherent techniques. All the satellites/debris that passed through the MWA's half power beam with a shortest range during a pass less than 2000 km were identified and their RCS, along with the shortest range during pass, are plotted in Figure 4.6. All of the detected objects in this work (except three CubeSats and one MiniSat) were detected within the theoretically predicted parameter space. Two of the CubeSats (DUCHIFAT-1 and UKUBE-1) were detected due to out-of band transmissions in the FM band (as previously observed by Zhang et al. (2018) and Prabu et al. (2020b)) and the other CubeSat and MiniSat were detected through FM reflections. Some satellites such as the ISS and Hubble Space Telescope (HST) were also detected outside the MWA's primary beam due to their large RCS.

From Figure 4.6 it can be seen that only 14% of the objects in the predicted parameter space were detected. This could be due to a number of reasons, for example unfavourable reflection geometries, or our pipeline being constrained to allow only one detection per time step per frequency channel. One significant reason could be that the RCS values are estimated by the US Space Surveillance Network (SSN)(R. Sridharan, 1998) using VHF/UHF/S-Band radars and are very likely to be quite different at the FM frequencies considered in this work. The RCS can also vary drastically as the transmitter-target-MWA reflection geometry changes and as the satellite tumbles. Also, the radar measured RCS is usually for a direct back-scatter/reflection where the transmitter and the receiver are co-located, as opposed to our method where we are looking at an oblique scattering of radiation (bi-static radar). Hence, we use the cataloged RCS values as an order of magnitude guide only. Also, since the classification of an event as a LEO object is done by visual inspection, it is possible that we missed detections near the horizon as it is usually crowded with many orbits due to projection effects as seen in Figure 4.2.

From Table 4.2 we can see that many satellites, such as the HST, were detected multiple times on the same night, demonstrating the MWA’s re-acquisition capability for large objects. Many objects such as rocket body debris and non-operational satellites were also detected, and for these objects passive space surveillance is the only way we can track them, thus demonstrating the MWA’s utility to track large obsolete objects. One such example is the object OPS 4467 A (NORAD ID 812). This satellite is the oldest object detected in our work and was launched in 1964.

Other interesting detected objects from Table 4.2 are MOZHAYETS-5 and RUBIN-5, which were launched together on the same rocket. RUBIN-5 was designed to stay attached to the payload adapter while MOZHAYETS-5 failed to detach from the adapter and hence they appear together as a single object in Table 4.2.

In one of the observations, the ISS was detected near the horizon with a peak flux density of 247,009 Jy/beam in one of the 40 kHz fine frequency channels. This could be due to a favourable reflection geometry and reflections from its very large solar panel arrays.

### 4.6.2 RFI Environment Analysis

There have been many recent studies that investigate the impact of satellite constellations on astronomy at optical, infrared and radio wavelengths (McDowell, 2020; Gallozzi et al., 2020; Hainaut & Williams, 2020). Here, along with demonstrating SDA capabilities with the MWA, we can use our data to examine the impact of the signals we detect on low frequency radio interferometers such as the MWA, or the future SKA, in the FM band. Rather than useful information on satellites in LEO, our signals can be considered disruptive sources of RFI. Understanding these signals as RFI in the MRO environment is of vital importance, as this is the site where the low frequency component of the SKA will soon be built.

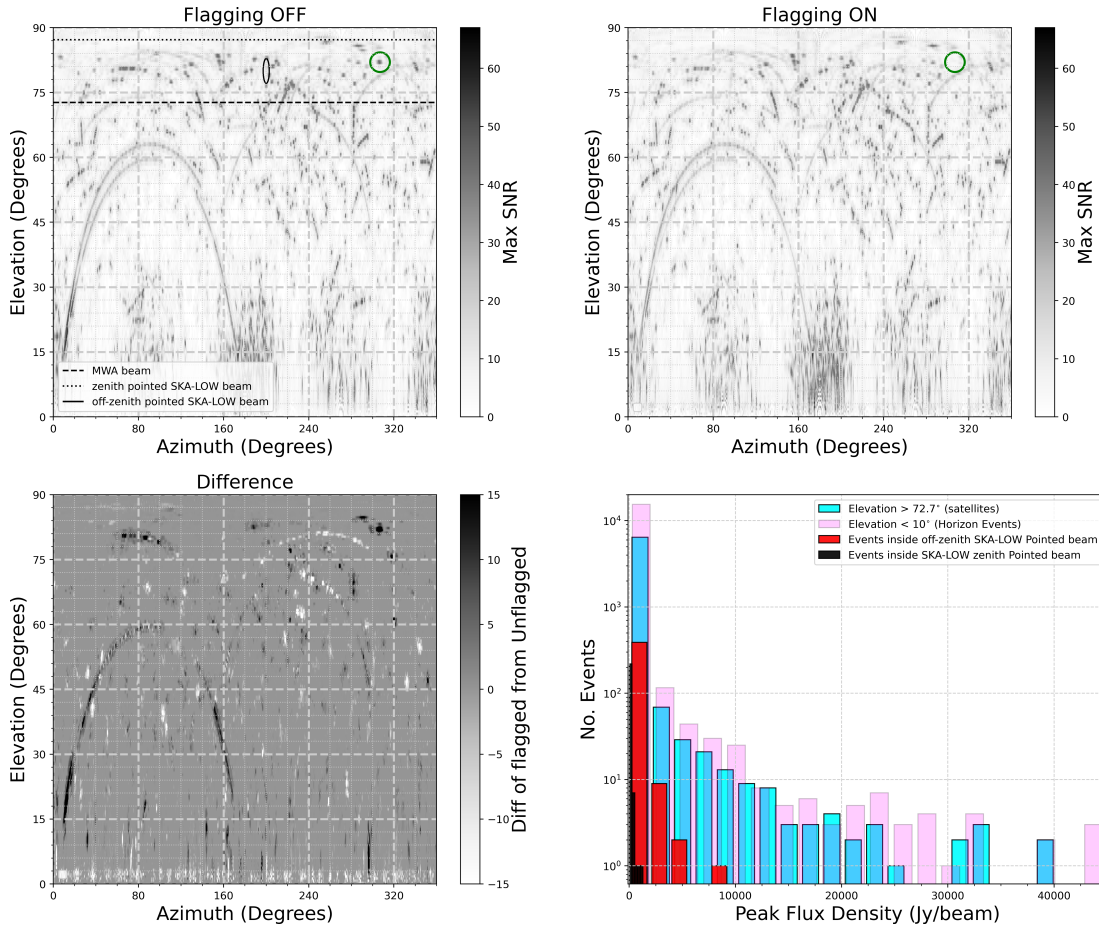


Figure 4.7: The Flagging OFF panel shows the maximum SNR detected using our pipeline at a given azimuth and elevation, using the data from Table 4.2). The panel also shows 2 different beam pointings for SKA-LOW station and 1 zenith pointed beam for MWA. The Flagging ON panel shows the events detected by the same pipeline after running AOFLAGGER on the measurement sets, applying the default built-in MWA flagging strategy. The event inside the green circle in the top two panels is an example of an event being flagged by AOFLAGGER. The bottom-left panel shows the difference of the two top panels (top-right subtracted from top-left), showing the different events detected by AOFLAGGER; black denotes signals detected and removed by AOFLAGGER, white denotes weaker signals revealed by the pipeline after AOFLAGGER has removed strong signals. The bottom-right panel shows the apparent peak intensity distribution for events detected in the different regions shown in the top-left panel and described in the text.

First we examine the data contained in Table 4.2 as a function of azimuth and elevation (data is binned in  $0.5^\circ$  resolution). In order to determine the maximum

impact of the RFI in any given direction, we plot the maximum SNR as a function of azimuth and elevation in the top-left panel of Figure 4.7. Complex structure across the sky from these sources of RFI are immediately apparent.

At low elevations ( $< 30^\circ$ ), we see periodicity in the strength of RFI detection as a function of azimuth. This reflects the sensitivity of the north-south dipoles (YY polarisation; sensitivity in east-west direction) and the east-west dipoles (XX polarisation; sensitivity in the north-south direction) that form the MWA antennas. Of these four sensitive horizon directions, we observe many high SNR events south of the array, due to the ducting of signals from powerful FM transmitters located in Perth and Geraldton (cities located south of the MWA).

We also note that we do not detect many high SNR events near the zenith (above an elevation of  $85^\circ$ ), perhaps due to inappropriate reflection geometries for the signal from transmitters near the horizon, but also likely due to the fact that the density of satellites in the sky is minimised toward the zenith (due to the projected volume of sky observed increases as we go away from the zenith). As the MWA beam was pointed toward the zenith, we can show the region within the beam as a constant zenith angle limit in Figure 4.7. For the MWA field-of-view at zenith, we can see a significant number of high SNR events within the MWA beam.

Similarly, we also indicate a zenith pointed beam for a single SKA-Low station, as well as an arbitrary off-zenith pointing (azimuth= $120^\circ$  elevation= $80^\circ$ ) for a SKA-Low station (all beams were approximated to be  $\lambda/d$ , where  $\lambda$  is the wavelength at 87.675 MHz and  $d$  is the diameter of the aperture, i.e. 35 m for a SKA-Low station and 5.65 m for an MWA tile). Note that the off-zenith pointed SKA-Low beam appears stretched due to different scales along x and y axes. Here we can see the advantages of a large station size for the SKA, especially when pointed at the zenith. At zenith (and in general), far fewer high SNR events are likely to corrupt SKA data. However, for off-zenith pointings, there is significant number of RFI events entering the SKA primary beam.

In order to then start to understand how RFI mitigation strategies commonly applied to MWA data perform in terms of identifying these signals and eliminating them from the data, we examined the performance of AOFLAGGER on these signals. AOFLAGGER is the default built-in flagging strategy for MWA data, applied as standard when data are obtained from the MWA archive. As explained earlier, we do not run AOFLAGGER in our pipeline, as we do not want to remove RFI.

We re-ran our full pipeline analysis of all datasets with the addition of the application of AOFLAGGER, and repeated the blind detection step on these flagged observations. The results of this analysis are shown in the top-right panel of Figure 4.7, in direct comparison to the top-left panel, which was obtained without the use of AOFLAGGER. The difference between the use of AOFLAGGER and not using AOFLAGGER is not significant, as most of the events detected by our blind detection pipeline were too faint to be detected by the flagging software. Some differences are highlighted in the comparison.

In order to examine the differences in detail, we plot the difference of the two plots (top-right panel subtracted from the top-left panel in Figure 4.7). This is shown in the bottom-left panel of Figure 4.7. The events shown in black are the events that have been detected and flagged by AOFLAGGER. We can see that the track of an aircraft (an inverted U trajectory going North-South in the figure) was detected by AOFLAGGER. But since our blind detection pipeline searches for signals in all fine-frequency channels, we still manage to find the aircraft in some of the fainter channels that were not detected by AOFLAGGER. The aircraft signals are a particularly interesting case to examine, as the reflected FM signals have a wide dynamic range across the observed frequencies. The aircraft signals are bright enough in some fine-frequency channels to be flagged by AOFLAGGER while also faint enough in other channels to be missed by AOFLAGGER (but detected in both cases by our blind detection pipeline). The aircraft example demonstrates the faint events probed by our detection method, events that are

faint enough to be missed by existing automated flagging strategies.

There are also some new events detected by the pipeline following the use of AOFLAGGER (shown in white in the difference panel), due to the brightest event being flagged by AOFLAGGER, allowing our pipeline to then detect the next brightest event. As described in Section 4.4.1, our pipeline is constrained to detect the brightest event in any given time step, at each frequency. After the application of AOFLAGGER, we detected a total of 3828 additional events, compared to not using AOFLAGGER. This immediately gives us an idea of the impact of our constraint to detect only the brightest events; the additional 3828 events represent a 12.56% increase, showing us that we are likely sacrificing 12.56% of events due to the choices made in the pipeline. While not a large effect, future refinements of the pipeline could include the use of AOFLAGGER to recover these events, as well as the use of the DSNRS technique to iteratively perform detection and flagging. Another alternative approach would be to incorporate peeling of the sources already detected, thus enabling the pipeline to detect the next brightest event. However, peeling requires creating a model of the source through CLEANing and hence is not considered in this work due to being computationally expensive.

While the use of the maximum detection SNR is useful to indicate the maximum impact of RFI in Figure 4.7, it is a function of the MWA's sensitivity. In order to use a measure that can indicate the impact on other telescopes, such as the SKA, the apparent flux density can be considered. The bottom-right panel of Figure 4.7 shows the peak intensity distribution for all the events detected: inside the zenith pointed MWA beam (mainly consisting of satellite events); inside the zenith pointed SKA beam; inside the arbitrarily pointed SKA beam; and for events near the horizon ( $< 10^\circ$ ). As the figure shows the apparent peak intensity (not primary beam corrected), the true intensity of the events near the horizon are orders of magnitude higher than apparent, as they were detected well outside the primary beam.

With 100s of events with intensities of 100s of Jy/beam predicted in an arbitrarily pointed SKA-Low beam over the course of a typical observation period, these signals will have to be considered when using the SKA in the FM band (or at any other frequency at which terrestrial transmitters commonly operate). The effect of RFI signals such as these on key science programs for the SKA (or MWA), such as the Epoch of Reionisation experiment, are complex. [Wilensky et al. \(2020\)](#) considers the threshold for RFI to have a significant effect on the EoR experiment and finds the threshold to be the result of a complex combinations of factors, such as the direction and strength of the RFI, the frequency and time occupancy of the RFI, and the detailed characteristics of the telescope being used.

While such an analysis is beyond the scope of this paper, the information presented here starts to give an indication of the radio astronomy impact of terrestrial transmissions that are reflected off objects in LEO.

## 4.7 Conclusion

We have built upon previous work using the MWA as a passive radar system by developing a semi-automated pipeline that searches for reflected signals from LEO satellites in high time and frequency resolution data. Previous detections were performed by manual inspection of full band-width difference images, and here we have dramatically increased the number of detections by searching autonomously in every fine-frequency channel.

Testing our pipeline on archived MWA data, we detected more than 70 unique LEO objects in 20 hours of observation. DUCHIFAT-1 and UKube-1 were detected due to spurious transmissions, while every other detected object was due to FM reflections. The large number of satellite detections through FM reflections alone prove MWA to be a valuable future asset for the global SDA network.

All, except four, of the detected objects were found to lie within the parameter space (range vs RCS) predicted by [Tingay et al. \(2013b\)](#). However, not all objects that were predicted to be detectable were detected. This could be due to a number



of reasons such as tumbling and unfavourable reflection geometries reducing the RCS of the object.

Along with the many satellite detections, we also detected FM reflections from Geminid meteors and aircraft flying over the MWA. Some detected events had angular speeds similar to LEO objects but did not have a satellite orbit match. In the future, we will further examine these unidentified objects by performing orbit determination. We will also use our data to demonstrate a detailed LEO catalog maintenance capability. The Gauss orbit determination technique (Curtis, 2013) will be utilised, as we only measure the angular migration of the objects with non-coherent techniques. In future, the detection pipeline used here will be upgraded to perform fully autonomous detections instead of the visual inspection performed here.

We also perform a preliminary analysis of the RFI environment at the Murchison Radio-astronomy Observatory, and estimate the impact of signals reflected from objects in LEO, which for astronomers constitute RFI, on the SKA. As part of this analysis, we examined the performance of the MWA's standard flagging strategy, based on AOFLAGGER, to detect and remove these RFI signals. We found that AOFLAGGER only found 13% of the signals our pipeline found. As such, careful consideration of future RFI flagging strategies for the MWA and the SKA should be given. These results also suggest future refinements for our pipeline.

Many satellites transmit at MWA frequencies for down-link telemetry. Hence, observing in these frequencies could expand our detection window beyond the feasible parameter space (RCS-range) shown in this work (observations at these frequencies will have to be performed using a modified form of the pipeline, as we will be detecting objects from LEO-GEO which have different angular speeds, thus requiring different integration times to make difference images). The future detection and characterisation of satellites that unintentionally transmit out of band will also assist in determining the threat of mega-constellations of small

satellites to ground-based radio astronomy facilities.

# Chapter 5

## Preliminary Orbit Determination

This chapter is a reproduction of Prabu, S. Hancock, P. Zhang, X. Tingay, S., “Demonstration of Orbit Determination and Catalogue Maintenance Capabilities for LEO Objects using the Murchison Widefield Array”. The manuscript is submitted to Publications of the Astronomical Society of Australia and is currently under review. The reader will encounter some repetition of material in the introductory sections. This chapter develops an orbit determination method using the non-coherent passive radar MWA observations.

### 5.1 Abstract

The rapidly increasing number of satellites in Earth orbit motivates the development of Space Domain Awareness (SDA) capabilities using wide field-of-view sensor systems that can perform simultaneous detections. We demonstrate a basic orbit determination method for Low Earth Orbit objects using the  $\sim 1300$  degree<sup>2</sup> field-of-view of the Murchison Widefield Array (MWA) at FM frequencies. Non-coherent passive radar techniques with the MWA produce spatially smeared detections, due to time averaging in the MWA’s standard signal processing chain. We develop methods to extract time-stamped measurements of a satellite’s angular coordinates from these data. We test our methods on 32 satel-

lite passes and use our extracted measurements to perform orbit determination for the targets using a least-squares fitting approach. The target satellites span a range in altitude and Radar Cross Section, providing examples of both high and low signal to noise detections. We validate our estimated orbital elements for the satellites against the publicly available Two Line Element (TLE) updates provided by the Space Surveillance Network (SSN) and find our determined [mean] orbital elements to be in close agreement<sup>1</sup>. We also test for re-acquisition for one target using our orbital elements and find the trajectory predicted by our method to coincide within  $0.2^\circ$  cross-track and  $0.3^\circ$  in-track directions for a subsequent pass, reduced to approximately  $0.1^\circ$  cross-track (less than one kilometre) if two passes are used to predict the subsequent pass (using simple two-body propagation). We find the median uncertainty in the angular position for objects in LEO (range less than 1000 km) to be 860 m in the cross-track direction and 780 m in the in-track direction, which are well within the typical uncertainty of  $\sim 1000$  m in the publicly available TLE information. Our techniques therefore demonstrate the MWA to be capable of being a valuable contributor to the global SDA community. Based on our understanding of the MWA SDA system, we also briefly describe methods to mitigate the impact of FM reflecting LEO satellites on radio astronomy observations, and how maintaining a catalog of FM reflecting LEO objects is in the best interests of both SDA and radio astronomy.

## 5.2 Introduction

For practical reasons the motions of a human-made object around the Earth are often approximated in terms of an idealised two body system that can be defined using six Keplerian/orbital elements. However, the approximation is only valid near the epoch at which measurements are made, as they change due to atmospheric drag and J2 effects (Mishne, 2004) (perturbations in orbit caused

---

<sup>1</sup>the uncertainties in the TLEs are publicly not made known, and hence we were not able to quantify the agreement between our determined TLE and the SSN published TLE

due to the Earth not being a perfect sphere). Hence, orbital elements must be updated and cataloged frequently in order to maintain a current and accurate understanding of the state of the near Earth space environment (Space Domain Awareness: SDA).

With the ongoing increase in the number of satellites in Earth orbit, catalog maintenance can be a challenging task. Thus we require multiple sensors to work together to perform detections at high rates, and maintain catalogs through data fusion. Some existing SDA sensors already work in pairs (Cordelli et al., 2019), consisting of one wide field-of-view (FOV) system that performs the detection of the objects along with preliminary orbit estimates, followed by precise orbit determination using higher resolution measurements obtained from instruments that often have a smaller FOV. In this paper, we aim to demonstrate a preliminary<sup>2</sup> orbit determination capability for Low Earth Orbit (LEO) objects using the Murchison Widefield Array (MWA) (Tingay et al., 2013a), using non-coherent passive radar techniques (Tingay et al., 2013b; Zhang et al., 2018; Prabu et al., 2020b,a) over very large FOVs at commercial FM frequencies ( $\sim 88$  MHz to  $\sim 108$  MHz in Australia). Radio telescopes such as Low Frequency ARray (LOFAR) (Klos et al., 2020, 2021) and the Italian Northern Cross telescope array (Losacco et al., 2018) have also been used to perform SDA observations, and recent studies (McDowell, 2020; Gallozzi et al., 2020; Hainaut & Williams, 2020; Mallama, 2020) have highlighted the importance of understanding the near-Earth space environment for astronomy in optical, infrared, and radio wavebands. Developing and maintaining a catalog of LEO objects known to reflect FM signals can help us understand the sources of Radio Frequency Interference (RFI) in the environment of the Murchison Radio Observatory (MRO) (Tingay et al., 2020), home to the MWA, ASKAP, EDGES, the future low-frequency Square Kilometre Array, and numerous other test arrays.

The MWA can perform SDA observations via the search for reflections of ter-

---

<sup>2</sup>Here we are not referring to the classical Gauss method, as often meant by the term "preliminary orbit determination" for angles-only detection among the SDA community.

restrial FM signals from satellites using standard radio astronomy imaging techniques, known as non-coherent passive radar. The detected signals are smeared, typically over a couple of degrees, mainly due to the motion of the satellites during individual observation periods (2s), as demonstrated in our previous work (Tingay et al., 2013b; Prabu et al., 2020b,a). The  $\sim$ second observation periods are driven by the MWA’s standard configuration for its primary astrophysics mission.

Deriving accurate angular position measurements and assigning time-stamps for these measurements can be a challenging task, due to these smearing effects. In this work, we describe methods to extract satellite angular position measurements from the spatially and temporally smeared data, and discuss how they can be used to determine orbital elements for the detected objects. The methods are tested on a subset of 32 LEO objects of varying altitude, inclination, Radar Cross-Section (RCS), and SNR reported in our previous work (Prabu et al., 2020a). We also test our satellite re-acquisition capability using predictions based on our methods, for multiple observations of the HST during different orbits.

Our motivation for demonstrating a catalog maintenance capability with the MWA is two-fold. Firstly, LEO catalog maintenance using the MWA is an added bonus output of the versatile MWA FM band observations performed for radio-astronomy purposes. As demonstrated in this work using archived MWA observations, any MWA FM band observations can be re-used for LEO catalog maintenance and do not require any SDA specific scheduling of observations, and hence is a cost-effective addition to the existing global SDA network. Second, its large FOV and 24/7 operational capability enables it to re-acquire LEO targets with ease. The orbital elements of LEO objects can vary significantly within a few hours, and the MWA’s FOV and ability to continuously monitor the LEO environment potentially makes it an essential SDA sensor in the age of satellite mega-constellations.

We briefly describe our non-coherent passive radar techniques in Section 5.3.

We discuss the methods developed to obtain satellite angular position measurements and how they can be used to perform orbit determinations in Section 5.4. We discuss our results from Section 5.5 in Section 5.6, followed by a brief conclusion of the work in Section 5.7.

## 5.3 Background

The MWA (Tingay et al., 2013a) is a radio interferometer built as a precursor to the low frequency component of the SKA. The MWA has 128 elements (each containing 16 dual polarised bow-tie antennas) that observe the radio sky from 70–300 MHz, and has an instantaneous bandwidth of 30.72 MHz. The MWA was designed for studying astronomical sources (Bowman et al., 2013; Beardsley et al., 2019) but has also been demonstrated to be a novel instrument for performing SDA observations (Tingay et al., 2013b; Palmer et al., 2017). Two different passive radar techniques have been developed for the MWA, namely coherent detection (Palmer et al., 2017; Hennessy et al., 2019; Hennessy et al., 2020) and non-coherent detection (Tingay et al., 2013b; Zhang et al., 2018; Prabu et al., 2020b,a), and in this work we focus on performing orbit determination using the data obtained from the non-coherent method.

The non-coherent detection method uses difference imaging on adjacent 2 s images to isolate transient events from the static background emission (Zhang et al., 2018). An example illustration of the difference imaging technique is shown in Figure 5.1. To increase the sensitivity of our search (as the signal of interest is narrow band), we split the MWA’s 30.72 MHz instantaneous bandwidth into 768 fine channels (each of 40 kHz bandwidth) and search for 6 sigma events in the difference images created for each of these fine channels at every time-step. A detailed description of the steps and pipeline can be found in Prabu et al. (2020b,a) and the reader is referred to these papers for further details.

We reported the detection of 74 objects in Prabu et al. (2020a). From these detections we have selected 32 satellite passes, of varying characteristics (Table

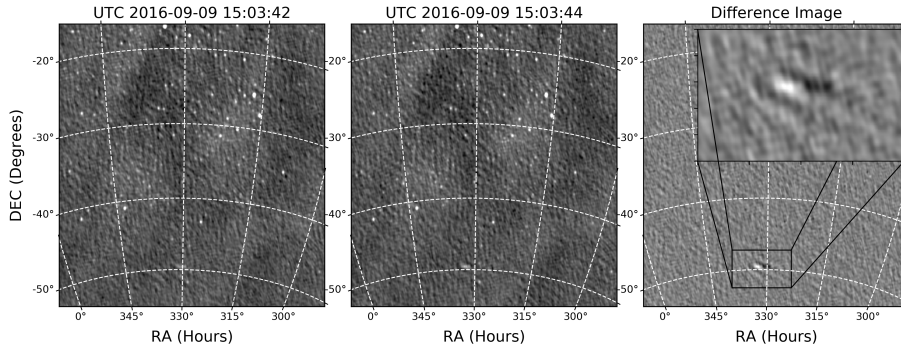


Figure 5.1: The left and the middle panel are consecutive 2s images of the sky as observed by the MWA, and the right panel illustrates how difference images can be used to isolate transient events from static background sources, as well as stationary imaging artefacts.

5.1) in order to test and demonstrate orbit determination<sup>3</sup>, using the information contained in the detections.

## 5.4 Methods

In order to perform orbit determination and demonstrate a catalog maintenance capability, we need to obtain multiple measurements of a satellite’s angular position during a pass from our difference image data. The MWA’s Phase 2 compact configuration (Wayth et al., 2018) has a  $\sim 15$  arcminute FWHM point spread function (PSF) at FM frequencies, and thus the detected signals in difference images appear elongated in both in-track and cross-track directions, as can be seen in Figure 5.2, due to PSF structure and the motion of the object during the observation period. We deal with these challenges in three steps as described in Section 5.4.1 in order to measure accurate time-stamped angular coordinates and then proceed to constrain the orbits in Section 5.5.1 using these measurements.

---

<sup>3</sup>In this paper, we define orbit determination as fitting a TLE (or mean orbital elements) to satellite passes that would enable us to reacquire targets during subsequent passes.



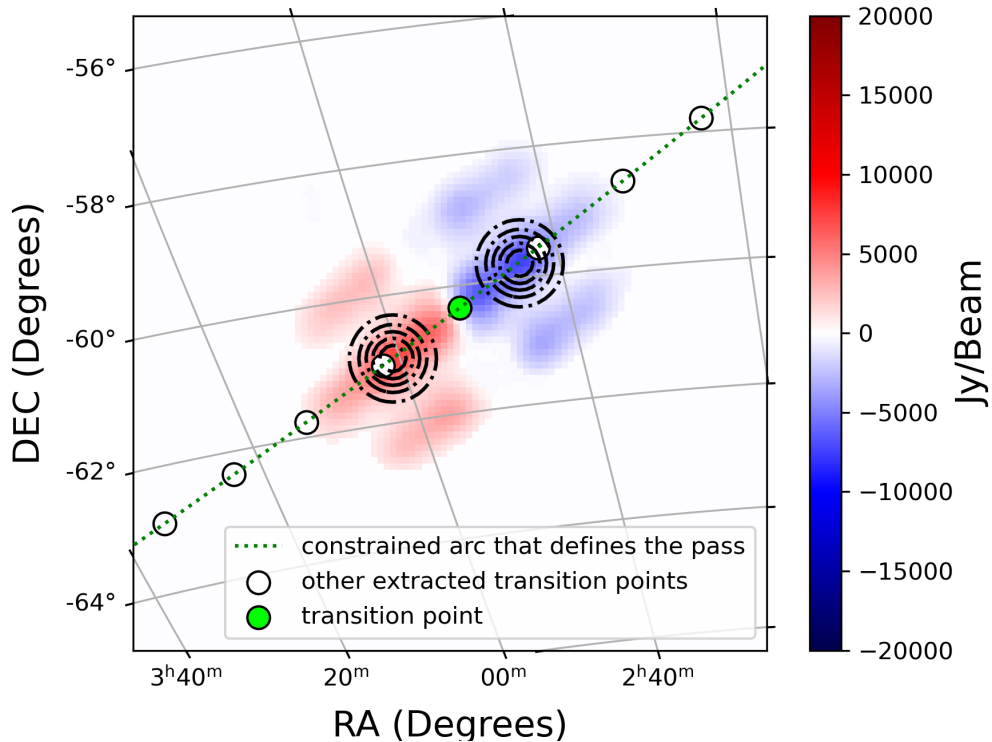


Figure 5.2: The reconstructed streak from the combined frequency information from difference images. The figure also shows the extracted measurement (transition point) as a green circle along with other measurements from adjacent time-steps as white circles. The dotted green line is the constrained arc described in Section 5.4.1. The Gaussian fits to the peak positive/negative pixels are also shown as black dotted contours.

## 5.4.1 Angular Coordinate Measurements

### 5.4.1.1 Signal Reconstruction

We have previously observed satellites to reflect FM signals at multiple frequencies (Tingay et al., 2013b; Prabu et al., 2020b,a). Sometimes, for weak reflection events, different parts of the satellite track are visible at different frequencies. So, as step 1, we combine our detections across different frequency channels to obtain a higher signal to noise measurement, in order to reconstruct the satellite track more accurately via the aggregation of detections at different frequencies. We

extract and combine the positive head and the negative tail of detected streaks (see Figure 5.2) from different fine frequency channels using our source finding software `RFISeeker`<sup>4</sup>, that was developed during our previous work (Prabu et al., 2020a). The combined detection is then corrected for primary beam attenuation using a primary beam model (Sokolowski et al., 2017) generated at the observed frequency.

#### 5.4.1.2 Constraining Cross-Track Structure

Since the curvature of the satellite’s pass is not resolved by the MWA on the 2s timescales of our difference images (as can be seen in Figure 5.2), the cross-track elongation of the signal can be attributed to PSF structure alone. Hence, as step 2, we characterise the cross-track structure by fitting a model of the PSF to the detected streak. We fit a Gaussian model of the PSF (statistical significance of the method is explained in Condon (1997)) to the peak maximum (and minimum) pixel in the head (and tail) of the streak. The model fitting is performed using `scipy.curvefit`<sup>5</sup> and the  $1\sigma$  uncertainties of the fit location are calculated using the square-root of the diagonal elements in the returned co-variance matrix. The average uncertainty in the Gaussian fit location was found to be under 5% of the full width at half maximum (FWHM) of the PSF, approximately 0.75 arcminutes. Repeating the same step for the heads and the tails detected at multiple time-steps, constrains the orbital pass to an arc (with an average cross-track error less than 5% of PSF FWHM). Note that the location of the peak [maximum/minimum] pixel in the streak may depend on the altitude of the satellite as well as the FM illumination pattern of the apparent MWA sky. Hence, the time stamp information of these peak pixels cannot be determined without constructing a comprehensive model of the apparent FM illumination, and is beyond the scope of this work.

---

<sup>4</sup><https://github.com/StevePrabu/RFISeeker>. More information on the usage of the software can be found in (Prabu et al., 2020a)

<sup>5</sup>[https://docs.scipy.org/doc/scipy/reference/generated/scipy.optimize.curve\\_fit.html](https://docs.scipy.org/doc/scipy/reference/generated/scipy.optimize.curve_fit.html)

### 5.4.1.3 Constraining In-Track Structure

The in-track structure of the streak is mainly due to the motion of the satellite during the 2s observation period. Since we perform difference imaging by subtracting the image at time-step  $t - 1$  from the image at time-step  $t$  (Zhang et al., 2018; Prabu et al., 2020b,a), the location of the satellite at the beginning of time-step  $t$  corresponds to the point where the streak transitions from the negative tail to the positive head, and the corresponding time-stamp can be found using the header time information provided in the two images used<sup>6</sup>. Hence, as step 3, we obtain our final time-stamped angular measurements of the pass, by determining the point where the re-constructed streak signal transitions from head to tail along the constrained arc (as shown with green markers in Figure 5.2). Similarly doing so for every detected streak provides us with multiple timestamped angular measurements. These values are used to perform orbit determination in Section 5.5.1

---

<sup>6</sup>We use `wsclean` (Offringa et al., 2014; Offringa & Smirnov, 2017) to create MWA sky images and the software uses the mid UTC time of the integration as the *OBS-DATE* parameter in the image header.

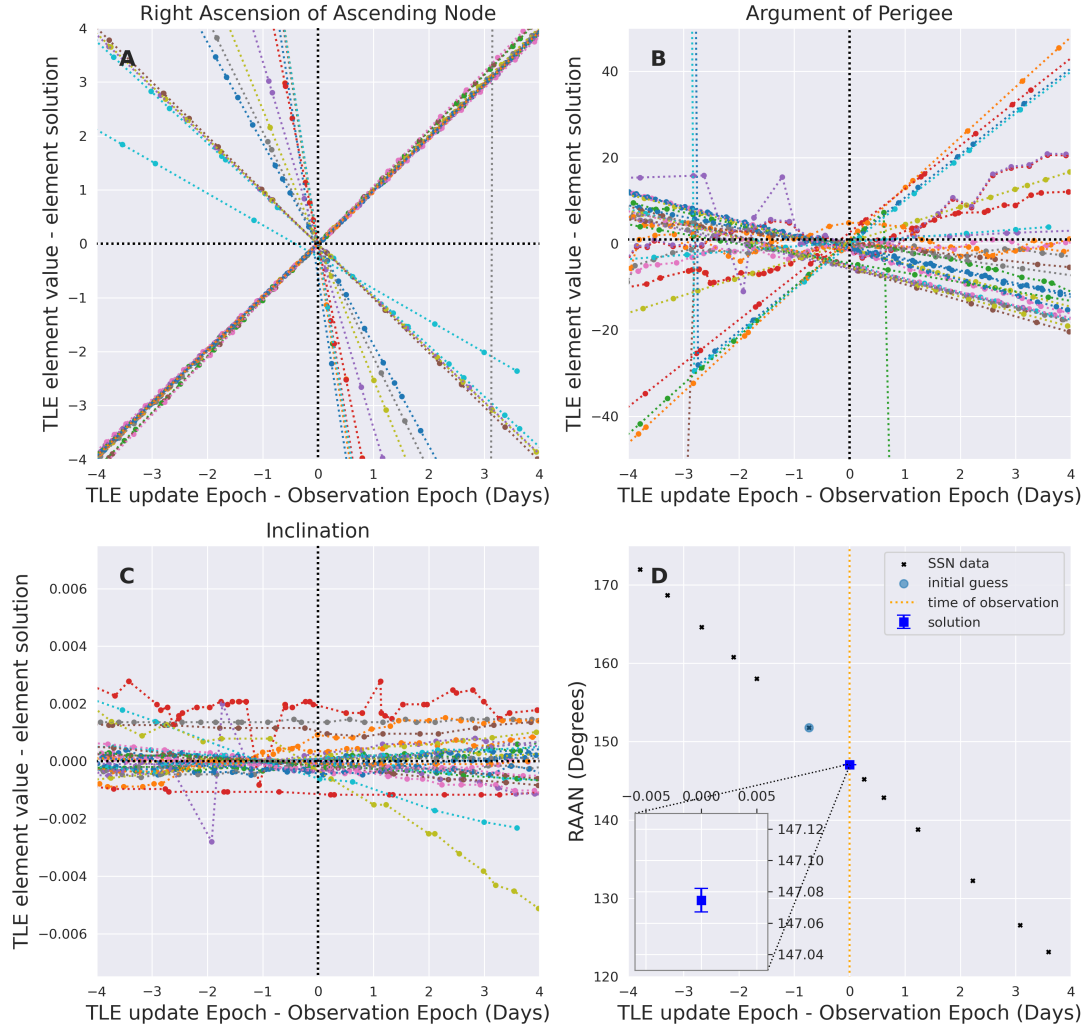


Figure 5.3: In panels A, B and C, we show the historic evolution of  $raan$ ,  $aop$ , and  $i$  for all the objects listed in Table 5.1, relative to our solutions. Panel D shows the historic values of  $raan$  obtained near the epoch of observation (for the HST event detected in observation 1165762576). We show the initial guess used by our pipeline as a blue circle marker, along with our determined value (with  $2\sigma$  uncertainties) at the epoch of the observation. We use the closest epoch TLE to propagate the satellite's position to the epoch of our observation.

Table 5.1: List of observations and target objects used for orbit determination in this work. The observation IDs<sup>9</sup> for all the satellite passes used in this work. The table also lists the corresponding UTC time for the observations, along with the NORAD ID for the satellite detected in the observation, and its Radar Cross-Section (RCS)<sup>10</sup>.  $N_{\text{meas.}}$  is the number of detections of the object during the observation period. We also report the determined orbital elements (along with the  $1\sigma$  error on the last digit within brackets) for each of these objects and the RMS in-track and cross-track residuals (in arc-minutes) after the fit.

Obs ID DATE UT	START UT STOP UT	OBJ. NAME NORAD	RCS ( $m^2$ ) $N_{\text{meas.}}$	raan ma	e mm	aop i	in-track (RMS) cross-track (RMS)
1157468632	15:03:35	HST	28.0799	61.675(2)	0.000289(1)	38.4(6)	2.6'
2016-09-09	15:05:27	20580	12	232.5(6)	15.0848526(4)	28.4700	2.5'
1160497672	16:27:35	ISS(ZARYA)	399.0524	182.0035	0.000655(6)	73.3056	6.6'
2016-10-14	16:29:27	25544	15	144.36648(3)	15.54191(4)	51.6421(2)	19.1'
1160497672	16:27:35	UKUBE-1	0.118	26.8606	0.0005614	118.1(3)	2.4'
2016-10-14	16:29:27	40074	5	215.7(3)	14.832312(3)	98.3375	4.6'
1160497552	16:25:35	ISS(ZARYA)	399.0524	182.0104	0.0006740(1)	73.29(3)	3.0'
2016-10-14	16:27:27	25544	19	140.9332(3)	15.54191(4)	51.6421(2)	1.3'
1160496232	16:03:35	GPM-CORE	8.104	34.749(1)	0.0009966(1)	273.28(2)	16.0'
2016-10-14	16:05:27	39574	7	56.35(2)	15.55243(6)	65.01180(6)	20.2'
1160495752	15:55:35	ARIANE40+3R/B	9.7046	202.8305	0.0016951(4)	353.7765(5)	2.8'
2016-10-14	15:57:27	23608	8	212.8078(7)	14.959279(8)	98.2094	5.5'
1160493592	15:19:35	GAOFEN2	3.506	6.1414	0.0007181(1)	200.8(2)	6.5'
2016-10-14	15:21:27	40118	16	132.2(2)	14.8058657(2)	97.9507	5.5'
1160493472	15:17:35	DUCHIFAT-1	0.037	195.3847	0.0014248(2)	40.2530(3)	2.5'
2016-10-14	15:19:27	40021	5	167.6723(9)	14.895209(3)	97.9214	4.3'

Table 5.1: ...continued from previous page.

Obs ID	START UT	OBJ. NAME	RCS ( $m^2$ )	raan	e	aop	in-track (RMS)
DATE UT	STOP UT	NORAD	$N_{\text{meas.}}$	ma	mm	i	cross-track (RMS)
1160493472	15:17:35	SPOT4	6.193	5.60(1)	0.0012212	313.5(4)	47.2'
2016-10-14	15:19:27	25260	23	20.6(4)	14.53434552	98.3715	68.3'
1160487832	13:43:35	OKEAN-4	7.1433	349.2752	0.0020528(1)	160.9(6)	10.1'
2016-10-14	13:45:27	23317	8	171.8(6)	14.872731(1)	82.53949(7)	0.8'
1160485792	13:09:35	SHIJIAN-16(SJ-16)	8.2723	148.82350(2)	0.0018570(6)	102.9(4)	4.2'
2016-10-14	13:11:27	39358	9	104.5(4)	14.8528152(1)	74.97430(4)	0.7'
1165766176	15:55:59	KANOPUS-V1	1.9	263.8922	0.0001989	70.2475(6)	6.2'
2016-12-14	15:57:51	38707	15	136.8321(6)	15.2001829(1)	97.4517	8.5'
1165762576	14:55:59	HST	28.0799	147.0746(3)	0.00027370(2)	351.1(8)	4.4'
2016-12-14	14:57:51	20580	10	286.0(8)	15.08620(3)	28.46880(7)	0.9'
1165761136	14:31:59	ZIYUAN3-1(ZY3-1)	5.315	55.5670	0.00010559(8)	74.7(2)	7.3'
2016-12-14	14:33:51	38046	14	257.59(2)	15.213742(3)	97.3105	6.5'
1165760776	14:25:59	COSMOS1328	8.2828	60.1338(1)	0.00111030(2)	167.3(1)	3.7'
2016-12-14	14:27:51	12987	11	165.7(1)	15.071518(4)	82.516(0)	0.3'
1165755976	13:05:59	COSMOS1544	8.2989	213.2614	0.0014169(0)	341.81638(2)	13.4'
2016-12-14	13:07:51	14819	16	226.1142(5)	15.25249645(1)	82.48479(1)	5.5'

Table 5.1: ...continued from previous page.

Obs ID	START UT	OBJ. NAME	RCS ( $m^2$ )	raan	e	aop	in-track (RMS)
DATE UT	STOP UT	NORAD	$N_{\text{meas.}}$	ma	mm	i	cross-track (RMS)
1165752856	12:13:59	SPOT1	7.279	21.129(2)	0.0141920(5)	257.8539(1)	3.7'
2016-12-14	12:15:51	16613	7	73.5564	14.6484554(1)	98.7430(1)	0.9'
1165771216	17:19:59	GOSAT(IBUKI)	4.6494	97.0669	0.0001526	91.8756	66.3'
2016-12-14	17:21:51	33492	3	241.45160(2)	14.67526130(1)	98.1110	59.4'
1165753936	12:31:59	COSMOS1766	8.2879	204.2835	0.001571(1)	31.6(1)	4.8'
2016-12-14	12:33:51	16881	14	175.5(1)	15.09860(8)	82.50508(4)	1.2'
1165753936	12:31:59	ATLAS2CENTAURR/B	14.8664	122.91(1)	0.642931(4)	248.20(2)	3.3'
2016-12-14	12:33:51	23968	20	3.079(3)	3.365053(5)	26.72361(1)	2.3'
1165773496	17:57:59	YAOGAN24	4.2274	105.7079	0.0016264	309.38(3)	4.0'
2016-12-14	17:59:51	40310	5	24.7(3)	14.7706137(2)	97.98487(4)	8.6'
1165771096	17:17:59	FGRST(GLAST)	4.9326	179.10(5)	0.0012252(2)	308.6(1)	3.9'
2016-12-14	17:19:51	33053	7	331.0(1)	15.107828(2)	25.58160(1)	1.5'
1165764136	15:21:59	IRS-P4(OCEANSAT)	3.4542	67.0832	0.00043390(5)	114.3260(9)	5.9'
2016-12-14	15:23:51	25758	6	219.0281(1)	14.523170(7)	98.17660(1)	6.1'
1165761376	14:35:59	H-2AR/B	27.4086	184.5777	0.00182159(2)	80(1)	2.9'
2016-12-14	14:37:51	41341	8	157.7(1)	15.040126(7)	30.6257(3)	1.4'

Table 5.1: ...continued from previous page.

Obs ID	START UT	OBJ. NAME	RCS ( $m^2$ )	raan	e	aop	in-track (RMS)
DATE UT	STOP UT	NORAD	$N_{\text{meas.}}$	ma	mm	i	cross-track (RMS)
1165761256	14:33:59	ZIYUAN3-1(ZY3-1)	5.315	55.5683	0.00010559(1)	74.49(2)	5.4'
2016-12-14	14:35:51	38046	5	260.44(2)	15.213743(5)	97.31052(5)	4.9'
1165758616	13:49:59	METOP-A	11.2479	46.0404	0.00013536(4)	48.530(7)	3.3'
2016-12-14	13:51:51	29499	5	284.656(7)	14.21485052(3)	98.7065	5.5'
1165757056	13:23:59	ENVISAT	18.597	36.2852	0.0001173	83.980(8)	4.6'
2016-12-14	13:25:51	27386	11	249.480(8)	14.3788361(8)	98.25991(3)	6.2'
1160491192	14:39:35	COSMOS2082	10.7604	8.5789(6)	0.00136930(2)	35.1(8)	1.1'
2016-10-14	14:41:27	20624	3	296.4(8)	14.14209(2)	71.04320(2)	0.5'
1160484112	12:41:35	ATLAS3BCENTAURR/B	11.93	43.4793	0.3205425(1)	303.20(1)	24.6'
2016-10-14	12:43:27	28118	4	351.242(9)	9.06535(6)	28.1480(1)	13.4'
1157474632	16:43:35	HST	28.0799	60.629(1)	0.00029159(1)	39(1)	8.7'
2016-09-09	16:45:27	20580	18	253.2(1)	15.084844(6)	28.469(2)	0.7'
1157472832	16:13:35	RESURSP3	7.66	346.0609	0.00042382(9)	20.8(3)	4.9'
2016-09-09	16:15:27	41386	3	311.8(3)	15.3223449(3)	97.2829(4)	6.3'
1157407072	21:57:35	RADARSAT-2	8.381	258.6263	0.0001236(7)	95.28(2)	2.6'
2016-09-08	21:59:27	32382	4	110.8(2)	14.29982302	98.57728(2)	6.4'



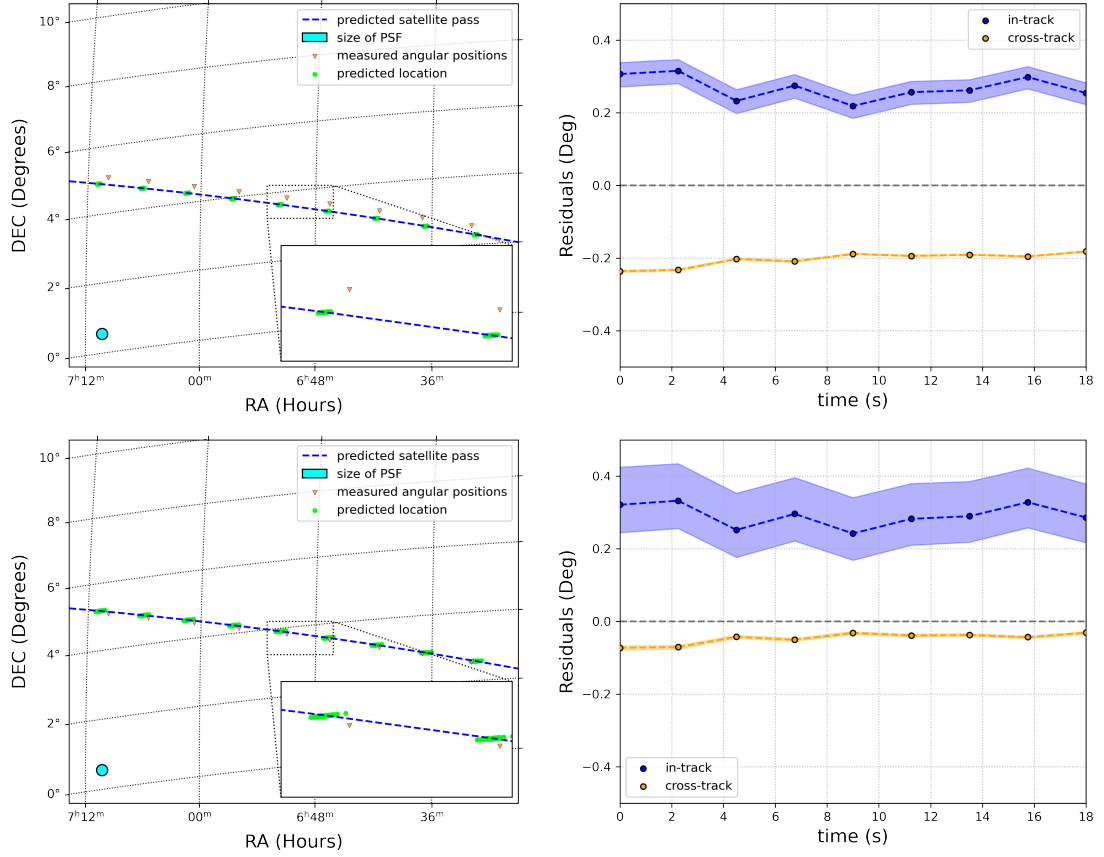


Figure 5.4: The measured HST pass using observation 1165768696 along with the predictions derived using measurements from a single prior orbit (panels A and B) and derived from measurements from two prior orbits (panels C and D). The predicted trajectory of the pass using our orbital element solutions are shown as a blue dashed line. The measured angular positions of the satellite are shown as orange triangle markers and the predicted positions through MC sampling of the errors associated with the orbital elements are shown as green circle markers. We also show the approximate size of the zenith pointed PSF of the observation as a cyan ellipse in the bottom left of panels A and C.

## 5.5 Results

### 5.5.1 Determining the Orbital Elements

Most modern SDA sensors perform orbit determination using instantaneous position vector (range) and instantaneous velocity vector (Doppler) measurements

of the satellite during the pass. The three orthogonal components of these two vectors in Euclidean space are used to analytically/numerically (JansenSturgeon et al., 2019) solve for the six orbital parameters, namely inclination ( $i$ ), argument of perigee ( $aop$ ), eccentricity ( $e$ ), right ascension of ascending node ( $raan$ ), mean motion ( $mm$ ), and mean anomaly ( $ma$ ). Angles-only orbit determination can also be performed using methods such as the Gauss and Laplace methods (Curtis, 2013), however these methods do not work under all scenarios for fast moving LEO objects (as also described by Hwang et al. (2019) and Wijnen et al. (2020)), and are often only used with success for heliocentric objects with smaller apparent angular speed such as asteroids, comets, and Kuiper belt objects (Celletti & Pinzari, 2006). The non-coherent passive radar techniques used in this work are confined to angles-only measurements. Upon testing angles only orbit determination methods, we often obtained poor solutions for  $e$ ,  $ma$ , and  $aop$ .

In order to use our measurements for orbit determination, we constrain the orbital elements by performing a least-squares fit of the predicted trajectory with our angular measurements. We obtained the publicly available Two-Line Element (TLE)<sup>11</sup> descriptions of the orbital elements for the objects we have selected<sup>12</sup> and used the closest TLE in time prior to our observations as the initial guess for the object’s orbital elements. Orbital element  $ma$  from the other published TLEs could not be used as the initial guess as its value is dependant on the satellite location (and hence it would be different for different observation locations that see the satellite at different times). Mean anomaly can be calculated as  $2 \times \pi \frac{t}{T}$ , where  $T$  is the orbital period and  $t$  is the time since perigee. Hence, we use Equation 5.1 to propagate the previously observed mean anomaly to the epoch of observation.

$$ma_t = (epoch_t - epoch_{t-1}) \times mm_{t-1} \times 360 + ma_{t-1} \quad (5.1)$$

---

<sup>11</sup>more information on the structure of TLE can be found in <https://www.celestrak.com/NORAD/documentation/tle-fmt.php>

<sup>12</sup>using the API query feature of [space-track.org](https://space-track.org)

where  $ma_{t-1}$  is the mean anomaly from a previous TLE update,  $(epoch_t - epoch_{t-1})$  is the time elapsed since the observation time from the previous TLE update<sup>13</sup>, and  $mm_{t-1}$  is the mean motion from the previous observation. Since  $mm$  is the average number of revolutions per day, and because  $ma$  increases linearly with time (irrespective of the orbit being circular or elliptical), the initial guess for  $ma$  at time  $t$  can be determined using Equation 5.1.

We fit for the orbital parameters in two steps. First, we allow only the elements with large expected variation to vary (i.e,  $raan$ ,  $ma$ , and  $aop$ ) to find the global minimum using `scipy.basinhopping`<sup>14</sup>. Second, we perform fine tuned adjustments of all six elements using `scipy.curve_fit`<sup>15</sup>.

To encourage convergence, we set boundary conditions to the six elements in both the fitting steps. The boundary condition for an orbital element is determined by inspecting the maximum variation in the orbital element value over the course of the past 60 days. This method seemed to provide good limits not just for passive objects, whose orbits primarily change due to atmospheric drag alone, but also for active objects with manoeuvring capabilities. The orbit estimates obtained for each of the 32 satellite passes are given in Table 5.1. We report the orbital elements up to the precision required to generate TLEs.

From Section 5.4.1.2, we know that the typical positional uncertainty in our individual angular position measurements to be less than an arcminute. Hence, we calculate the  $1\sigma$  uncertainties associated with our orbital elements by performing a Monte-Carlo (MC) (Metropolis & Ulam, 1949) re-sampling from a 2D normal distribution of angular positions (with standard deviation equal to the error in the angular position measurement). The uncertainties we estimate are listed in Table 5.1. If our measured error in the orbital element is larger than the

---

<sup>13</sup>The UTC time of TLE update can be determined using the "EPOCH" parameter that is returned when using the `tle_query` class from the `spacetracktool` <https://pypi.org/project/spacetracktool/> python module

<sup>14</sup><https://docs.scipy.org/doc/scipy/reference/generated/scipy.optimize.basinhopping.html>

<sup>15</sup>[https://docs.scipy.org/doc/scipy/reference/generated/scipy.optimize.curve\\_fit.html](https://docs.scipy.org/doc/scipy/reference/generated/scipy.optimize.curve_fit.html)

precision required to generate TLEs, then we report the error in the last digit within brackets. For some of the objects in Table 5.1, we were able to obtain more position measurements than for other objects (due to being detected in more time-steps), and hence were able to better constrain the orbital elements with smaller uncertainties. Also, due to using 2D projected data (RA-DEC) of the 3D motion of the satellite, the uncertainties were often found to be highly coupled (e.g,  $\Delta ma$  and  $\Delta aop$  reported in Table 5.1 were found to be almost always equal in value. The trace of  $ma$  and  $aop$  during the MC sampling almost always had a correlation coefficient of approx.  $-1$ ). We project our residuals ( $fit - measured$ ) for every orbit determination into in-track and cross-track directions and list the RMS of the residuals in these two directions in Table 5.1<sup>16</sup>.

### 5.5.2 Validation of Results

The orbital elements obtained from our method were verified against the TLE values available via the SSN near the epoch of observation. Our values were in close agreement with the orbital elements extracted from the TLEs. For all the events detected in Table 5.1, we show the fractional historic evolution of their orbital elements ( $raan$ ,  $aop$  and  $i$ ) in panels A, B and C of Figure 5.3. We see that most of the parameter trends go through the origin (they don't have to as the influence of drag on a tumbling LEO object with varying drag ram area is very complex) and our solutions are in good agreement with the public TLE values from near the epoch of observation.

We also show an example for one of the orbital elements ( $raan$  for HST pass during the observation 1165762576) in panel D of Figure 5.3. Figure 5.3.D also shows the initial guess used by our pipeline, and our  $raan$  solution with  $2\sigma$  uncertainty. We also test the dependence of the converged solution and find it to be independent of the initial guess used by the pipeline (more information in Appendix A.2).

---

<sup>16</sup>A demo pipeline of the scripts used to perform angular measurement extraction and orbit determination can be found in <https://github.com/PhD-Misc/MWA-OrbitDetermination>.

### 5.5.3 HST Re-Acquisition

During one of the four observation periods used during our LEO blind survey using the MWA ([Prabu et al., 2020a](#)), the HST was observed four times (more information in [Table 5.2](#)) on one of the nights. We use these observations to test for re-acquisition of the satellite based on our estimated orbital elements.

Table 5.2: Information on the HST observations described in Section 5.5.3

Obs ID	Start UTC	Stop UTC	time-steps detected	additional comment
1165756576	2016-12-14 13:15:59.0	2016-12-14 13:17:51.0	2	Used for 2-pass orbit determination (Section 5.5.3.2).
1165762576	2016-12-14 14:55:59.0	2016-12-14 14:57:51.0	10	Used for 1-pass orbit determination (Section 5.5.3.1). Used for 2-pass orbit determination (Section 5.5.3.2)
1165768696	2016-12-14 16:37:59.0	2016-12-14 16:39:51.0	13	Used to test for target re-acquisition using our determined orbital elements

### 5.5.3.1 One Pass Re-Acquisition

We use the orbital elements obtained for the HST during the observation 1165762576 (part of Table 5.1) to predict the subsequent HST pass that was visible to the MWA (observation 1165768696). The two observations are approximately 100 minutes apart. Panel A of Figure 5.4 shows the predicted trajectory using our determined orbital elements as the blue dashed line the predicted positions (using MC sampling of the orbital elements) as green markers. We see that the predicted trajectory and the measured trajectory (inverted red triangles) match to within  $0.2^\circ$  (1.9 km at the HST altitude) in the cross-track direction and  $0.3^\circ$  (2.8 km at the HST altitude) in the in-track direction. We calculate and plot the in-track and cross-track offsets between the predicted angular position and the measured positions of each of the MC walkers in Panel B of Figure 5.4.

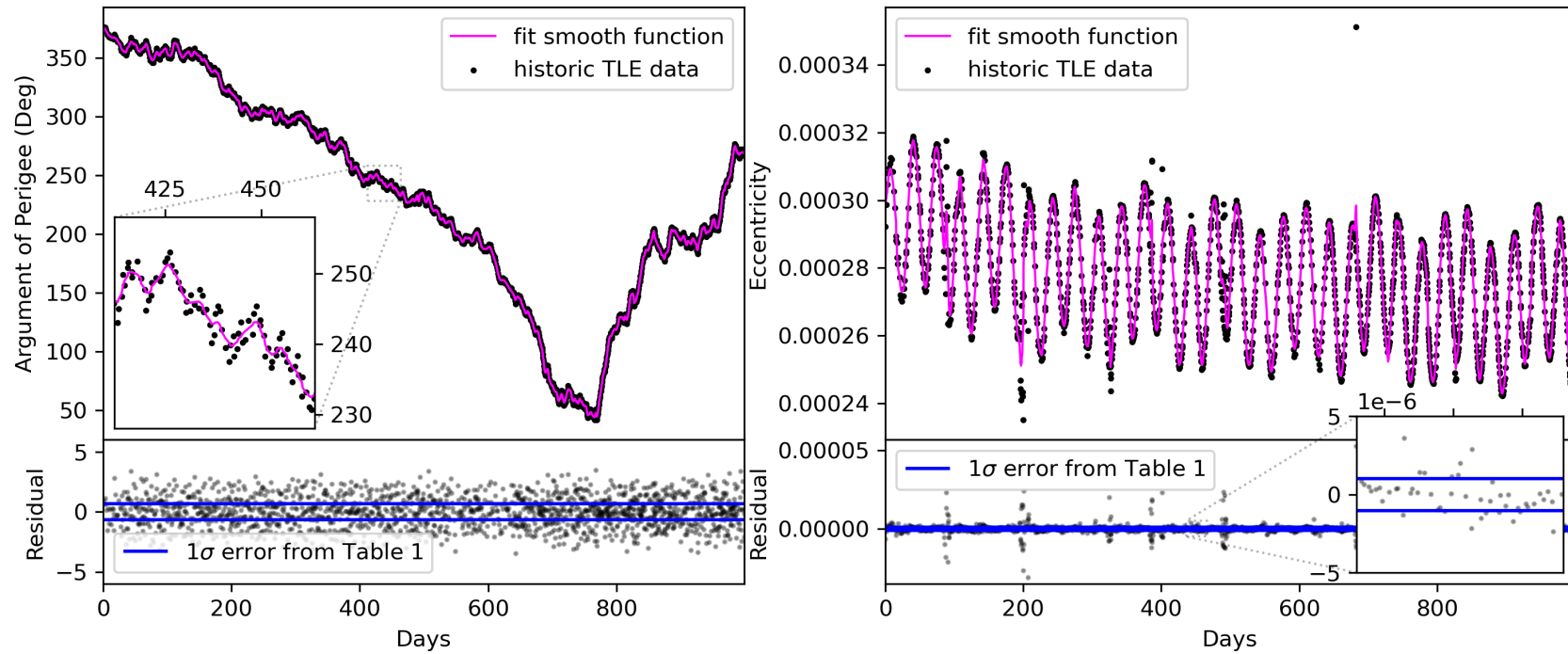


Figure 5.5: Figure shows the historic evolution of  $aop$  and  $e$  for HST over a 1000 days. The residual panel of each figure shows the estimated random error in the reported TLE updates along with our reported errors (in Table 5.1) for  $aop$  and  $e$ . Note that the order of magnitude of the scatter in  $e$  that we are interested in, is shown in the insert panel.



### 5.5.3.2 Two Pass Re-Acquisition

We also test our orbit determination method using angular position measurements obtained for the HST from two subsequent passes, i.e 1165762576 (used for one pass-re acquisition in the previous section) along with angular position measurements from the previous (100 minutes prior) HST orbit observation 1165756576. The orbital elements obtained from the two pass orbit determination were also tested for satellite re-acquisition and the predicted trajectory is shown in Panel C of Figure 5.4. The in-track and cross-track offset for the 2-pass satellite re-acquisition is shown in Panel D of Figure 5.4.

The observed reduction in cross-track offsets to less than  $0.1^\circ$  (1 km at the HST altitude) between the two methods is analogous to the improvement observed by optical studies (Bennett et al., 2015) that compared prediction accuracy when using a short arc detection and a long arc detection to perform orbit determination. Although the MWA is a wide FOV sensor that is capable of detecting satellite passes that span more than 10s of degrees, the curvature of the pass is not highly constrained due to arc-minute angular resolutions. Hence, using position measurements from multiple passes helps determine the orbital elements more accurately. The two pass orbit determination also resulted in very small uncertainties for the  $mm$  orbital element, as multi-pass observations help tightly constrain the orbital period of the object (which in-turn affects the value of  $\Delta ma$ , as  $mm$  is a derived measure of the orbital period).

## 5.6 Discussion and Future Work

### 5.6.1 SDA Catalog Maintenance using the MWA and Future Improvements

The rapid increase in LEO objects within the last decade demands the development of orbit determination and catalog maintenance capabilities using multiple

SDA sensors, to assist in avoiding cascading collision event scenarios (Kessler et al., 2010). In this work, we demonstrate a self-sustaining catalog maintenance capability using MWA SDA observations, provided we have access to one-off initial orbit guesses for the objects of interest.

To maintain an accurate understanding of our LEO environment, it is important to note that we report our measurement uncertainties in the orbit determination (not a common practice in the current Space Surveillance community). Having errors associated with the orbital elements assists with better conjunction monitoring and associated risk estimates. With further work, we expect that our measurement uncertainties will reduce.

We were able to successfully re-acquire an object in a future orbit using our determined orbital elements. The offset between the predicted pass and the observed pass was found to be reduced when using multi-pass observations to perform orbit determination, compared to a single pass orbit determination. In the future, the accuracy of our orbit prediction can also be improved by incorporating data fusion with other sensors that observe the target near the epoch. Awareness of the errors associated with the instrument is especially important when performing data fusion for joint orbital element estimation. Studies have shown data fusion to be more effective when using 3D measurements (angular position measurements with range measurements) compared to using 2D measurements (angular measurements only) (Bennett et al., 2015), and using range measurements can help de-couple the uncertainties in our orbital element estimates.

#### **5.6.1.1 SDA Sensitivity Dependence on Array Configuration and Hardware Parameters**

We have used the compact configuration of the MWA Phase 2 array, which contains only short baselines, for this work. The angular resolution of our position measurements could be improved by using the Phase 2 extended configuration of the MWA (longest baseline spans approx. 5 km). However, upon testing SDA

observations using the extended configuration, we identified two limiting factors that reduced our sensitivity towards LEO objects, the near-field effect and visibility fringe washing. We document these effects here.

Interferometer theory assumes that the received wave-front from the source of interest is planar, i.e, the emitting/reflecting source to be far away. However, due to the near-field nature of SDA targets, the curvature of the received wave-front can be observed using the longer baselines of the MWA extended configuration. Using the far-field equation obtained from (Zhang et al., 2018) ( $d = 2D^2/\lambda$ , where  $d$  is the distance of the object,  $D$  is the baseline length, and  $\lambda$  is the wavelength of the observation), we find that objects at an altitude of 400 km (e.g ISS) appear in the near-field for baselines longer than approx. 1160 m. Thus, for extended configuration SDA observations, due to the signal not being correlated coherently, we obtain a de-focusing effect that smears the signal over a large patch of the sky.

As we go from the short baselines of the compact configuration used in the current work towards longer baselines of the extended configuration, even before the near-field limitation comes into effect, visibility fringe washing is expected to become significant. The phase of the measured visibility contains information about the source position (assuming a single source) during the correlator time-averaging, and the measured phase changes with time as the source moves (usually due to sky rotation). The time-averaging interval of the correlator is often optimised to avoid spatial smearing of the data due to sky rotation and for existing MWA hardware this is limited to 0.5 s. However, in our SDA observations, LEO objects often have very high angular speeds (e.g ISS moves at approx.  $1^\circ/\text{sec}$  near the zenith), and hence due to rapid changes in the phase of the visibility, the 0.5 s time-averaging results in visibility fringe washing. A simplified form of fringe frequency (time rate of change in visibility phase) for an East-West baseline is given below (adapted from Marr et al. (2015))

$$F_{freq} = 2\pi\omega\frac{b}{\lambda}\cos(\omega\Delta t) \quad (5.2)$$

where  $F_{freq}$  is the fringe frequency,  $\omega$  is the angular speed of the source,  $b$  the projected baseline length,  $\lambda$  the wavelength of the observing frequency and  $\Delta t$  is the correlator integration time. Using Equation 5.2 we see that the phase of the visibility changes by more than  $\pi$  for an object like the ISS for baselines longer than 195 m, with the existing MWA hardware ( $\Delta t = 0.5$ ). With the current ongoing upgrade to MWA Phase 3, the correlator time-averaging can reduce to 0.1 s and this should help increase the number of long baselines that we can use for SDA observations.

### 5.6.1.2 The MWA SDA Capability in the Global Context of SDA Sensors

In this section, we place the MWA passive radar system in the context of existing global SDA sensors. We do this by discussing three aspects of the system: the accuracy of position measurements; goodness of orbit determination and associated errors; and the value added to existing global SDA networks.

With our SDA system we are able to perform angular position measurements with an average uncertainties of 1.1 arc-minutes, which are sufficiently small to support meaningful coordination with much smaller field-of-view optical sensors (such as the ZIMLAT telescope used in [Cordelli et al. \(2019\)](#) [ $7' \times 7'$  FOV] and the OWL-Net SDA sensor used in [Choi et al. \(2018\)](#) [ $1.1^\circ \times 1.1^\circ$  FOV]). Unaided laser ranging systems require a few arc-second accuracy ([Bennett et al., 2015](#)). With the current MWA SDA system, coordinating with laser devices could prove to be a challenging task. The 1.1 arc-minute angular error translates to under 0.5 km positional error at a distance of 1000 km. These typical uncertainties are comparable to the notional  $\sim 1$  km positional errors ([Vallado et al., 2013](#)) of TLEs during the epoch of measurement.

In previous sections we have validated the accuracy of our orbit determination

method by testing for re-acquirability of the target object, as well as by verifying them against the TLE values released by SSN near the epoch of observation. The uncertainties associated with these SSN TLE updates are not publicly available, and hence we place our reported orbital element errors (Table 5.1) in the global context using the HST observation (observation 1165762576 in Table 5.1) as an example. We obtain the historic TLE values for HST for 1000 days and plot the orbital elements as a function of time ( $aop$  and  $e$  shown in Figure 5.5). The SSN reported TLE values change with every entry due to the random errors associated with the sensor system that reports it, as well as due to the systematic drift in the orbital element value with time due to the impact of drag, and orbital manoeuvres performed by the satellite. Since we are only interested in the errors associated with the global SDA systems, we isolate the scatter in the data from the drift by fitting a smooth function to the data<sup>17</sup>. The difference between model and data can be used as an estimate of the errors in the reported values. In Figure 5.5 we show our reported error for  $aop$  and  $e$  with reference to the estimated errors in the TLE updates, and they are very similar in value. Note that in the residual panel for  $e$  in Figure 5.5, the jumps/spikes in the residuals are probably due to manoeuvres performed by the HST, and the random errors that we are interested in are shown in the insert residual panel.

With the growing density of objects in LEO, multi-target tracking capability is preferred for SDA sensors (Jones et al., 2015). The MWA SDA system is not just able to perform simultaneous detections, but also perform SDA observations at all times and is not constrained to observation windows like optical sensors that are confined to twilight. The large FOV of the MWA allows us to perform detections that span 10s of degrees across the sky. Unlike active SDA radars, the operation cost involved is also lower with our system due to the exploitation of non-cooperative terrestrial FM transmitters to perform passive Space Surveillance. Most of the non-coherent SDA work done thus far (including Prabu et al.

---

<sup>17</sup>performed using `scipy.ndimage.gaussian_filter1d`. The filter parameters were optimised by trial and error, until the residual in the fit showed no structure.

(2020b) and Prabu et al. (2020a)), was performed using archived data, meaning the primary science case for the observation was not to perform SDA. Observations designed specifically for SDA, using an optimised and dedicated facility based on the MWA technologies and our techniques, would prove to be even more productive.

### 5.6.2 Importance of FM Reflecting LEO Catalog for Astronomy Observations

The MRO is not just the home to the MWA, but also to other interferometers that operate at FM frequencies, such as the Engineering Development Array (EDA) (Wayth et al., 2017) and the future low-frequency component of the SKA. Maintaining a catalog of LEO objects that are known to reflect FM transmitters can help understand FM band observations performed using these low-frequency radio interferometers. Not all optically "small" objects are "small" objects for low-frequency observations. The RCS of a "small" object can drastically increase by the presence of a broken antenna or a wire, and thus maintaining a catalog of radio-bright LEO objects is not just useful for SDA purposes but is also in the general interest of the radio astronomy community.

The impact of LEO objects on low-frequency observations can also be mitigated using our SDA understanding of the non-coherent system. Based on the knowledge of FM reflecting LEO objects predicted to be within our FOV during an observation (knowledge from maintaining a catalog of FM reflecting LEO objects), we could optimise the observation parameters (if feasible), such as UV-weighting and correlator time-averaging, to emphasise the near-field effect and fringe-washing effect. A catalog of FM reflecting LEO objects can also be used to better understand the expected false positive rates in transient and variability studies, analogous to similar studies at optical wavelengths (Arimatsu et al., 2021; Tingay & Joubert, 2021; Richmond et al., 2020).

## 5.7 Conclusion

In this work we have demonstrated orbit determination capabilities using a wide field-of-view system, the MWA, in non-coherent passive radar mode at FM frequencies. The non-coherent passive radar techniques developed for the MWA (Tingay et al., 2013b; Zhang et al., 2018; Prabu et al., 2020b,a) were used in this work and the detected signals are spatially smeared over several degrees, mainly due to the motion of the satellites during the 2 s difference image timescales.

We demonstrate a method for obtaining satellite position measurements from the data, by understanding the different factors (such as the PSF structure and apparent satellite motion) that contribute to the smearing of the signals, and we tested the method on 20 LEO satellite detections obtained from our previous work (Prabu et al., 2020a).

The angular position measurements from our method were used to perform orbit determination for the objects using a least-squares fit approach, and we report these orbital elements in this paper. The orbital elements were verified against the publicly released TLE values by the Space Surveillance Network (SSN)<sup>18</sup> and were found to be in good agreement. We also tested target re-acquisition using our orbital elements on a pair of consecutive HST passes and found the predicted trajectory and the observed pass to coincide in time and position, to within the measurement uncertainties.

In the future, the angles only position measurements from our non-coherent detection method can be coupled with measurements from other sensors to perform catalog maintenance and conjunction monitoring through data fusion. Due to fitting for the six parameters using measurements in 2D space (RA-DEC), the errors in our orbit determination process were found to be highly coupled, and range measurements (that have three independent Euclidean x,y,z components) can help de-couple these errors and constrain the orbital elements better.

We conclude by placing our developed MWA SDA capability in the global

---

<sup>18</sup>Obtained from [space-track.org](https://space-track.org).

context of SDA sensors, by discussing the accuracy of angular position measurements, the goodness of orbit determination, and the value added to the existing global SDA network by the MWA SDA system . Based on our understanding of MWA's response towards LEO objects, we discuss methods to mitigate the impact of LEO objects on radio-astronomy observations, and how maintaining a catalog of FM reflecting LEO objects can help better understand FM band observations performed from the MRO, home to the MWA and the future low-frequency SKA.



# Chapter 6

## Targeted Searches for Weak Reflected FM Signals using the MWA

### 6.1 Introduction

In Chapter 4, I demonstrated techniques to perform blind detections of LEO objects using MWA observations. Whilst this is a good method for detecting lost/new objects, more sensitive detections of known objects can be performed by using prior information about their orbits. In this chapter, I demonstrate and compare two different techniques that perform targeted searches for reflected signals by using prior information about the apparent trajectory of the satellite, based on its predicted Geocentric Cartesian coordinates.

The first method that I explore in this Chapter is called “shift-stacking”. The shift-stacked target search method uses phase-tracked difference images to perform detections by integrating the signal along the predicted trajectory of the pass. Although shift-stacking has been previously described in the literature to search for new Kuiper belt objects, trans-Neptunian objects ([Bernstein et al., 2004](#)) such as “Planet Nine” ([Rice & Laughlin, 2020](#)), and solar-system

satellites (Burkhart et al., 2016) by trial and error iterations performed in a multi-dimensional parameters space, I adapt this method to perform targeted searches for weak reflected signals in MWA data.

The second targeted search method that is demonstrated in this Chapter is aimed at detecting weak signals by re-focusing the interferometer to the predicted near-field satellite position. Standard interferometer theory assumes the observed source to be in the far-field of the instrument, thus deriving a 2D Fourier relationship between the apparent sky and the measured visibilities (as explained in Chapter 2). However, due to the near-field nature of the LEO objects that we aim to detect, the longer baselines of the MWA see a curved wave-front rather than a planar wave-front. Hence, when imaged (without accounting for the curvature), the satellite signal appears de-focused, resulting in reduced SNR. In this Chapter, I demonstrate a near-field targeted search performed using the MWA and also address its current limitations due to hardware constraints.

This chapter is structured as follows. In Section 6.2 I describe the observations used and the data reduction methods employed. The results of the analysis performed are provided in Section 6.3, followed by a brief discussion. I draw conclusions in Section 6.4.

## 6.2 Data And Methods

### 6.2.1 Shift-Stacking

The shift-stacking method aims to detect satellites by performing a spatially coherent averaging of the satellite signal along its predicted trajectory. An example of shift-stacking for the object PICOSAT-9 (NORAD ID 26930) during the observation 1157400472 is demonstrated in Figure 6.1. The top-left panel shows the predicted trajectory of the object above the visible horizon and the phase-tracked field-of-view (FOV) of an individual shift-stack frame (frame for integration number,  $N = 28$ ). Due to the large FOV of the MWA, the curvature of the satellite

pass is often resolved (i.e, the apparent direction of the streak changes during the pass) and stacking without any correction would result in signal smearing. Hence we rotate the individual frames (using `scipy.ndimage.rotate`<sup>1</sup>) to align the streak in the vertical direction (arbitrarily chosen) prior to stacking. The bottom-left panel of Figure 6.1 shows the rotated shift-stacked difference image (after performing an inverse-noise weighted stacking of  $N$  frames) for a fine frequency channel.

I test the shift-stacking method using the 20 hours of Phase 2 compact configuration (Wayth et al., 2018) observations used in the Chapter 4 blind survey. Re-using the observations in this chapter enable us to compare the performance of the blind detection method and the targeted detection method. The visibilities are calibrated (using the `calibrate` tool developed in Offringa et al. (2016)) and converted to CASA measurement set format (McMullin et al., 2007) as explained in Chapter 4, and the images are created using `WSClean` (Offringa et al., 2014; Offringa & Smirnov, 2017).

All LEO objects that were predicted to pass through the MWA’s primary beam during the observations were identified<sup>2</sup>. For every identified object, we search for the satellite signal at every 40 kHz fine frequency channel using the shift-stacking pipeline<sup>3</sup> (resulting in a stacked image cube). Prior to stacking, the phase centre of each of the individual frames is centred (using the `chgcentre` tool developed by Andre Offringa) at the predicted location of the object during the epoch, thus enabling spatially coherent stacking of the faint satellite signal along the satellite trajectory.

All  $6\sigma$  events that appear as a streak signal are identified from the obtained shift-stacked image cube. We vet the events to obtain a primary list of candidate detections (note that we sort them further to remove false positives in Section

---

<sup>1</sup><https://docs.scipy.org/doc/scipy/reference/generated/scipy.ndimage.rotate.html>

<sup>2</sup>by performing an API query using `spacetracktool.SpaceTrackClient.tle_publish_query` for the epoch. <https://pypi.org/project/spacetracktool/>

<sup>3</sup> <https://github.com/StevePrabu/Space-Fest/blob/master/bin/phaseTrack.sh>

6.3.1) using the criteria that the events must appear as a spatially coherent  $6\sigma$  streak in more than one fine frequency channel (this helps get rid of aliased side-lobes of other bright events that may spatially coincide with the object of interest and also is the selection criteria used during the blind survey). The list of 164 detected candidates are further investigated in Section 6.3.1.

## 6.2.2 Near-field re-focusing

The wavefronts of the reflected FM signals from LEO objects appear curved when observed using the long MWA baselines, resulting in de-focused (reduced SNR) signals. This apparent deviation ( $\Phi$ ) from a planar wave-front as seen by a “long” baseline is shown in Figure 6.2. The Phase 2 extended array observation 1290483224 is used in this Section, as the compact configuration observations could not be used, as most of its baselines are under 200 m in length (LEO objects appear in the far-field). The target observation used was calibrated using amplitude and phase solutions obtained for the observation 1290513616 (calibrated using infield GLEAM sources (Hurley-Walker et al., 2017), followed by the application of self-calibration). The two observations were about 8 hours apart and MWA calibration solutions are often valid within a day.

Prior information of the satellite’s and MWA tile’s Geocentric Cartesian coordinates (e.g,  $X_{sat}$ ,  $Y_{sat}$ ,  $Z_{sat}$  and  $X_{tile1}$ ,  $Y_{tile1}$ ,  $Z_{tile1}$ ) are used to calculate the actual deviation/delay from a planar wave-front ( $\phi$  in Figure 6.2) as seen by each baseline (calculated independently for every time-step within the observation). The calculated delay  $\phi$  is applied as a phase offset to re-focus the array to the desired near-field location. For a baseline between  $tile_1$  and  $tile_2$ ,  $\phi_{1-2}$  is calculated using Equation 6.1

$$\begin{aligned}
 R_1 &= \sqrt{(X_{sat} - X_{tile1})^2 + (Y_{sat} - Y_{tile1})^2 + (Z_{sat} - Z_{tile1})^2} \\
 R_2 &= \sqrt{(X_{sat} - X_{tile2})^2 + (Y_{sat} - Y_{tile2})^2 + (Z_{sat} - Z_{tile2})^2} \\
 \phi_{1-2} &= (R_1 - R_2) - w_{1-2}
 \end{aligned} \tag{6.1}$$

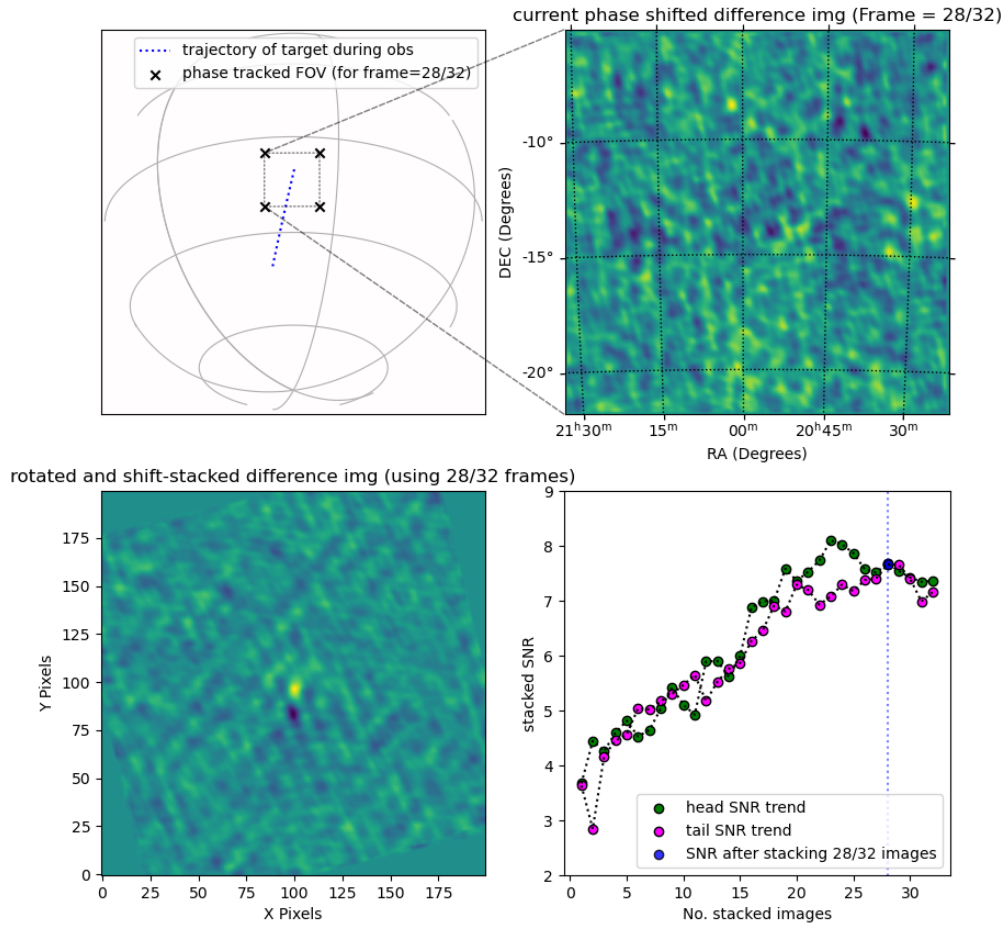


Figure 6.1: Demonstration of the targeted search performed using the shift-stacking method. The top left-panel is the entire horizon visible to the MWA during the observation. The predicted trajectory of the satellite (blue dotted line) and the phase tracked FOV of the satellite (for frame  $N = 28$ ) is shown using black crosses. The insert panel (top-right) shows the phase-tracked fine channel difference image for the considered time-step/frame. The bottom-left panel is the rotated shift-stacked fine channel difference image of the satellite signal after stacking  $N$  frames (in this case  $N = 28$ ). An animation of this figure is available at <https://www.youtube.com/watch?v=blm2dIg7TM8>. The bottom-right panel shows the SNR of the satellite signal increasing with the number of stacked frames.

where  $R_1(R_2)$  is the distance in  $m$  between the object and  $tile_1(tile_2)$ .  $w_{1-2}$  is the w-term associated with a planar wave-front as seen by the baseline. The calculated delay is applied to the measured visibility as a complex phase offset using the Equation 6.2 (adapted from Marr et al. (2015) ),

$$\Delta phase_{1-2} = \exp^{i2\pi \frac{\phi_{1-2}}{\lambda}}, \quad (6.2)$$

where  $\lambda$  is the wavelength of the fine frequency channel. The correction is applied to the measurement set prior to imaging using our developed Python tool LEOVision<sup>4</sup>

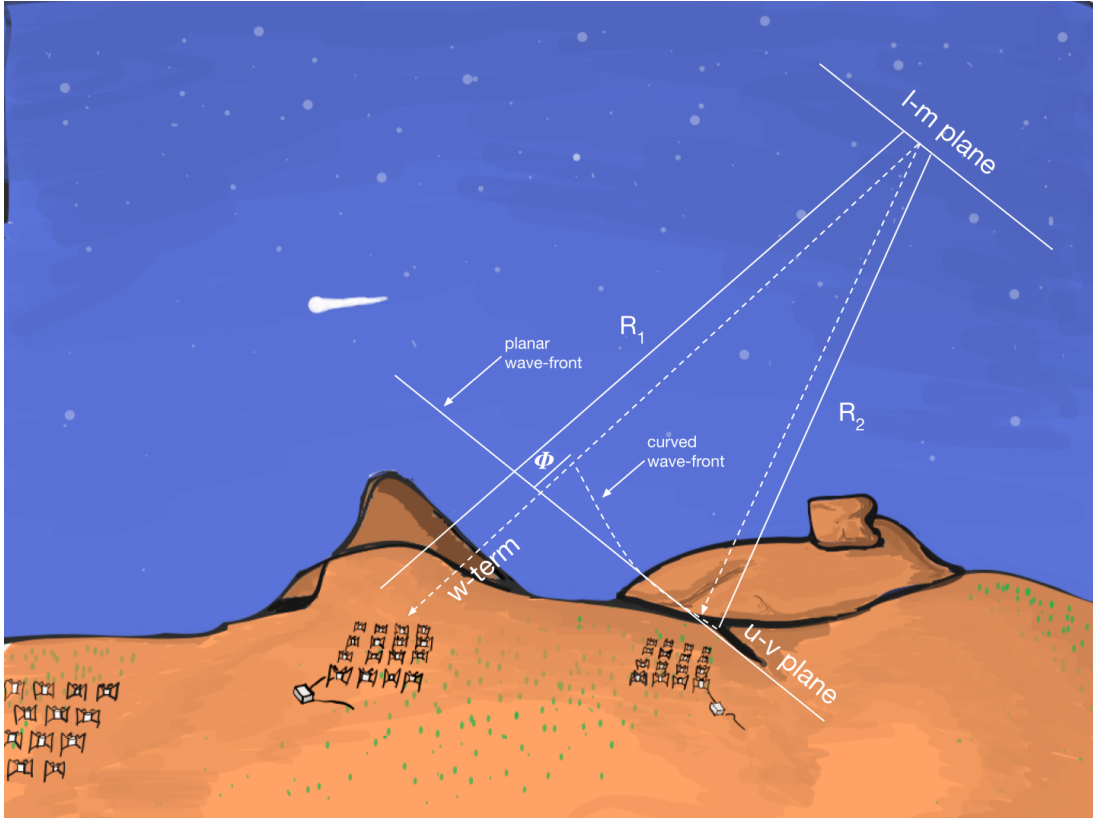


Figure 6.2: The near-field curvature as seen by a baseline-pair.  $\Phi$  is the delay due to the curved wave-front and,  $R_i$  is the distance between the object and  $tile_i$ .

<sup>4</sup><https://github.com/StevePrabu/LEOVision>

## 6.3 Results and Discussion

### 6.3.1 Shift-Stacking Candidates

Through manual inspection of the 164 candidates obtained from the shift-stack search performed in Section 6.2.1, we identify two different types of events, namely, flaring events and steady reflection events. Flaring events often have a single frame with a very high SNR signal and stacking reduced the SNR of the event (due to lack of spatially coherent signal in other frames). An example of a flaring event is shown in Figure 6.3. On the contrary, the SNR of steady reflection events only increased with stacking and an example is shown in the bottom-right panel of Figure 6.1.

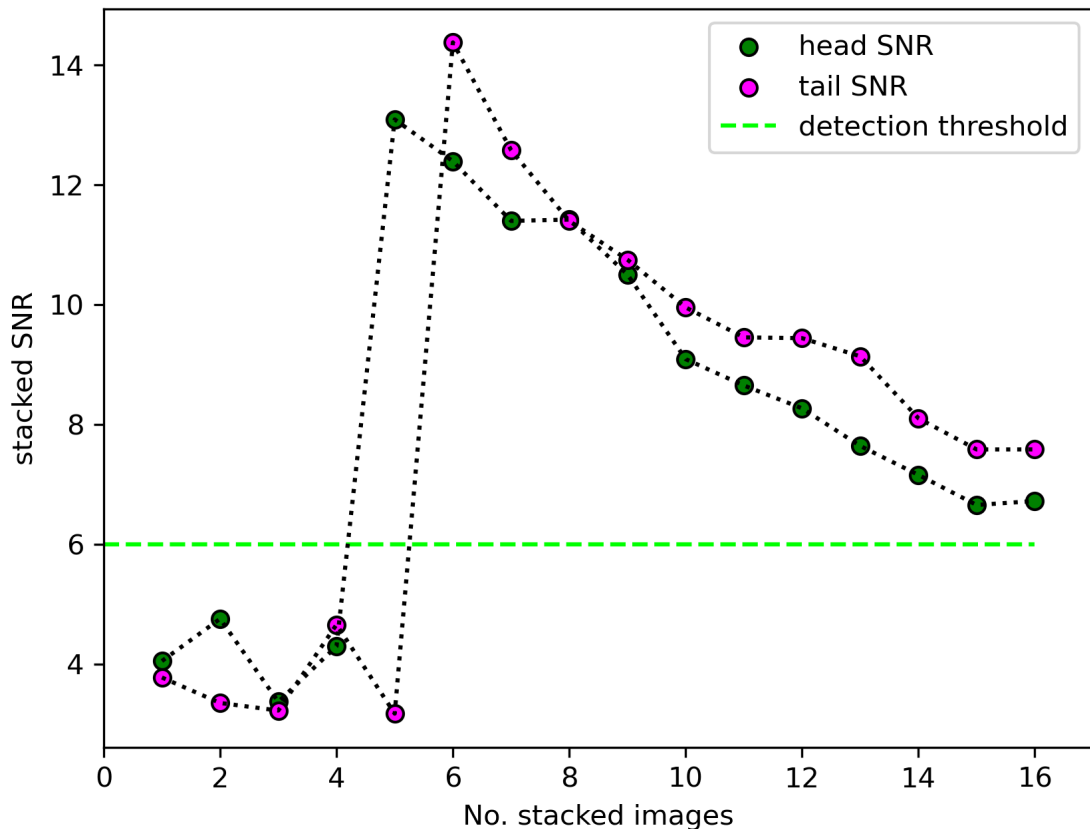


Figure 6.3: An example of a flaring event detected using the shift-stack pipeline.

The two different populations of candidates are further analysed based on

their offset from the phase centre (predicted location of the object using TLE) of the shift-stacked image, and the frequency channel they are detected in. While the frequency channel investigation would help determine if the event is due to an FM reflection from real objects or bad difference imaging (imperfect background source subtraction due to time varying sky signal or instrument response), the apparent offset should help determine if the detected signals are likely to be from the object of interest (LEO objects).

Figure 6.4 shows the centroid offset for all the flaring and steady reflection events, and we see a very different behaviour between the two populations. The majority of the steady reflection events appear within a degree from the phase centre (expected location of the object), while the flaring events have an almost uniform distribution of offsets before tapering off near the edge of the shift-stacked FOV. This tapering is due to image rotation resulting in many blank pixels near the edge as seen in the bottom-left panel of Figure 6.1. As most of the steady reflection events are closer to the predicted locations than the flaring events, they are more likely to be from the target of interest, and hence we classify them as our final list of candidate detections. We detect almost all the objects detected during the blind survey in Chapter 4 (except a few events where a few noisy frames reduced the stacked SNR of the signal under the detection threshold used in Section 6.2.1) and many more new signals not previously detected. Using shift-stacking, we improve the total (Chapter 4 and Chapter 6) number of detection candidates from our 20 hours of observation by 75%<sup>5</sup>. The list of new detection candidates (excluding the events already detected during the blind survey in Chapter 4) are listed in Table 6.2. Note that for the MWA, primary beam correction is applied in the image domain, and creating the corresponding phase tracked primary beam models for every time-step is a very computationally intensive task as the individual shift-stack frames were not primary beam corrected. Hence, Table 6.2

---

<sup>5</sup>During the blind survey 73 events were detected inside the primary beam (along with 7 detections of large objects outside the primary beam). Using shift-stack search, we obtain 55 new events inside the primary beam.



provides only the apparent peak flux density of the events.

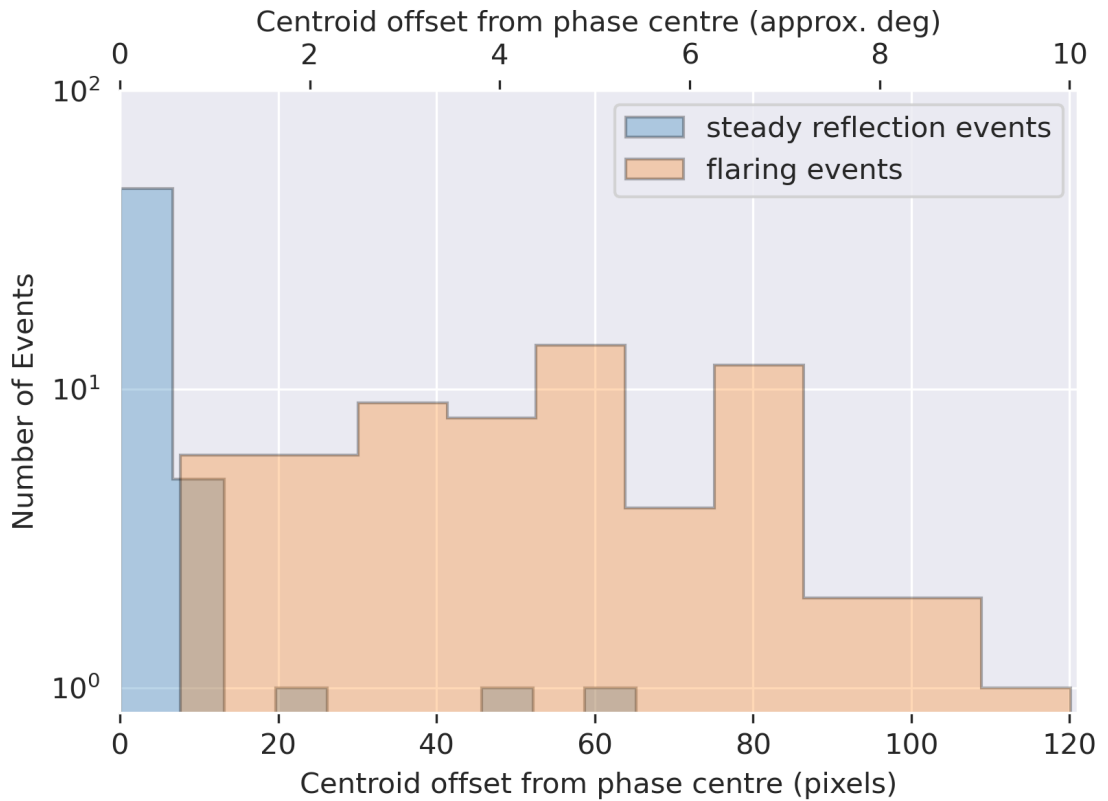


Figure 6.4: The apparent centroid offset distribution for steady reflection and flaring events. Most of the steady reflection events are within a degree from the predicted location, while the flaring events have almost a uniform distribution within the FOV and tapers off towards the edge due to rotating the frames.

The frequency of the observations used in the shift-stack analysis span 72.335–103.015 MHz, while the FM band only overlaps with the second half of the observation band (i.e, above 88 MHz). Figure 6.5 shows the frequency distribution of all the detected steady reflection and flaring events. From Figure 6.5 we see that all the steady reflection events are confined within the FM band (as expected from FM reflecting satellite) and most of the flaring events are also confined within the FM band. Hence, it is very likely that the flaring events, though not the targeted satellite signals, are likely to be real reflection events (and not due to noise). Many (8.5 hours) of the observations used coincided with the Geminids meteor shower and it is possible that many of the flaring events are associated

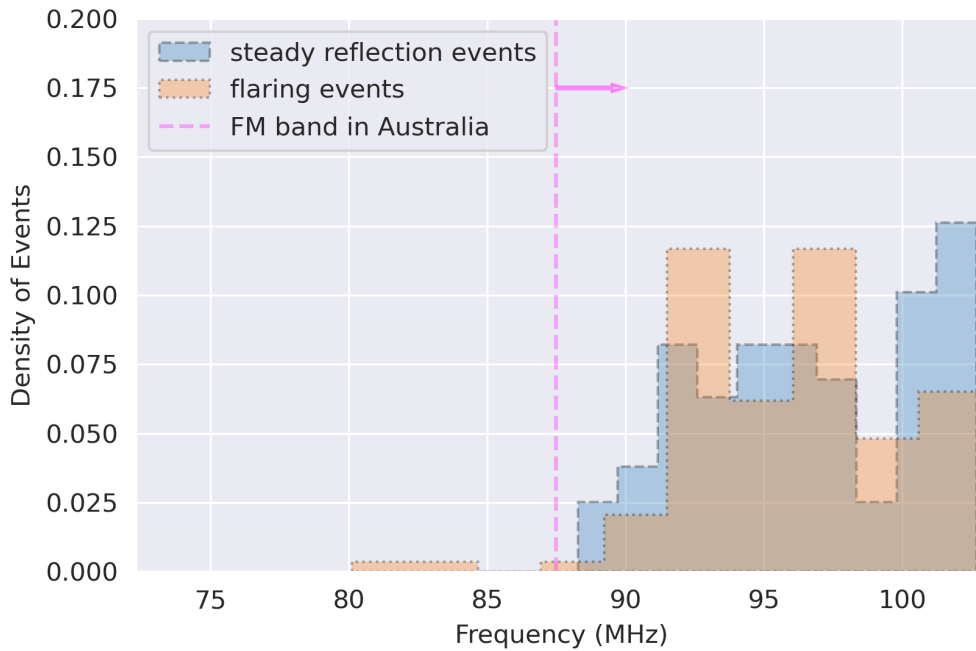


Figure 6.5: The density distribution of channels in which the flaring and steady reflection events were detected. The two brightest channels at which the event was detected spatially coherent (channels identified during the candidate vetting process in Section 6.2.1) was used to create the plot. We see that all the steady reflection events are confined with-in the FM band (as expected), and most of the flaring events were also detected within the FM band, implying that many of the flaring events could be FM reflections from meteors.

with FM reflections from ionised meteor trails. The occurrence of these FM reflecting flaring events are consistent with a recent study of the RFI environment at the MRO by [Tingay et al. \(2020\)](#).

The final list of new detection candidates (from Table 6.2) from the shift-stack targeted search is shown in the RCS vs range parameter space in Figure 6.6. The background image is the blind survey detection summary figure from chapter 4, and the new detections are annotated using white circle markers. The histograms along the right and lower axes of Figure 6.6 show the distribution of all the search trials performed using shift-stack in this chapter (blue) along with total number of detections (blind survey and shift-stack in orange) obtained inside

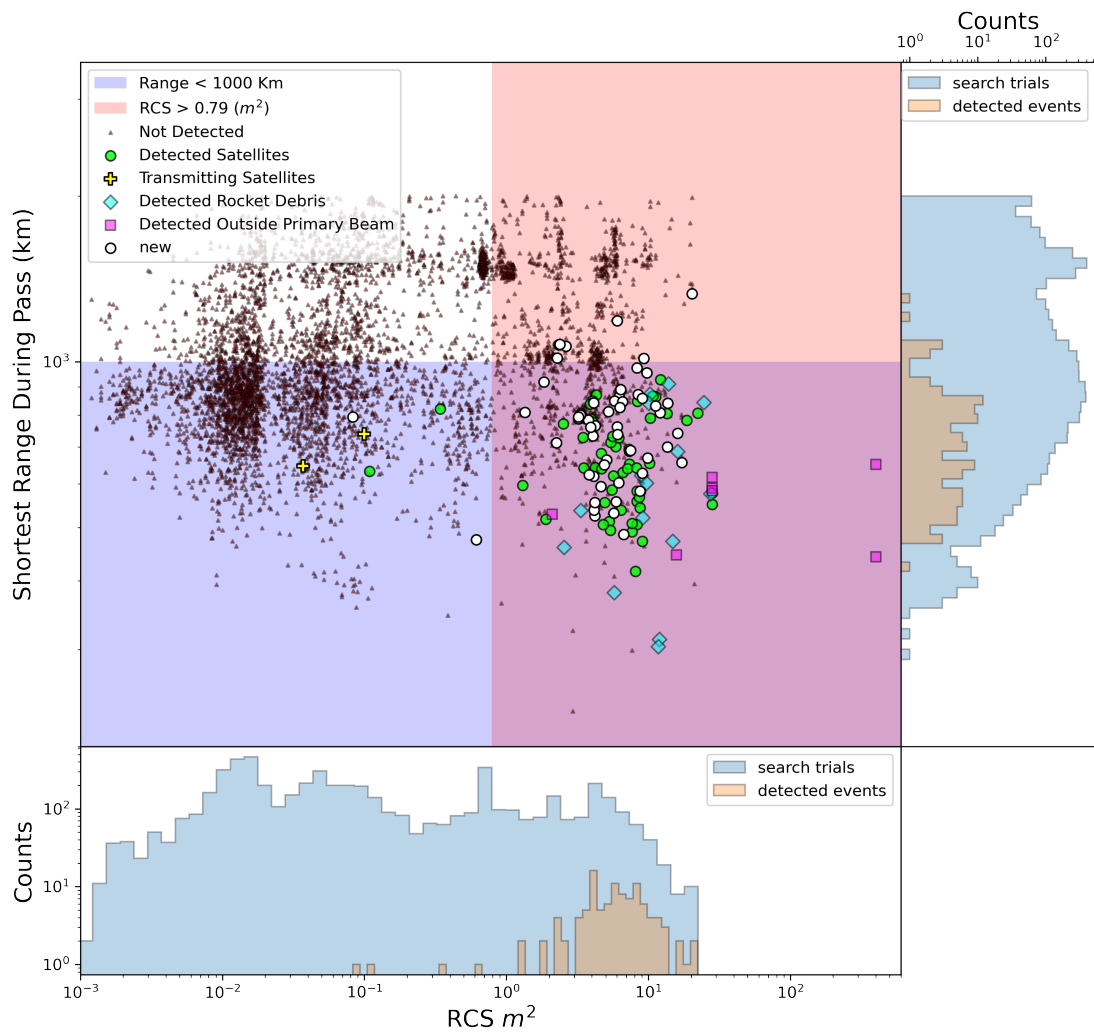


Figure 6.6: The new candidate detections in range vs RCS parameter space using white circle markers. The background image is the detection summary of the blind survey performed in Chapter 4.

the primary beam during the observations used. The blue histogram shows the parameter space probed during the search, and the orange is what was detected (completeness of the technique) using the methods developed in this thesis.

Table 6.1: All the new events detected by the shift-stacking targeted search. The last column mentions the apparent peak flux density in the shift-stacked image.

Observation ID	Name	Norad ID	RCS $m^2$	Shortest Range km	Apparent Peak Flux Density (Jy/beam)
1165782736	DELTA 2 R/B(1)	24809	9.88	668	5.41
1165782496	DELTA 2 R/B(1)	23640	9.75	954	5.65
1165776496	CZ-2D R/B	36597	8.72	582	6.09
1165776256	SL-24 R/B	31123	5.23	811	7.85
1165775896	FENGYUN 3B	37214	6.21	863	7.43
1165771576	SUOMI NPP	37849	5.78	848	8.78
1165770376	IRIDIUM 43	25039	3.20	788	5.18
1165770256	ATLAS AGENA D R/B	2144	6.04	761	5.32
1165768576	ASTRO-H (HITOMI)	41337	6.16	603	7.11
1165767376	OCEANSAT-2	35931	4.06	732	6.14
1165766296	SL-16 R/B	24298	8.49	871	6.79
1165765936	OA0 1	2142	12.1	807	4.33
1165765816	PSLV R/B	25759	6.06	737	5.20
1165763536	DELTA 2 DEB [DPAF]	29110	5.07	662	4.61
1165763536	KAZEOSAT 1	39731	4.22	765	3.66

Table 6.2: ...continued from previous page.

Observation IDs	Name	Norad ID	RCS $m^2$	Shortest Range km	Apparent Peak Flux Density (Jy/beam)
1165760896	COSMOS 2486	39177	16.0	741	2.18
1165759696	KORONAS-FOTON	33504	4.18	524	6.90
1165757896	KMS 4	41332	0.61	475	3.29
1165757056	CZ-2C DEB	40288	0.08	793	2.86
1165753576	CAMEO and DELTA 1 R/B	11081	8.30	975	6.23
1160505712	IRIDIUM 7	24793	3.32	799	5.72
1160505112	IRIDIUM 6	24794	3.23	794	8.27
1160504872	SL-24 DEB	33318	4.64	593	6.12
1160504272	SL-16 R/B	17974	9.05	858	10.0
1160503672	IRS-1D	24971	3.91	760	9.29
1160502232	FORTE	24920	1.35	809	6.57
1160500192	SL-14 R/B	10974	4.12	619	4.62
1160499712	SUZAKU (ASTRO-EII)	28773	4.15	538	7.94
1160499352	INTERCOSMOS 25	21819	7.32	688	8.92
1160498872	CZ-2C R/B	40262	7.47	690	10.5

Table 6.2: ...continued from previous page.

Observation IDs	Name	Norad ID	RCS $m^2$	Shortest Range km	Apparent Peak Flux Density (Jy/beam)
1160489992	PSLV R/B	41620	6.71	485	9.66
1160489152	METOP-B	38771	13.6	840	6.87
1160489032	H-2A R/B	38341	17.2	655	6.57
1160483992	COSMOS 1833	17589	4.11	841	7.97
1160482912	FENGYUN 3A	32958	6.58	845	9.37
1160479912	COSMOS 1300	12785	5.69	531	16.2
1157489632	SL-24 R/B	31699	5.92	557	21.3
1157469232	KORONAS-FOTON	33504	4.18	554	17.9
1157459032	ALOS (DAICHI)	28931	13.6	700	33.5
1157406472	SL-14 R/B	14820	3.82	623	4.42
1157406472	TSX-5	26374	1.84	919	3.42
1157401672	SL-3 R/B	7275	6.37	889	6.34
1157398072	BREEZE-M DEB [TANK]	36594	6.29	825	4.05
1157384272	SJ-11-07	40261	2.26	712	8.18
1157378272	METOP-A	29499	11.2	830	8.86
1165769776	COSMOS 860	9486	2.28	1015	4.71

Table 6.2: ...continued from previous page.

Observation IDs	Name	Norad ID	RCS $m^2$	Shortest Range km	Apparent Peak Flux Density (Jy/beam)
1160496712	SL-12 R/B(2)	27473	20.3	1329	3.73
1160495392	YAOGAN 25A	40338	2.33	1074	5.19
1160495392	YAOGAN 25C	40340	2.63	1066	6.21
1160495392	YAOGAN 25B	40339	2.39	1075	3.09
1157484832	CZ-3 R/B	20474	9.30	1014	26.3
1165762936	CBERS 4	40336	3.78	783	6.94
1160498512	SL-8 R/B	11170	6.04	1187	5.08
1160491312	SL-24 DEB	35689	4.88	649	8.64
1160492992	DELTA 1 R/B(1)	10793	9.06	627	10.8

### 6.3.2 Near-field Results

The ISS was found to be within the primary beam of the extended array observation used, and hence is used as the object of interest in this section. The motivation for using the ISS is two-fold; first it is a bright object which gives consistent reflections at multiple frequencies, secondly it is a particularly low orbit object and thus is in the near-field more often than other large objects. For one of the time-steps that the ISS was detected, the MWA’s baselines were divided into short and long baselines (using 826 m as the cut-off for the baseline separation, as determined by the near-field equation  $d = 2D^2/\lambda$  provided in Chapter 3), and their corresponding fine-channel difference images are shown in the top panels of Figure 6.7. We see that the streak signal is detected over  $6\sigma$  in the short-baseline image while it is not detected using the long-baselines.

The near-field visibility phase correction for the appropriate time-step is applied using the `LEOVision Python` tool. The phase corrected difference images for the short and the long baselines are shown in the bottom panels of Figure 6.7. While the SNR of the short baseline image has increased, the previously undetected streak signal in the long baseline image now begins to appear. This demonstrates the MWA’s capability to focus on the desired near-field satellite position to perform more sensitive SDA detections.

Although the streak signal was recovered in the long-baseline difference image after applying the phase correction, the streak SNR in the long-baseline difference image is much lower than the short-baseline SNR, contrary to our expectation. When the baseline cut-off was applied, 1365 baselines were classified as short baselines and the remaining 6636 baselines were classified as long baselines (note only 8001 baselines were available after flagging). Because the long-baseline image has more collecting area (number of baselines), we expect it to detect the streak at a higher SNR than the short-baselines image, contrary to what we observe in Figure 6.7. We attribute this effect to fringe-washing of the satellite signals in the long-baselines. As explained in Chapter 2, the phase of the measured com-



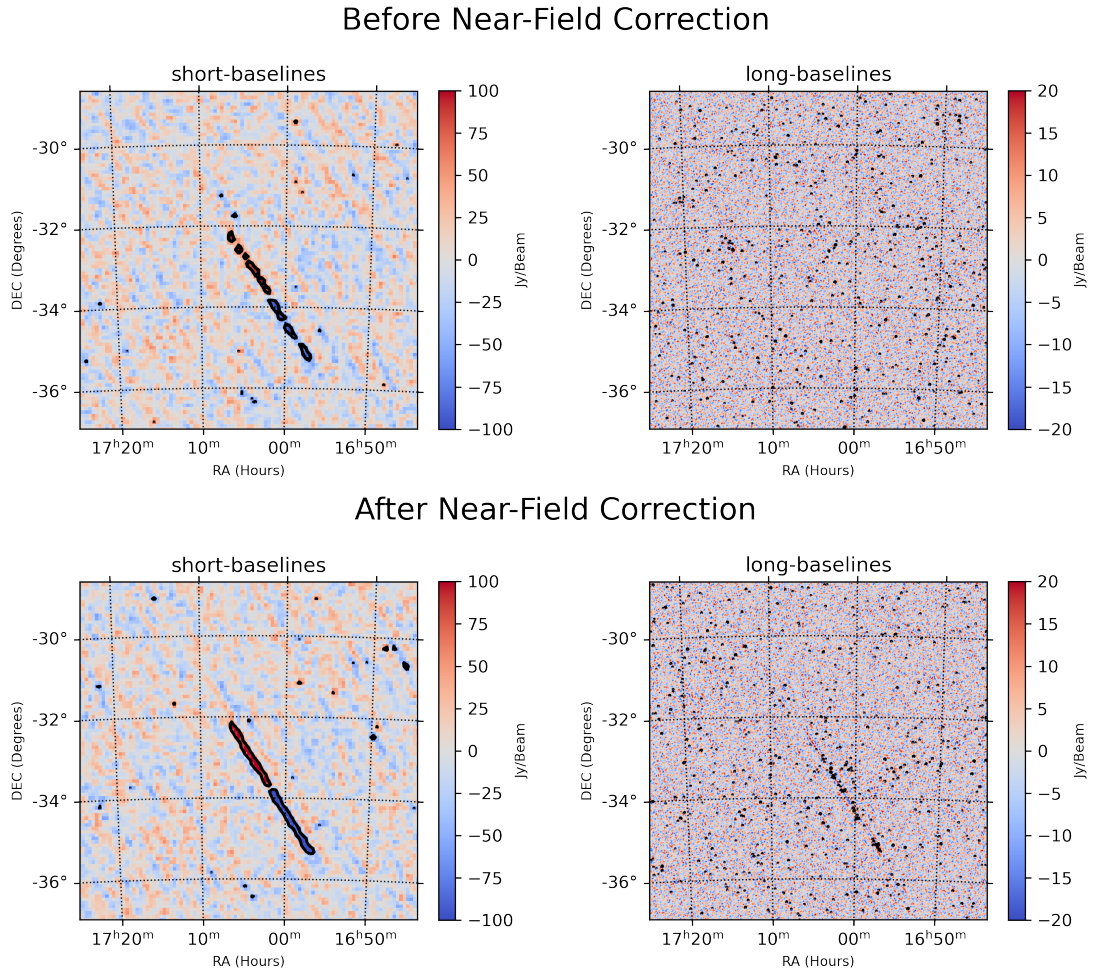


Figure 6.7: Demonstration of the near-field imaging capability with the MWA. The top two panels are the short-baseline and long-baseline difference image of a single fine channel at a given time-step, prior to applying the required phase correction. The long/short baseline cut-off used is 826 m, as determined by the near-field equation.

plex visibility contains information about the source position with respect to the phase-centre. The visibility averaging duration (limited to 0.5 s with the current MWA hardware) of the correlator is often optimised to minimise fringe-washing of celestial sources due to sidereal rotation ( $0.25^\circ/\text{minute}$ ). However, the phase of the fast moving LEO objects (e.g. ISS moves at approx.  $60^\circ/\text{minute}$  near the zenith) considered in this work change rapidly within the time-averaging duration, thus resulting in loss of coherence (fringe-washing) when observed using the

long baselines. The baseline lengths affected by fringe-washing when observing an object at an altitude  $alt$  is given by Equation 6.3 (the equation is derived in Appendix A.3)

$$\Delta\Phi \approx 2\pi \frac{b}{\lambda \times alt} \sqrt{\frac{GM_{earth}}{R_{earth} + alt}} \Delta t \quad (6.3)$$

where  $\Delta\Phi$  is the change in visibility phase,  $\Delta t$  is the visibility averaging duration,  $b$  baseline length,  $\lambda$  wavelength in  $m$ ,  $G$  is the gravitation constant,  $M_{earth}$  is the mass of Earth, and  $R_{earth}$  is the radius of Earth. Using Equation 6.3, we show the baselines affected by fringe-washing effect (source phase change of  $\pi$ ) in the top panel of Figure 6.8 (for 2.0 s, 0.5 s, and 0.1 s visibility averaging). Note that the figure also shows the baseline lengths affected by near-field effect (independent of the visibility averaging duration).

The bottom panel of Figure 6.8 also shows the baseline distribution of the MWA Phase 2 extended array and the compact array. As we go from short baselines towards the longer baselines, from Figure 6.8, we see that the fringe-washing comes into effect much before the near-field de-focusing effect (plotted using equation  $d = 2D^2/\lambda$  provided in Chapter 3) for the 2 s time-averaging used. Hence, in Figure 6.7 we cannot recover the streak signal with the longer baseline difference image due to fringe-washing. However, with the Phase 3 MWA, we will be able to sample visibilities with 0.1 s time-averaging and more sensitive SDA observations with longer baselines should be possible. The number of baselines not fringe-washed<sup>6</sup> as a function of altitude is shown in Figure 6.9. We see that the sensitivity of extended array with the new Phase 3 correlator (0.1 s averaging) is more sensitive (as more baselines are not fringe-washed) than the current hex configuration blind survey performed in Chapter 4 (compact configuration with 2 s averaging). The Phase 3 MWA will also eventually have 256 tiles (as compared

---

<sup>6</sup>since we ignore the baseline orientation with respect to the direction of satellite pass, the number of baselines not fringe-washed in the plot can be treated as the worst case scenario. In reality, the only the baselines with a component parallel to the satellite pass will be fringe washed and hence the figure can be used as an upper limit.

to 128 tiles in Phase 2), and hence the increase in interferometer collecting area should help detect fainter events (either due to small RCS or very large altitudes).

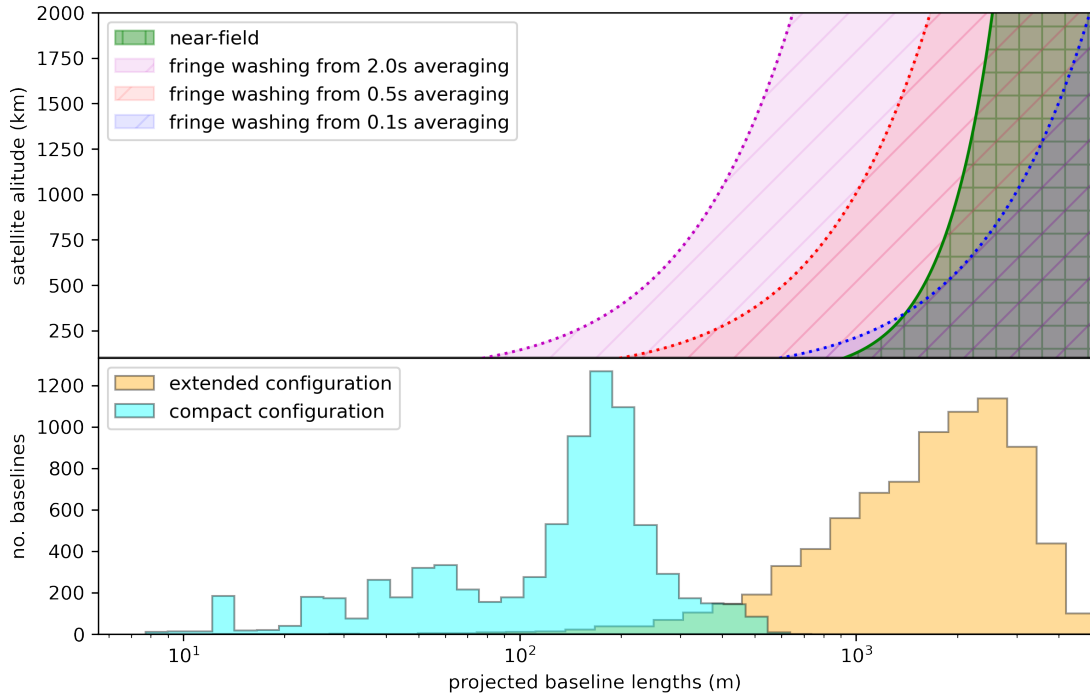


Figure 6.8: Top panel of figure shows the baselines affected by near-field effect and fringe-washing (phase change of  $\pi$ ) as a function of satellite altitude. The bottom panel of the figure shows the baseline length distribution for the phase 2 compact and extended configuration.

## 6.4 Conclusion

In this Chapter, I have developed and demonstrated two different methods to perform targeted searches for reflected LEO satellite signals in MWA FM band observations. The first targeted search method is called shift-stacking. The method aims to increase the SNR of weak signals by averaging the signal along the predicted trajectory, through coherent stacking. I test the method for all the objects that drift through the MWA's primary beam during the 20 hours of observation used during the blind survey (Chapter 4). The shift-stacking targeted search

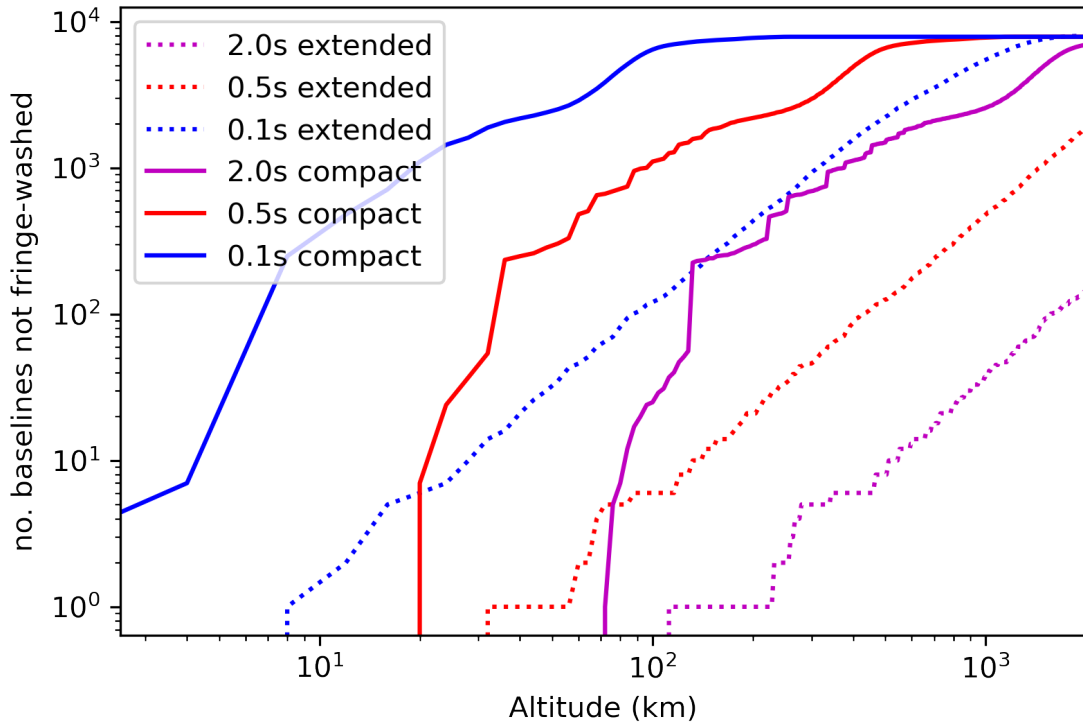


Figure 6.9: Figure shows the number of baselines not fringe-washed for the compact and extended configuration as a function of visibility averaging duration.

resulted in 55 new detections that were previously not detected by our blind detection pipeline, demonstrating that the shift-stacking method is able to probe a weaker population of signals as it uses prior information about the object’s pass to perform signal stacking.

The second targeted search method aims at the detection of weak signals by re-focusing the interferometer to the desired near-field satellite location. It does so by calculating the apparent delay as seen by a baseline and converting it into a visibility phase correction. This method was proved to work effectively using an extended array observation of the ISS. The previously undetected ISS FM reflection signal in the long-baseline difference image of the observation was recovered after applying the required near-field phase correction. However, the recovered signal was weaker than expected, due to visibility fringe-washing. The phase of the ISS signal changed rapidly (during the correlator integration time

of 0.5 s) resulting in de-correlation of the signal. However, with the ongoing upgrade of MWA to Phase 3, we should be able to perform more sensitive near-field detections due to being able to sample the apparent sky with 0.1 s averaging (reduces fringe-washing).



# Chapter 7

## Conclusion

This thesis develops and test methods to use the Murchison Widefield Array (MWA) to contribute towards the global Space Domain Awareness (SDA) effort, primarily towards the observation and SDA data acquisition. The MWA is used as a non-coherent passive radar to perform space surveillance and search for satellite reflections of terrestrial FM transmissions. In summary, the thesis has shown that the MWA could be used to provided valuable SDA data.

The rapidly increasing number of human made objects in Earth orbit has raised concerns among the observational astronomy community about the impact of these reflecting satellites across optical, infrared, and radio wavelengths. Hence, this thesis also briefly discuss the impact of FM reflecting satellites on FM band observations performed from the Murchison Radio-astronomy Observatory (home to the MWA and the future low-frequency Square Kilometre Array) and potential ways to mitigate these impacts.

The research done in exploring MWA utilisation as an SDA sensor has been laid out as four research projects in this thesis. Each one of these projects explores a different aspect of the MWA SDA system and assesses how it can be used to contribute to LEO space surveillance. The four projects are summarised below.

## 7.1 Project 1: The Dynamic Spectrum Analysis

This study used the wide-band observational capability of the MWA to perform high time and frequency inspection of the detected satellite signals (reflections). The concept of Dynamic Signal to Noise Ratio Spectrum (DSNRS) was developed during the study to isolate the satellite signals from direct path reception from transmitters, due to atmospheric ducting. Using DSNRS, the different FM frequencies reflected by large satellites such as ISS and ALOS were identified. The work also detected FM reflections from a defunct satellite called Alouette, a 1 m diameter spherical satellite at 2200 km altitude, which is the most distant Earth orbiting object detected in this thesis.

The work also identified spurious satellite broadband transmissions from two CubeSats, namely, Ukube-1 and Duchifat-1, that polluted the low frequency sky. The Effective Isotropic Radiation Power (EIRP) from these CubeSats was measured to be 256 mW, compared to  $11 \mu\text{W}$  for FM reflecting satellites such as Alouette. The study also found other FM reflecting events within the observations, later found to be meteor trails and aircraft, which warranted further investigation.

The work identifies in-track offset between the actual satellite location and the predicted TLE location, thus demonstrating the MWA's ability to detect objects in LEO and potentially contribute to SDA. The developed DSNRS technique can be used to monitor and report spurious satellite transmissions that contaminate the radio-astronomy observations performed from the MRO.

## 7.2 Project 2: A LEO Blind Survey

During this project, a blind detection pipeline was developed, to autonomously detect FM reflecting satellite signals in MWA data. As part of the pipeline, a Python source-finding software was developed, `RFISeeker`, that performed detections of transient narrow-band signals by creating difference images at every fine



frequency channel and at 2 s cadence. The pipeline was used to perform a blind survey of the LEO environment, using archived MWA Phase 2 compact configuration observations. The survey detected over 70 unique LEO objects over multiple passes in under 20 hours of observation. Objects as small as  $0.03\text{ m}^2$  radar cross-section and as far as 977 km were detected during the blind survey. Additionally, the pipeline also detected FM reflections from ionised meteor trails and aircraft during the survey. For bright events (such as aircraft), parallax ranging methods were demonstrated, by splitting the array into sub-arrays that observed the source with an angular offset.

The bright time-varying signals detected during the blind survey are often considered as Radio Frequency Interference (RFI) in the context of astronomical observations. Hence the detected events during the blind survey were used to perform a brief characterisation of the different FM band RFI seen by the MWA. The study helped realise that most of these events go un-flagged when using the default MWA flagging strategy, and more care must be taken in order to mitigate the impact of satellite signals on FM band observations performed from the MRO.

### **7.3 Project 3 : Catalogue Maintenance**

This project developed methods to extract angular position measurements of satellite passes from MWA observations. Using the measurements, the study demonstrates orbit determination and catalogue maintenance of LEO objects using a set of 32 satellite passes detected during the blind survey. The estimated orbital elements were compared with the publicly published TLE updates for the objects near the epoch, and were found to be in good agreement. The orbit determination method also kept track of the errors associated with the measurements, and demonstrated re-acquisition of satellites by propagating the errors into angular position uncertainties of the object at a future epoch/pass. The estimated positional errors were also found to be less than the widely accepted 1 km positional uncertainty in the publicly published TLEs.

The study found that the MWA SDA system is limited by the near-field effect and fringe-washing when using long baselines with the default range of integration times using the current MWA correlator. The study also briefly discusses ways to mitigate the impact of satellite signals on radio-astronomy observations by intensifying the near-field and fringe-washing effects. The importance of maintaining a catalogue of FM reflecting LEO objects is also discussed - how it can benefit not just the SDA effort but also the radio astronomy community. Maintaining a catalog of FM reflecting satellites can help better understand FM band observations performed from the MRO. Not all optically “small” objects are “small” in radio-frequencies, as the RCS of the object can drastically increase by the presence of wires and antennas on the object. Hence, maintaining a catalog of FM reflecting LEO objects can also be used to better understand false positives in transient searches performed from the MRO.

## **7.4 Project 4 : Targeted Search for Faint Signals**

The final project of this thesis was aimed at recovering faint satellite signals from MWA observations. The project developed and tested two different approaches to detect faint signals, namely, shift-stacking and near-field imaging. The shift-stacking method stacks phase-tracked images of the satellites pass and performs detections through coherent averaging of the faint satellite signal. The method was used to search for all LEO objects that passed within the MWA’s primary beam during the 20 hours of observation used during the blind survey. The shift-stack search almost doubled the total number of satellite detections within the observations used.

Near-field imaging aims to increase the SNR of the signal detection by focusing the array to the desired near-field satellite location. By default, the MWA is focused at infinity to observe far-field astronomical sources. However, due to

the near-field nature of the satellite signals, when imaging satellite signals without any correction, we obtain a de-focused image (reduced SNR) of the satellite signal. Hence, the near-field imaging method focuses the array to the satellite's location by applying a frequency dependent phase correction to the measured visibilities. The method was tested successfully on an MWA Phase 2 extended array observation of the ISS. However, the maximum possible SNR (associated with the total collecting area of the MWA) of the event was not achieved due to fringe-washing of the satellite signals in the long-baseline measurements.

The work also briefly expands on using fringe-washing to mitigate the impact of satellite signals on astronomy observations. It also identifies the baselines affected by fringe-washing as a function of satellite altitude (for a given correlator integration time), which helps determine the preferred uv-weighting that minimises the impact of satellite signals on continuum images made for radio astronomy studies.

## 7.5 Closing Remarks and Future Work

In summary, this thesis has shown the MWA to be a novel instrument for performing LEO space surveillance. The methods developed demonstrate the following capabilities using the MWA. The MWA:

- can detect LEO objects (whose dimensions<sup>1</sup> are comparable to FM wavelengths) through their reflection of terrestrial FM transmissions;
- can identify and monitor spurious out of band transmissions from satellites;
- can perform blind detections of known LEO satellites ;
- can detect lost or uncatalogued objects in LEO ;
- can carry out preliminary catalogue maintenance of LEO objects;

---

<sup>1</sup>debris of radius greater than 0.5 m

- can conduct re-acquisition of LEO objects over consecutive passes; and
- can detect faint satellite signals by performing targeted searches that use prior information about their orbits.

In the future, the near-field phase correction software developed can be modified to determine the 3D location of the target by iterative maximisation of the satellite signal by varying its predicted location (the SNR of the signal is maximum when the predicted near-field location matches with its true position). This method would allow us to perform range measurements of LEO objects by exploiting the curvature of its near-field wave-front. All the techniques demonstrated in this thesis (along with the near-field ranging method mentioned above), could be combined into a single automated pipeline, to demonstrate a complete MWA SDA system, that is capable of contributing to the Australian/global SDA effort with wide field of view and 24/7 operational capability.

# Appendices



# Appendix A

## Supporting Material

### A.1 TLEs used in Chapter 3

Observation ID	Target	Absolute days b/w Obs and TLE
<b>TLE LINE 1</b>		
<b>TLE LINE 2</b>		
1102604896	Alouette-2	1
1 01804U 65098A 14348.18243322 .00000655 00000-0 21126-3 0 9997		
2 01804 079.8020 237.6772 1345902 080.7516 294.2870 12.24707195163859		
1142340880	ALOS	1.4
1 28931U 06002A 16079.98024251 +.00000391 +00000-0 +86490-4 0 9999		
2 28931 097.8961 122.7695 0001002 052.8253 307.3040 14.62149601541084		
1142351440	UKube-1	1.2
1 40074U 14037F 16079.81203031 .00001270 00000-0 16363-3 0 9993		
2 40074 98.3348 169.0455 0005943 80.4298 279.7595 14.82938013 91827		
1142425368	ISS	1.3
1 25544U 98067A 16078.18872957 .00011987 00000-0 18767-3 0 9997		
2 25544 51.6438 151.8661 0001598 315.1341 138.1171 15.54181702990822		
1142521608	Duchifat-1	0.1
1 40021U 14033M 16080.72630360 .00001579 00000-0 17313-3 0 9990		
2 40021 97.9377 347.0557 0013429 0.3746 359.7479 14.89116495 95096		

Figure A.1: TLEs used in Chapter 3 for DSNRS analysis.



## A.2 Supplementary Information for Orbit Determination Solution Convergence

As described in Section 5.5.1, the orbit determination pipeline used in this work using the closest epoch SSN published TLE for the target as the initial guess. In this section we test the dependence of the converged solution and confirm that the pipeline is in-fact updating the TLE to the epoch of the observation and not re-confirming the initial guess provided. We use the HST pass in observation 1157468632 as the test example for this analysis. Rather than feeding the pipeline with the closest epoch TLE as the initial guess (as done in Section 5.5.1), we provide the TLE published in the previous 14 days as the initial guess and analyse the converged solution.

In Figure A.2 we show the different initial guess provided to the pipeline using black markers and we see that the orbital elements can vary substantially even within a few days. The converged solution for all the provided initial guesses are shown using orange scatter points along with the solution reported in Table 5.1. We see that the converged solution is independent of the initial guess and using the closest epoch TLE as the initial guess only helps the solution converge faster.

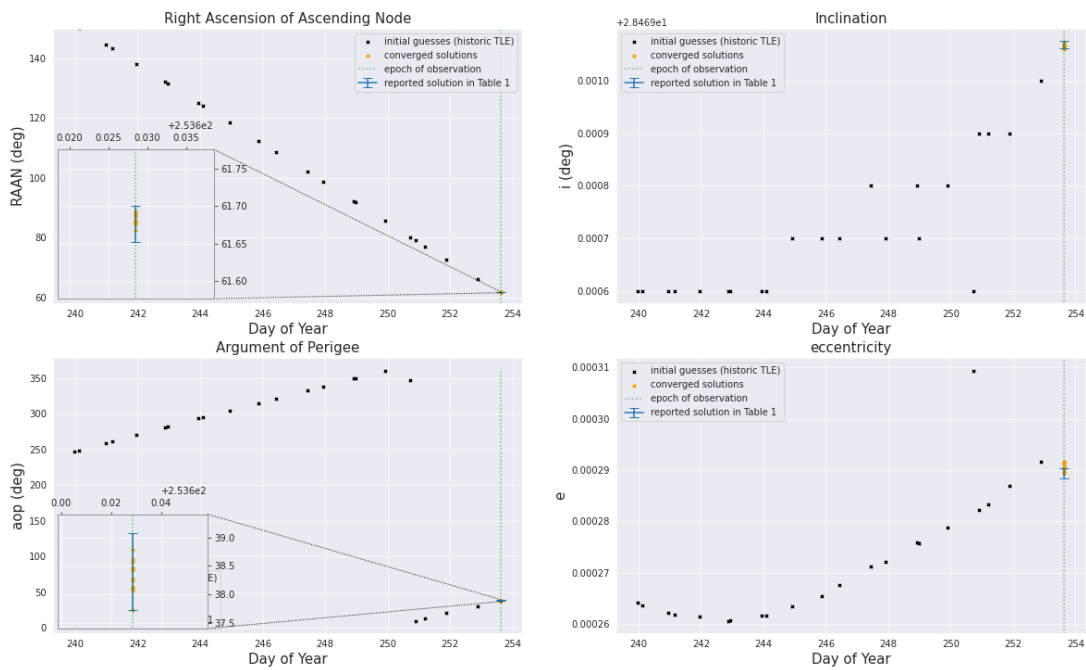


Figure A.2: In panels A, B, C, and D we show different initial guesses (for  $raan$ ,  $i$ ,  $aop$ , and  $e$  respectively) provided to the orbit determination pipeline using black scatter points. The converged solution for all the provided initial guesses are shown using orange scatter points. The solution determined in Table 5.1 using closest epoch TLE as the initial guess is shown using blue error-bars.

### A.3 Visibility fringe-washing as a function of satellite altitude

The classical mechanics equation for the linear velocity of a satellite in a circular orbit around Earth is given by

$$v = \sqrt{\frac{GM}{R + alt}} \quad (\text{A.1})$$

where  $v$  is the linear velocity of the satellite,  $G$  is the gravitation constant ( $6.67408 \times 10^{-11} m^3 kg^{-1} s^{-2}$ ),  $R$  (6371 km) is the radius of Earth,  $M$  is the mass of Earth and  $alt$  is the altitude of the considered satellite.

The fringe-rate (the time rate of change of the visibility phase) as measured by a zenith pointed East-West baseline is given by (obtained from [Marr et al. \(2015\)](#))

$$\frac{\delta\Phi}{\delta t} = 2\pi\omega \frac{b}{\lambda} \quad (\text{A.2})$$

and for small integration times Equation [A.2](#) becomes

$$\begin{aligned} \frac{\Delta\Phi}{\Delta t} &\approx 2\pi\omega \frac{b}{\lambda} \\ \Delta\Phi &\approx 2\pi\omega \frac{b}{\lambda} \Delta t \end{aligned} \quad (\text{A.3})$$

For an observer on the surface (i.e, the MWA), the apparent angular motion (for small angles near the zenith) can be derived using the derivative form of  $s = r\theta$  relating angular velocity with linear velocity ( $v = r\omega$ ). The apparent angular velocity  $\omega$  for a satellite (near the zenith) can be determined using Equation [A.1](#)

$$\begin{aligned} \omega &= \frac{v}{radius} = \frac{v}{alt} \\ \implies \omega &= \frac{1}{alt} \sqrt{\frac{GM}{R + alt}} \end{aligned} \quad (\text{A.4})$$

Substituting the value of  $\omega$  from Equation [A.4](#) in Equation [A.3](#), we get the function relating the change in visibility phase as measured by a baseline for the apparent motion of a satellite.

$$\Delta\Phi \approx 2\pi \frac{b}{\lambda \times alt} \sqrt{\frac{GM}{R + alt}} \Delta t \quad (\text{A.5})$$

# Appendix B

## Copyright Information

Chapter 3 and Chapter 4 of this thesis are reproduction of journal articles published in the Publications of the Astronomical Society of Australia (PASA). PASA grants permission to authors to re-use the articles in a Doctoral thesis. The licensing information for the two articles are attached in the following pages.



- Home
- Help ▾
- Email Support
- Sign in
- Create Account

**The development of non-coherent passive radar techniques for space situational awareness with the Murchison Widefield Array**

Author: Steve Prabu , Paul J. Hancock , Xiang Zhang , Steven J. Tingay

 **CAMBRIDGE UNIVERSITY PRESS**

Publication: Publications of the Astronomical Society of Australia  
Publisher: Cambridge University Press  
Date: Mar 23, 2020

*Copyright © Copyright © Astronomical Society of Australia 2020; published by Cambridge University Press*

**License Not Required**

Permission is granted at no cost for use of content in a Master's Thesis and/or Doctoral Dissertation. If you intend to distribute or sell your Master's Thesis/Doctoral Dissertation to the general public through print or website publication, please return to the previous page and select 'Republish in a Book/Journal' or 'Post on intranet/password-protected website' to complete your request.

BACK CLOSE



- Home
- Help ▾
- Email Support
- Sign in
- Create Account

**A low-frequency blind survey of the low Earth orbit environment using non-coherent passive radar with the Murchison widefield array**



Author: S. Prabu , P. Hancock , X. Zhang , S. J. Tingay  
Publication: Publications of the Astronomical Society of Australia  
Publisher: Cambridge University Press  
Date: Dec 9, 2020

*Copyright © © The Author(s), 2020. Published by Cambridge University Press on behalf of the Astronomical Society of Australia*

**License Not Required**

Permission is granted at no cost for use of content in a Master's Thesis and/or Doctoral Dissertation. If you intend to distribute or sell your Master's Thesis/Doctoral Dissertation to the general public through print or website publication, please return to the previous page and select 'Republish in a Book/Journal' or 'Post on intranet/password-protected website' to complete your request.

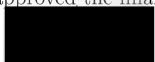


[BACK](#)

[CLOSE](#)

## B.0.1 Table of Attribution

### B.0.1.1 Chapter 3 of this thesis

Below is the table of co-author attribution for the journal article Prabu, S. Hancock, P. Zhang, X. Tingay, S.J, “The development of non-coherent passive radar techniques for space situational awareness with the Murchison Widefield Array”, Publications of the Astronomical Society of Australia , Volume 37 , 2020 , e010, DOI: <https://doi.org/10.1017/pasa.2020.1>.

	Conception & Design	Acquisition of Data & Method	Data Conditioning & Manipulation	Analysis & Statistical Method	Interpretation & Discussion
P. Hancock	✓				✓
P. Hancock Acknowledgement: I acknowledge that these represent my contribution to the above research output and I have approved the final version. Signed: 					
X. Zhang	✓				✓
X. Zhang Acknowledgement: I acknowledge that these represent my contribution to the above research output and I have approved the final version. Signed: 					
S.J. Tingay	✓				✓
S.J. Tingay Acknowledgement: I acknowledge that these represent my contribution to the above research output and I have approved the final version. Signed: 					



### B.0.1.2 Chapter 4 of this thesis

Below is the table of co-author attribution for the journal article Prabu, S. Hancock, P. Zhang, X. Tingay, S.J, “A low-frequency blind survey of the low Earth orbit environment using non-coherent passive radar with the Murchison Wide-field Array”, Publications of the Astronomical Society of Australia , Volume 37 , 2020, e052, DOI: <https://doi.org/10.1017/pasa.2020.40>.

	Conception & Design	Acquisition of Data & Method	Data Conditioning & Manipulation	Analysis & Statistical Method	Interpretation & Discussion
P. Hancock	✓				✓
P. Hancock Acknowledgement: I acknowledge that these represent my contribution to the above research output and I have approved the final version. Signed: ██████████					
X. Zhang	✓				✓
X. Zhang Acknowledgement: I acknowledge that these represent my contribution to the above research output and I have approved the final version. Signed: ██████████					
S.J. Tingay	✓				✓
S.J. Tingay Acknowledgement: I acknowledge that these represent my contribution to the above research output and I have approved the final version. Signed: ██████████					



# Bibliography

(1999). *Synthesis Imaging in Radio Astronomy II*, vol. 180 of *Astronomical Society of the Pacific Conference Series*.

V. Akhmetov, et al. (2019). ‘Analysis of the Indian ASAT test on 27 March 2019’.

K. Arimatsu, et al. (2021). ‘Detectability of Optical Transients with Timescales of Subseconds’. *The Astronomical Journal* **161**(3):135.

H. Aziz, et al. (2015). ‘RCS analysis on different targets and bistatic angles using LTE frequency’. vol. 3, pp. 658–663.

A. P. Beardsley, et al. (2019). ‘Science with the Murchison Widefield Array: Phase I Results and Phase II Opportunities’. *arXiv e-prints* p. arXiv:1910.02895.

J. C. Bennett, et al. (2015). ‘An analysis of very short-arc orbit determination for low-Earth objects using sparse optical and laser tracking data’. *Advances in Space Research* **55**(2):617–629.

G. M. Bernstein, et al. (2004). ‘The Size Distribution of Trans-Neptunian Bodies’. *The Astronomical Journal* **128**(3):1364–1390.

P. Bland, et al. (2012). ‘The Australian Desert Fireball Network: a new era for planetary science’. *Australian Journal of Earth Sciences* **59**(2):177–187.

N. Bobrinsky & L. Del Monte (2010). ‘The space situational awareness program of the European Space Agency’. *Cosmic Research* **48**(5):392–398.

- J. D. Bowman, et al. (2013). ‘Science with the Murchison Widefield Array’. *Publications of the Astronomical Society of Australia* **30**:e031.
- R. N. Bracewell & R. N. Bracewell (1986). *The Fourier transform and its applications*, vol. 31999. McGraw-Hill New York.
- L. D. Burkhart, et al. (2016). ‘A Deep Search for Additional Satellites around the Dwarf Planet Haumea’. *The Astronomical Journal* **151**(6):162.
- P. Castleberg & K. Xilouris (1997). ‘The Arecibo Observatory’. *IEEE Potentials* **16**(3):33–35.
- A. Celletti & G. Pinzari (2006). ‘Dependence on the observational time intervals and domain of convergence of orbital determination methods’. In A. Celletti & S. Ferraz-Mello (eds.), *Periodic, Quasi-Periodic and Chaotic Motions in Celestial Mechanics: Theory and Applications*, pp. 327–344, Dordrecht. Springer Netherlands.
- J. Choi, et al. (2018). ‘Optical tracking data validation and orbit estimation for sparse observations of satellites by the OWL-Net’. *Sensors* **18**(6):1868.
- J. Condon (1997). ‘Errors in elliptical Gaussian fits’. *Publications of the Astronomical Society of the Pacific* **109**(732):166.
- E. Cordelli, et al. (2019). ‘Use of a night-tracking camera for characterization and orbit improvement of defunct spacecraft’. *arXiv preprint arXiv:1903.00210* .
- T. Cornwell & R. Perley (1992). ‘Radio-interferometric imaging of very large fields-The problem of non-coplanar arrays’. *Astronomy and Astrophysics* **261**:353–364.
- T. J. Cornwell, et al. (2008). ‘The Noncoplanar Baselines Effect in Radio Interferometry: The W-Projection Algorithm’. *IEEE Journal of Selected Topics in Signal Processing* **2**(5):647–657.

- H. D. Curtis (2013). *Orbital mechanics for engineering students*. Butterworth-Heinemann.
- P. E. Dewdney, et al. (2009). ‘The square kilometre array’. *Proceedings of the IEEE* **97**(8):1482–1496.
- M. A. Earl (2015). ‘Determining the Range of an Artificial Satellite Using its Observed Trigonometric Parallax’.
- S. W. Ellingson, et al. (2013). ‘The LWA1 Radio Telescope’. *IEEE Transactions on Antennas and Propagation* **61**:2540–2549.
- T. Flohrer & H. Krag (2017). ‘Space Surveillance and Tracking in ESA’s SSA Programme’. *7Th European Conference on Space Debris* (1):18–21.
- S. Gallozzi, et al. (2020). ‘Concerns about ground based astronomical observations: a step to safeguard the astronomical sky’.
- T. Gaussiran II, et al. (2004). ‘LOFAR as an ionospheric probe’. *Planetary and Space Science* **52**(15):1375 – 1380.
- R. Goldstein, et al. (1998). ‘Radar observations of space debris’. *Planetary and Space Science* **46**(8):1007 – 1013.
- O. R. Hainaut & A. P. Williams (2020). ‘Impact of satellite constellations on astronomical observations with ESO telescopes in the visible and infrared domains’. *Astronomy & Astrophysics* **636**:A121.
- P. J. Hancock, et al. (2012). ‘Compact continuum source finding for next generation radio surveys’. *Monthly Notices of the Royal Astronomical Society* **422**:1812–1824.
- P. J. Hancock, et al. (2018). ‘Source Finding in the Era of the SKA (Precursors): Aegean 2.0’. *Publications of the Astronomical Society of Australia* **35**:e011.

- J. F. Helmboldt, et al. (2014). ‘All-sky imaging of meteor trails at 55.25 MHz with the first station of the Long Wavelength Array’. *Radio Science* **49**(3):157–180.
- K. G. Henize, et al. (1993). ‘Detection of orbital debris with GEODSS telescopes’. In *Space Debris Detection and Mitigation*, vol. 1951, pp. 76–84. International Society for Optics and Photonics.
- B. Hennessy, et al. (2020). ‘Orbit Determination Before Detect: Orbital Parameter Matched Filtering for Uncued Detection’. In *2020 IEEE International Radar Conference (RADAR)*, pp. 889–894. IEEE.
- B. Hennessy, et al. (2019). ‘Improved Techniques for the Surveillance of the Near Earth Space Environment with the Murchison Widefield Array’. In *2019 IEEE Radar Conference (RadarConf)*, pp. 1–6.
- J. A. Högbom (1974). ‘Aperture Synthesis with a Non-Regular Distribution of Interferometer Baselines’. *Astronomy and Astrophysics Supplement Series* **15**:417.
- B. Humphreys & T. Cornwell (2011). ‘Analysis of convolutional resampling algorithm performance’. *SKA Memo* **132**.
- N. Hurley-Walker, et al. (2017). ‘GaLactic and Extragalactic All-sky Murchison Widefield Array (GLEAM) survey - I. A low-frequency extragalactic catalogue’. *Monthly Notices of the Royal Astronomical Society* **464**(1):1146–1167.
- H. Hwang, et al. (2019). ‘Angles-only initial orbit determination of Low Earth Orbit (LEO) satellites using real observational data’. *Journal of Astronomy and Space Science* **36**(3):187–197. Funding Information: This research was supported by the development of Electro-optical Space Surveillance System, OWL-Net, and through the Korea Astronomy and Space Science Institute funded by the National Research Council of Science and Technology, and by the Korea Astronomy and Space Science Institute under the RD program (Project No. 2019-1-854-02) supervised by the Ministry of Science and ICT.

- T. JansenSturgeon, et al. (2019). ‘Comparing analytical and numerical approaches to meteoroid orbit determination using Hayabusa telemetry’. *Meteoritics Planetary Science* **54**(9):21492162.
- K. Jansky (1932). ‘Directional Studies of Atmosphericics at High Frequencies’. *Proceedings of the Institute of Radio Engineers* **20**(12):1920–1932.
- J. Johnson-Freese & D. Burbach (2019). ‘The Outer Space Treaty and the weaponization of space’. *Bulletin of the Atomic Scientists* **75**(4):137–141.
- B. A. Jones, et al. (2015). ‘Challenges of multi-target tracking for space situational awareness’. In *2015 18th International Conference on Information Fusion (Fusion)*, pp. 1278–1285. IEEE.
- T. Kelso (2007). ‘Analysis of the 2007 Chinese ASAT Test and the Impact of its Debris on the Space Environment’. In *Advanced Maui Optical and Space Surveillance Technologies Conference*, p. E35.
- T. S. Kelso (2009). ‘Analysis and Implications of the Iridium 33-Cosmos 2251 Collision’. In *Advanced Maui Optical and Space Surveillance Technologies Conference*, p. E3.
- D. J. Kessler & B. G. Cour-Palais (1978). ‘Collision frequency of artificial satellites: The creation of a debris belt’. **83**:2637–2646.
- D. J. Kessler, et al. (2010). ‘Kessler Syndrome-AAS Paper.pdf’. *Americal Astronomical Society* (January).
- J. Klos, et al. (2020). ‘On the possibility of using LOFAR radio telescope for passive radiolocation’. In *2020 21st International Radar Symposium (IRS)*, pp. 73–76. IEEE.
- J. Klos, et al. (2021). ‘Experimental Verification of the Concept of Using LOFAR Radio-Telescopes as Receivers in Passive Radiolocation Systems’. *Sensors* **21**(6):2043.

- A. Konovalenko, et al. (2005). ‘Status of the 70 meter antenna in Yevpatoria’. In *2005 15th International Crimean Conference Microwave and Telecommunication Technology, CriMiCo’2005-Conference Proceedings*, pp. 962–968.
- B. Lal, et al. (2018). ‘Global trends in space situational awareness (SSA) and space traffic management (STM)’. Tech. rep., INSTITUTE FOR DEFENSE ANALYSES WASHINGTON DC.
- E. Lenc, et al. (2018). ‘An all-sky survey of circular polarization at 200 MHz’. *Monthly Notices of the Royal Astronomical Society* **478**(2):2835–2849.
- W. Li, et al. (2018). ‘Comparing Redundant and Sky-model-based Interferometric Calibration: A First Look with Phase II of the MWA’. *The Astrophysical Journal* **863**(2):170.
- M. Losacco, et al. (2018). ‘The multibeam radar sensor BIRALES: Performance assessment for space surveillance and tracking’. In *69th International Astronautical Congress (IAC 2018)*, pp. 1–9.
- J. T. Lyon (1960). ‘Space Vehicles, Satellites, and the Law’. *McGill LJ* **7**:271.
- A. Mallama (2020). ‘A Flat-Panel Brightness Model for the Starlink Satellites and Measurement of their Absolute Visual Magnitude’. *arXiv preprint arXiv:2003.07805* .
- J. M. Marr, et al. (2015). *Fundamentals of radio astronomy: observational methods*, vol. 13. CRC Press.
- J. C. McDowell (2020). ‘The Low Earth Orbit Satellite Population and Impacts of the SpaceX Starlink Constellation’.
- J. P. McMullin, et al. (2007). ‘CASA Architecture and Applications’. In R. A. Shaw, F. Hill, & D. J. Bell (eds.), *Astronomical Data Analysis Software and Systems XVI*, vol. 376 of *Astronomical Society of the Pacific Conference Series*, p. 127.



- N. Metropolis & S. Ulam (1949). ‘The monte carlo method’. *Journal of the American statistical association* **44**(247):335–341.
- J. G. Miller (2007). ‘A new sensor allocation algorithm for the space surveillance network’. *Military Operations Research* pp. 57–70.
- D. Mishne (2004). ‘Formation control of satellites subject to drag variations and J2 perturbations’. *Journal of guidance, control, and dynamics* **27**(4):685–692.
- I. Molotov, et al. (2004). ‘Radar interferometer measurements of space debris using the Evpatoria RT-70 transmitter’. *Advances in Space Research* **34**(5):884–891.
- G. Muntoni, et al. (2021). ‘Crowded Space: A Review on Radar Measurements for Space Debris Monitoring and Tracking’. *Applied Sciences* **11**(4):1364.
- K. S. Obenberger, et al. (2016). ‘Rates, flux densities, and spectral indices of meteor radio afterglows’. *Journal of Geophysical Research (Space Physics)* **121**:6808–6817.
- A. R. Offringa, et al. (2014). ‘WSClean: an implementation of a fast, generic wide-field imager for radio astronomy’. *MNRAS* **444**(1):606–619.
- A. R. Offringa & O. Smirnov (2017). ‘An optimized algorithm for multiscale wideband deconvolution of radio astronomical images’. *MNRAS* **471**(1):301–316.
- A. R. Offringa, et al. (2016). ‘Parametrizing Epoch of Reionization foregrounds: a deep survey of low-frequency point-source spectra with the Murchison Wide-field Array’. *Monthly Notices of the Royal Astronomical Society* **458**(1):1057–1070.
- A. R. Offringa, et al. (2015). ‘The Low-Frequency Environment of the Murchison Widefield Array: Radio-Frequency Interference Analysis and Mitigation’. *Publications of the Astronomical Society of Australia* **32**:e008.

- S. M. Ord, et al. (2015). ‘The Murchison Widefield Array Correlator’. *Publications of the Astronomical Society of Australia* **32**:e006.
- J. E. Palmer, et al. (2017). ‘Surveillance of Space using passive radar and the Murchison Widefield Array’. In *2017 IEEE Radar Conference (RadarConf)*, pp. 1715–1720.
- C. Pardini & L. Anselmo (2009). ‘USA-193 decay predictions using public domain trajectory data and assessment of the post-intercept orbital debris cloud’. *Acta Astronautica* **64**(7):787 – 795.
- S. Prabu, et al. (2020a). ‘A low-frequency blind survey of the low Earth orbit environment using non-coherent passive radar with the Murchison widefield array’. *Publications of the Astronomical Society of Australia* **37**:e052.
- S. Prabu, et al. (2020b). ‘The development of non-coherent passive radar techniques for space situational awareness with the Murchison Widefield Array’. *Publications of the Astronomical Society of Australia* **37**:e010.
- S. Prabu, et al. (2020c). ‘Results from blind survey of LEO using MWA’.
- T. Prabu, et al. (2015). ‘A digital-receiver for the Murchison Widefield Array’. *Experimental Astronomy* **39**(1):7393.
- A. F. P. R. Sridharan (1998). ‘U.S. Space Surveillance Network capabilities’.
- J. Radtke, et al. (2017). ‘Interactions of the space debris environment with mega constellations-Using the example of the OneWeb constellation’. *Acta Astronautica* **131**:55–68.
- G. Reber (1944). ‘Cosmic Static.’. *The Astrophysical Journal* **100**:279.
- J. E. Reed (1969). ‘The AN/FPS-85 radar system’. *Proceedings of the IEEE* **57**(3):324–335.

- M. Rice & G. Laughlin (2020). ‘Exploring Trans-Neptunian Space with TESS: A Targeted Shift-stacking Search for Planet Nine and Distant TNOs in the Galactic Plane’. **1**(3):81.
- M. W. Richmond, et al. (2020). ‘An optical search for transients lasting a few seconds’. **72**(1):3.
- G. Ruiz, et al. (2005). ‘Algorithms for Multi-Beam Receiver Data Analysis’. In D. Danesy (ed.), *4th European Conference on Space Debris*, vol. 587 of *ESA Special Publication*, p. 89.
- M. Ryle & D. D. Vonberg (1946). ‘Solar Radiation on 175 Mc./s.’. *Nature* **158**(4010):339–340.
- H. Schaub, et al. (2015). ‘Cost and risk assessment for spacecraft operation decisions caused by the space debris environment’. *Acta Astronautica* **113**:66 – 79.
- M. I. Skolnik (1990). ‘Radar handbook second edition’. *McGrawHill* .
- M. Sokolowski, et al. (2017). ‘Calibration and stokes imaging with full embedded element primary beam model for the murchison widefield array’. *Publications of the Astronomical Society of Australia* **34**.
- E. G. Stansbery, et al. (1995). ‘Characterization of the orbital debris environment from haystack radar measurements’. *Advances in Space Research* **16**:5–16.
- Y. Taromaru, et al. (2005). ‘Observation of space debris by the Kamisaibara radar system’. In *Proceedings of the 4th European Conference on Space Debris*, pp. 18–20.
- G. B. Taylor, et al. (2012). ‘First Light for the First Station of the Long Wavelength Array’. *Journal of Astronomical Instrumentation* **1**:1250004–284.
- A. R. Thompson, et al. (2017). *Interferometry and synthesis in radio astronomy*. Springer Nature.

- S. Tingay & W. Joubert (2021). ‘High cadence optical transient searches using drift scan imaging II: Event rate upper limits on optical transients of duration  $\geq 21$  ms and magnitude  $\leq 6.6$ ’. *Publications of the Astronomical Society of Australia* **38**:e001.
- S. J. Tingay, et al. (2013a). ‘The Murchison widefield array: The square kilometre array precursor at low radio frequencies’. *Publications of the Astronomical Society of Australia* **30**(1).
- S. J. Tingay, et al. (2013b). ‘On the detection and tracking of space debris using the Murchison widefield array. I. Simulations and test observations demonstrate feasibility’. *Astronomical Journal* **146**(4).
- S. J. Tingay, et al. (2020). ‘A survey of spatially and temporally resolved radio frequency interference in the FM band at the Murchison Radio-astronomy Observatory’. *Publications of the Astronomical Society of Australia* **37**:e039.
- S. Torbert (2016). *Applied computer science*. Springer.
- S. E. Tremblay, et al. (2015). ‘The High Time and Frequency Resolution Capabilities of the Murchison Widefield Array’. *Publications of the Astronomical Society of Australia* **32**:e005.
- D. A. Vallado (2001). *Fundamentals of astrodynamics and applications*, vol. 12. Springer Science & Business Media.
- D. A. Vallado, et al. (2013). ‘Improved SSA through orbit determination of two-line element sets’. In *ESA Space Debris Conference*.
- M. P. van Haarlem, et al. (2013). ‘LOFAR: The LOw-Frequency ARray’. *Astronomy and Astrophysics* **556**:A2.
- R. Wayth, et al. (2017). ‘The Engineering Development Array: A low frequency radio telescope utilising SKA precursor technology’. *Publications of the Astronomical Society of Australia* **34**.

- R. B. Wayth, et al. (2018). ‘The Phase II Murchison Widefield Array: Design overview’. *Publications of the Astronomical Society of Australia* **35**.
- T. P. G. Wijnen, et al. (2020). ‘Using all-sky optical observations for automated orbit determination and prediction for satellites in Low Earth Orbit’.
- M. J. Wilensky, et al. (2020). ‘Quantifying Excess Power from Radio Frequency Interference in Epoch of Reionization Measurements’.
- A. Witze (2018). ‘The quest to conquer Earth’s space junk problem’. *Nature* **561**:24–26.
- D. F. Woods, et al. (2013). ‘Space Surveillance Telescope: focus and alignment of a three mirror telescope’. *Optical Engineering* **52**(5):053604.
- X. Zhang, et al. (2018). ‘Limits on radio emission from meteors using the MWA’. *Monthly Notices of the Royal Astronomical Society* **11**(April):1–11.

Every reasonable effort has been made to acknowledge the owners of copyright material. I would be pleased to hear from any copyright owner who has been omitted or incorrectly acknowledged.